



Intuitive Physical Human-Robot Interaction Using a Parallel Mechanism in a Macro-Mini Architecture.

Mémoire

Nicolas Badeau

Maîtrise en génie mécanique - avec mémoire
Maître ès sciences (M. Sc.)

Québec, Canada

Intuitive Physical Human-Robot Interaction Using a Parallel Mechanism in a Macro-Mini Architecture.

Mémoire

Nicolas Badeau

Sous la direction de:

Clément Gosselin, directeur de recherche

Résumé

Ce mémoire présente le développement d'un mécanisme de type macro-mini permettant des interactions humain-robot intuitives. Le type d'architecture macro-mini permet de contrôler un robot ayant une grande impédance tel qu'une cellule robotisée cartésienne (e.g. *gantry*) à l'aide d'un mécanisme à plus faible impédance, réduisant considérablement l'effort devant être fourni par l'opérateur et atténuant par conséquent la fatigue de ce dernier.

Le mécanisme macro-mini proposé est composé d'une cellule robotisée cartésienne ayant trois axes et d'un mécanisme parallèle découplé à trois degrés de liberté. Chacun des axes de la cellule est contrôlé à partir de mesures de position angulaire provenant d'un encodeur attaché à l'un des degrés de liberté du mécanisme parallèle. Ce type d'architecture découplé permet un contrôle simple et intuitif.

Le contrôle par impédance est privilégié pour ce type d'architecture. Une comparaison expérimentale des performances entre le contrôle par impédance et par admittance — utilisant des capteurs d'effort — est également présentée. L'analyse des résultats obtenus démontre que le contrôle par impédance permet d'effectuer des tâches plus rapidement (facteur 2) et avec moins d'effort (facteur 20).

Une analyse approfondie de la stabilité du système avec différents modèles de contrôleur par impédance a été effectuée. Ceci a permis de déterminer que le contrôleur par impédance standard n'est pas stable lorsque utilisé avec l'architecture proposée. Un contrôleur alternatif a donc été développé afin de permettre un contrôle plus intuitif et stable.

L'ajout d'un moteur à l'axe de rotation du mécanisme parallèle a permis la création de retour haptique à l'utilisateur afin de simuler des interactions avec des objets ou contraintes virtuelles. Ce retour haptique a également été utilisé pour varier l'impédance ressentie par l'utilisateur en ajoutant une masse virtuelle à l'effecteur du mini.

Pour terminer, l'analyse de la dynamique du système est utilisée pour la détection de collision entre le mécanisme parallèle et l'environnement sans avoir recours à des capteurs d'effort. Cet élément est essentiel pour des interactions humain-robot sécuritaires.

Abstract

This thesis presents the development of a novel macro-mini mechanism allowing intuitive physical human-robot interaction (pHRI). This type of architecture allows the control of a high-impedance robot — such as a Cartesian gantry robot in a manufacturing environment — using a smaller and lower impedance mechanism, therefore allowing a significant reduction of the operator’s effort and fatigue.

The proposed macro-mini mechanism consists of a three-axis Cartesian gantry system (i.e. macro mechanism) and a passive three-degree-of-freedom parallel mechanism (i.e. mini mechanism). The mini mechanism is statically balanced at its workspace centre and all three degrees of freedom are decoupled. This means that the gantry axes are individually controlled using the measurement of a single angular encoder of the mini. It also means that the motion of the mini mechanism along the direction of a degree of freedom does not affect the remaining degrees of freedom, considerably simplifying the control.

The use of impedance control with this type of architecture is thoroughly described and analyzed. An experimental comparison with a standard admittance controller — using a force sensor — is accomplished using a simple peg-in-hole experiment. Results show that the impedance control allows a faster task completion (by a factor of 2) with smaller effort (by a factor of 20) compared with the admittance controller.

A comprehensive stability analysis is also accomplished on several designs of impedance controller, but with the same macro-mini architecture. Results demonstrate that the standard impedance controller is not stable with the proposed architecture and hence an alternative controller is introduced and evaluated.

A backdrivable motor is added at the mini’s joint in order to render haptic feedback to the operator. Such feedback is used to simulate virtual environment interactions such as walls and collisions with movable objects. The backdrivable motor is also used to vary the impedance felt by the user during control by adding a virtual mass at the mini mechanism end-effector.

Finally, the system’s dynamic analysis is used for collision detection of the macro-mini mechanism during planned trajectory motion without the need for force sensors. This last aspect is essential for safe physical human-robot interactions.

Contents

Résumé	ii
Abstract	iii
Contents	iv
List of Tables	vi
List of Figures	vii
Remerciements	xi
Foreword	xii
Introduction	1
1 Intuitive Physical Human-Robot Interaction Using a Passive Parallel Mechanism	3
1.1 Résumé	3
1.2 Abstract	3
1.3 Introduction	4
1.4 Architecture of the Macro-Mini Mechanism	6
1.5 Kinematic Performance of the Macro-Mini Robot	14
1.6 Control of the Macro-Mini robot	18
1.7 Experimental Results	19
1.8 Video Demonstration	24
1.9 Conclusion	25
1.10 Bibliography	25
2 Passive Macro-Mini Impedance Control Analysis	28
2.1 Introduction	29
2.2 Experimental Setup	30
2.3 System's Dynamic Analysis	32
2.4 Standard Impedance Controller	35
2.5 Frequency-Dependent Stiffness Controller	50
2.6 Conclusion	61
2.7 Bibliography	63
3 Active Macro-Mini Architecture and Control Strategies	64

3.1	Introduction	65
3.2	Impedance Control with Haptic Feedback	66
3.3	Planned Trajectory Motion	87
3.4	Trajectories Involving Interactions with the Environment	96
3.5	Conclusion	100
3.6	Bibliography	101
	Conclusion	104
	Bibliography	106

List of Tables

1.1	Comparison of the inertia perceived at the end-effector for the serial LIP mechanism proposed in [13] and the parallel LIP mechanism proposed in this paper.	10
1.2	Velocity and acceleration limitations of the HIA mechanism used in the prototype.	16
1.3	Results of the qualitative survey on the user experience.	24
2.1	Macro-mini experimental parameters and variables.	31

List of Figures

1.1	Decoupled translational 3-dof parallel mechanism (Tripteron)(from [7]).	8
1.2	Novel mini LIP parallel mechanism.	9
1.3	Comparison of size and complexity of the mechanism proposed in this paper (left) and the mechanism proposed in [13] (right).	10
1.4	Geometric and mass parameters for the statically balanced mechanism (X- and Y-axis).	12
1.5	Macro-mini robotic system for pHRI. The mini LIP mechanism is mounted on the end-effector of the macro HIA mechanism.	13
1.6	Schematic representation of a 1-dof active-passive mechanism (taken from [12]).	14
1.7	Maximum feasible motion amplitude as a function of the frequency of the input movement.	17
1.8	Control architecture of the macro-mini robotic system using the parallel LIP mechanism.	18
1.9	Schematic representation of the experimental setup used to determine the human motion capabilities (amplitude as a function of the frequency).	20
1.10	Holed board used for the peg-in-hole experiment.	21
1.11	Measured forces for the peg-in-hole experiment with the HIA mechanism only and admittance control.	22
1.12	Measured forces for the peg-in-hole experiment with the proposed LIP-HIA mechanism.	22
1.13	Average force and time to execute the task for the 100 trials performed by the 10 volunteers.	23
2.1	Photo of the macro-mini simplified mechanism used for the experimental test. .	30
2.2	Schematic of the experimental setup used in Chapters 2 and 3.	31
2.3	Representation of the simplified macro-mini passive mechanism.	32
2.4	Simulated response for over-damped $\zeta = 1.5$, under-damped $\zeta = 0.5$ and critically damped $\zeta = 1$ sets of gains.	42
2.5	Experimental response for multiple virtual stiffness K_d values. $\{M_d = C_d = 0\}$	43
2.6	Comparison of a simulated and an experimental response for a selected virtual stiffness value. $\{K_d = 1000, M_d = C_d = 0\}$	44
2.7	Experimental response for multiple virtual damping C_d values. $\{K_d = 1000, M_d = 0\}$	45
2.8	Comparison between simulated and experimental response for a selected virtual stiffness and damping. $\{K_d = 1000, C_d = 400, M_d = 0\}$	46
2.9	Theoretical response for different values of the virtual mass. Curves were normalized in amplitude. $\{K_d = 1000, C_d = 400\}$	47

2.10	Experimental response for multiple virtual mass M_d values. $\{K_d = 1000, C_d = 400\}$	48
2.11	Simulated response of the system for different values of γ using the proposed methodology for an over-damped system gain sets.	59
2.12	Experimental response for multiple values of frequency-dependent virtual stiffness K_f . $\{K_d = 1000, C_d = 400\}$	60
3.1	Illustration of the dynamics involved in the interactions between the mini end-effector and the virtual wall.	69
3.2	Illustration of the dynamics involved in the interactions between the mini end-effector and a movable virtual object described by a virtual mass M_v and damping C_v	70
3.3	Collision's response for different values of the coefficient of restitution γ . ($C_v = 3$ kg/s, $M_v = 15$ kg)	74
3.4	Collision's response for different values of the virtual mass M_v . ($C_v = 1.5$ kg/s, $\gamma = 0.5$)	76
3.5	Collision's response for different values of the virtual mass C_v . ($M_v = 1.5$ kg, $\gamma = 0.5$)	77
3.6	Illustration of a virtual mass M_v attached to the mini end-effector. The virtual mass is simulated via the mini mechanism control torque $\tau_c(t)$	78
3.7	Theoretical response to a unit-impulse force ($F_H(s) = 1$) for different values of the virtual mass M_v	82
3.8	Typical signal measured during the virtual mass experiment.	84
3.9	Theoretical and experimental force f_h as a function of the mini angular position $\theta(t)$ and virtual mass M_v	85
3.10	Theoretical motion of the macro system. The time axis is normalized to the period $T = t_f - t_0$. The initial position is $x_A = 0$ m and the final position is $x_B = 1$ m	88
3.11	Empirical results obtained for a motion from $x_A = 0$ m to $x_B = 0.2$ m.	91
3.12	Comparison of the mini position between the passive and active mechanism.	94
3.13	Forces during trajectory motion, no collision.	98
3.14	Forces during trajectory motion, collision occurs at c. $t = 0.4$ s during the trajectory.	99

*À ma conjointe Kathy, et mon
fils Ethan.*

I'd take the awe of understanding
over the awe of ignorance any
day.

Douglas Adams

Remerciements

Je tiens tout d'abord à remercier mon directeur de maîtrise, le professeur Clément Gosselin, pour son soutien et ses conseils tout au long de mes études, y compris lors de mes trois années en tant qu'assistant de recherche au baccalauréat. Sa supervision et ses enseignements m'ont permis de devenir un bien meilleur ingénieur et scientifique.

Je veux également souligner l'aide apportée par les professionnels de recherche du laboratoire, Simon Foucault et Thierry Laliberté, sans qui ce projet n'aurait pu voir le jour. Leur dévouement pour la robotique et les étudiants du laboratoire n'a d'égal que leur connaissance.

Cette maîtrise a été complétée avec le soutien financier d'Olympus, pour qui je travaille depuis maintenant les six dernières années. Je veux remercier mes nombreux collègues qui m'ont soutenu tout au long de ce projet et qui par le fait même, et sans bien le vouloir, ont pris un peu de ma charge de travail.

Pour terminer, je tiens à mentionner le soutien indéfectible de ma conjointe, Kathy. Ses encouragements et sa compréhension envers mon désir de compléter ce projet ont été plus que nécessaires et appréciés. Son aide inconditionnelle, alors même que nous fondions notre famille, témoigne de son amour.

Et à mon garçon, Éthan, qui me démontre jour après jour l'importance de la curiosité pour grandir, merci.

Foreword

Chapter 1 is an article published in the IEEE Robotics and Automation Magazine (RAM). The information regarding this article and my own contribution to it are described below.

Title: Intuitive Physical Human-Robot Interaction Using a Passive Parallel Mechanism

Journals: IEEE Robotics and Automation Magazine

Status: Published in June 2018

Contribution: First author. Design and implementation of real-time impedance controller.

Coauthors:

Clément Gosselin: Second author and supervisor for the preparation of the article and its revision.

Thierry Laliberté: Design of the passive parallel mechanism.

Simon Foucault: Supervised and helped for the experimental section.

Muhammad E. Abdallah: Revision of article.

Chapter 2 presents a complete analysis of the passive macro-mini architecture where the mini mechanism is unactuated. The chapter includes an analysis of the dynamics of the system and a comparison between a standard impedance controller and the frequency-dependent stiffness controller used for the IEEE RAM article.

Chapter 3 presents an actuated version of the mini mechanism. This additional active degree of freedom is firstly used to generate haptic feedback to the user. It is also used to reduce the swinging movement of the mini mechanism occurring during planned trajectory motion of the macro mechanism. Finally, a method is presented to detect collision between the environment and the mini end-effector solely using the system dynamics and angular encoder measurements.

Introduction

The current industrial environment requires, now more than ever before, robotic systems that can be used alongside human operators. The lack of flexibility and agility of current robotic cells in assembly lines causes task adaptation and physical human-robot interactions (pHRI) to be difficult and expensive. Human-robot collaboration is beneficial when a task requires the agility of a human operator but the strength of a robotic system.

The domain of collaborative robots — commonly called cobots — is growing fast. Companies like Universal Robots and Robotiq, among others, are providing solutions for simple collaborative tasks such as CNC machine tending or adaptive sanding. However, such solutions are still based on admittance control using force sensors and they rely on torque constraints for safety reason. These limitations cause such solutions to be unusable in assembly lines where heavy objects must be manipulated with minimal effort by human operators.

Indeed, intuitiveness and effortlessness are of paramount importance for human-robot interactions in assembly lines since they directly affect the time that an operator needs to accomplish a task and the number of times this task can be repeated with precision without putting the operator's health and safety at risk.

While most collaborative robots use admittance controllers, converting force input into motion output, this type of control still has some limitations. To begin with, the impedance felt by the operator when manipulating the robot is directly linked with the mass, motion and configuration of the robot. Also, since signals generated by force sensors are usually noisy, low-pass filtering is necessary, therefore causing small delays in the control, which sometimes can render the control non-intuitive or simply unstable.

On the contrary, impedance controllers convert motion input into force to be applied to or by the robotic system. Using a low-impedance mechanism as an interface between an operator and a higher-impedance mechanism such as a gantry system allows for intuitive, fast and effortless control. In this case, the impedance felt by the operator can therefore be decoupled from the high-impedance robotic system and its payload.

The main objective of this study is to design, implement and evaluate a stable impedance controller for such macro-mini mechanism architecture. While the mini mechanism architecture

was already designed prior to this study, the controller needed to be designed and evaluated. In order to better evaluate the performance of the macro-mini architecture with the proposed impedance controller, a comparison with a standard admittance controller using force sensor measurements is completed and presented herein.

The second objective is to render haptic feedback using the macro-mini architecture. In this case, a backdrivable motor is added to the mini mechanism's joint. The interactions with a variety of virtual objects are effectively being simulated using this additional actuated degree of freedom.

The third and last objective is to design stable and safe motion trajectories for the macro mechanism without intervention from a human operator. Indeed, while human-robot interactions remain the main objective of using such macro-mini architecture, it still must be able to carry out simple pick and place operations autonomously. For safety reasons, a collision detection method not relying on force sensor measurements is also developed in the course of this study.

This thesis is structured as follows. Chapter 1 presents an article published in the IEEE Robotics and Automation Magazine (RAM). This paper includes a description of the macro-mini mechanism and the impedance controller used. A comparison between the impedance controller and a standard admittance controller is also presented for a simple peg-in-hole experiment. Chapter 2 presents a more thorough analysis of such a macro-mini architecture with a simplified experimental setup. Two different impedance controllers are analyzed and compared for stability performance. Chapter 3 presents the results of the addition of a backdrivable motor to the mini mechanism joint. The active mini mechanism is used to simulate interactions with virtual objects and to compensate for payload oscillations during planned motion. A collision detection algorithm is also presented and tested.

Chapter 1

Intuitive Physical Human-Robot Interaction Using a Passive Parallel Mechanism

1.1 Résumé

Dans ce papier, nous proposons un nouveau mécanisme passif parallèle et une architecture de type macro-mini pour des interactions humain-robot efficaces et intuitives. L'architecture de type macro-mini permet d'utiliser un mécanisme passif à faible impédance (mini) afin de facilement et intuitivement contrôler un mécanisme actif à forte impédance (macro) tel qu'un robot portique Cartésien. Le mécanisme mini proposé est basé sur un robot parallèle translationnel à trois degrés de liberté, le rendant simple et compacte, permettant ainsi de minimiser l'inertie ajoutée à l'effecteur du mécanisme macro. Le mécanisme mini passif est premièrement décrit et analysé. Ensuite, la cinématique de l'architecture macro-mini est étudiée afin d'établir les capacités du robot. Un contrôleur par impédance est par la suite proposé afin de contrôler les mouvements du mécanisme macro à partir des coordonnées relatives du mécanisme mini. Finalement, des résultats expérimentaux sont présentés afin d'illustrer la performance et l'intuitivité du robot.

1.2 Abstract

In this paper we propose a novel passive mechanism and a macro-mini architecture for effective and intuitive physical human-robot interaction (pHRI). The macro-mini concept allows the use of a mini low-impedance passive mechanism (LIP) to effortlessly and intuitively control a macro high-impedance active (HIA) system such as a gantry manipulator. The proposed mini LIP design is based on a three-degree-of-freedom (3-dof) translational parallel mechanism, which makes it simple and compact, thereby adding little inertia to the end-effector of the macro

HIA mechanism. The kinematically and statically decoupled LIP mechanism is first described and analysed. Then, the kinematics of the macro-mini architecture is studied in order to establish the capabilities of the robot. A controller is then proposed that uses the passive joint coordinates of the LIP mechanism as input to control the motion of the HIA mechanism. Finally, experimental results are provided in order to illustrate the performance and intuitive behaviour of the robot, which is particularly suited for manufacturing applications.

1.3 Introduction

The current fast-evolving industrial environment requires robotic systems that are highly precise, powerful, and yet as flexible and dexterous as human workers. Human-robot collaboration is hence a rapidly growing field where actuated systems are either actively controlled by humans or interacting with them. A common paradigm in physical human-robot interaction (pHRI) consists in a human user guiding the motion of a robot through direct physical contact. In order to obtain an intuitive behaviour, the robot should ideally be as responsive as a human co-worker. Such an agile behaviour is difficult to produce, especially with robots that have large payload capabilities. This is the case in industrial applications where many tasks require human-fine manipulation adaptability while being exhausting or requiring humans to apply forces that are beyond ergonomic feasible ranges.

Most industrial robots can be characterised by very narrow impedance bandwidth, large payload capability, precise actuators and extensive workspace. On the contrary, humans have large impedance bandwidth, flexibility and dexterity but low payload capabilities. The possibility to combine the advantages of both may yield highly effective industrial systems. This approach led to the development of human-friendly robotic manipulators [18], notably, in the field of pHRI [11], [3]. In order to allow fine manipulation, pHRI manipulators should closely match the varying human mechanical impedance. In other words, if the apparent impedance of a manipulator can be minimized, the human operator can then deploy his/her own impedance, which yields a very intuitive interaction. This is especially important in assembly operations, where the matching of parts requires a very low impedance interaction to be effective and intuitive to the human operator.

In most industrial pHRI applications, force/torque sensors are used to sense and regulate the interaction between the human operator and the robot. An admittance controller is then used to emulate different impedances [19, 16]. In some cases, a PI controller [17], or even lead and lag compensators [1] are used. However, it has been shown that the hardware dynamics limit the apparent impedance reduction [9] and that any attempt to go below a certain fraction of the intrinsic inertia leads to unstable behaviours [4]. According to [19, 1, 16], based on such techniques, the apparent inertia can be reduced by a factor of 5 to 7 with respect to the real inertia. Other approaches making use of force sensors include the appending of compliant

material in order to mechanically filter the high-frequency interactions [14]. Nevertheless, large inertia reduction ratios are achievable only by overstepping the concept of passivity [5, 6], which means that physical contacts are limited to specific ranges of environment dynamics.

Also, when physically interacting with a robot over long periods of time, for instance over a working shift in an assembly plant, intuitiveness is of paramount importance. If a system lacks responsiveness, the human user can have the impression of constantly ‘dragging’ or ‘fighting’ the robot, which becomes tiring and frustrating. The use of force/torque sensors typically requires filters to reduce the sensor noise, which yields a lack of responsiveness due to delays and induces the ‘dragging’ impression. This issue can be addressed by replacing the high-impedance force/torque sensor by a low-impedance mechanical interface, which can in fact be considered as a position sensor¹. This approach was used in [12] and [13], where it was proposed to use the concept of underactuation redundancy to provide very low mechanical impedance to a human operator. In this concept, a low-impedance passive (LIP) mini manipulator, which provides the low-impedance interaction, is mounted at the end-effector of a high-impedance active (HIA) macro manipulator that provides the workspace and force capabilities. Such an arrangement yields an apparent impedance that is lower than that of any actuated mechanism. This concept nicely applies to task spaces with limited degrees of freedom, for example to 4-dof SCARA²-type tasks. In such tasks, the space is divided into the space of operational degrees of freedom and the space of constrained degrees of freedom. In the space of operational degrees of freedom, all the work on the payload — except for the gravity compensation forces — is performed by the human being, while in the constrained space, the constraint forces are provided by the robot. Therefore, only the operational degrees of freedom need to render the low impedance. Examples of similar mechanisms are cable-suspended intelligent assist devices [20, 2]. Unfortunately, cable-suspended devices cannot constrain rotational motion and cannot handle off-centred payloads.

The robot proposed in [13] consists of a macro 3-dof active gantry system on which a passive 3-dof mini mechanism is mounted. The effectiveness of the low-impedance rendering is clearly demonstrated in assembly operations such as peg-in-hole tasks. Indeed, the robot is shown to be very responsive, intuitive and provides very high bandwidth for small-range precision tasks. Also, when the robot is moving autonomously, collisions can be easily detected and contact forces in the occurrence of a collision are very low compared to those encountered in active systems.

Moreover, the HIA mechanism constituting the macro component of the robot is located outside of the human operator’s workspace, which ensures safety, i.e., the human operator interacts strictly with the low-impedance passive mechanism. However, the mini manipulator

¹It should be pointed out that force/torque sensors based on strain gauges can also be considered as position sensors, though with a very high impedance, since they are based on the measurement of the extension of the strain gauges.

²Selective Compliance Assembly Robot Arm or Selective Compliance Articulated Robot Arm

proposed in the aforementioned reference is based on the serial arrangement of three complex 1-dof mechanisms that aim at decoupling the three translational directions of motion while providing a central equilibrium configuration to which the mini manipulator smoothly returns when no external force is applied on it. One of the drawbacks of this mechanism is its complexity. Indeed, a large number of links and joints are required to ensure proper kinematics. Another drawback of the passive mechanism proposed in [13] is that the forces that tend to return the mechanism to its neutral position when displaced horizontally are proportional to the mass of the payload attached to the end-effector. When large payloads are handled, this effect can be detrimental because the human operator then has to deploy significant forces.

In this paper, we propose a novel mini low-impedance passive (LIP) mechanism. The mechanism is based on a decoupled parallel mechanism referred to as the tripteron [7], which makes it much more compact than the mini passive mechanism proposed in [13]. Moreover, the inertia of the proposed mechanism is equivalent in all directions, thereby producing a very intuitive interaction. Also, the design of the mechanism is such that the forces that tend to return the mechanism to its equilibrium configuration are independent from the mass of the payload. Similarly to what was done in [13], the novel mechanism is mounted on a 3-dof translational gantry mechanism and a macro-mini controller is used to control the motion of the gantry based on the motion of the mini passive mechanism.

This paper is structured as follows. Section 1.4 describes the architecture of the novel LIP mechanism. Design issues are discussed, including kinematic and static decoupling. Section 1.5 presents a kinematic analysis of the macro-mini mechanism that is used to determine the capabilities of the robot. Section 1.6 describes the controller used for the macro-mini architecture, including the use of the mini LIP mechanism’s joint coordinates as commands for the macro HIA mechanism. Experimental results obtained with a prototype of the proposed mechanism are reported in Section 1.7, and some of them are compared with the analysis provided in Section 1.5. Section 1.8 describes the video attached to this paper, while concluding remarks are given in Section 1.9.

1.4 Architecture of the Macro-Mini Mechanism

In the proposed concept, a mini LIP mechanism is mounted on the end-effector of a macro HIA mechanism. The payload or tool to be manipulated is mounted on the end-effector of the mini LIP mechanism. In addition to its low impedance, the passive mini mechanism is designed such that it has only one static equilibrium position at the centre of its workspace. When the user displaces the payload/tool from its equilibrium position, the motion induced in the passive mini mechanism is measured by encoders mounted on its passive joints. This motion is used as a command for the macro HIA mechanism. If the response of the macro HIA mechanism is fast enough for the end-effector of the mini LIP mechanism to remain within its

workspace at all times, the interaction impedance felt by the user remains very low, thereby providing a very intuitive interaction. Also, if the user lets go of the payload, the payload converges to its equilibrium configuration, thereby smoothly stopping the motion of the macro HIA mechanism.

In the following subsections, the architecture of the novel mini LIP mechanism as well as that of the macro HIA mechanism are presented. A detailed description of the LIP mechanism, which is based on a 3-dof Cartesian parallel mechanism, is first given. Then, the HIA gantry mechanism is briefly presented.

1.4.1 Architecture of the LIP - Mini Tripteron Mechanism

The novel mini LIP mechanism is based on the Tripteron translational parallel robot, proposed in [7, 10, 8] and shown in Fig. 1.1. This parallel mechanism has a 3- $\underline{P}RRR$ architecture, where R stands for a passive revolute joint and \underline{P} stands for an actuated prismatic joint. The geometric arrangement of the joints in this overconstrained mechanism provides three kinematically decoupled and orthogonal degrees of freedom, namely the three pure Cartesian translations. The rotation of the end-effector is prevented and hence only pure translations are possible. With this orthogonal arrangement of the actuated prismatic joints, the kinematics of the robot simplifies to

$$\boldsymbol{\rho} = \boldsymbol{p}, \quad \dot{\boldsymbol{\rho}} = \dot{\boldsymbol{p}} \quad (1.1)$$

where $\boldsymbol{\rho}$ is the 3-component array containing the three prismatic joint displacements and \boldsymbol{p} is the 3D position vector of a reference point on the end-effector, both arrays' components being expressed in metres. In other words, each of the prismatic joints controls the motion of one of the Cartesian coordinates and is completely decoupled from the others. The time derivative appearing in the second equation in (1.1) means that the Jacobian matrix of the mechanism is the identity matrix and therefore that the mechanism is free from singularities within its workspace. In the application pursued in this work, the kinematic decoupling of the mechanism is very important. Indeed, it is imperative that the vertical motion of the LIP mechanism be decoupled from the horizontal motion because these two types of motion are handled differently, similarly to what was done in [13]. Namely, the vertical motion of the LIP mechanism is centred on an equilibrium position that is induced by a spring system whereas the equilibrium position of the horizontal motion is produced by the pendulum effect of the parallelogram mechanisms corresponding to the horizontal motion. A kinematically coupled mechanism could not produce such a behaviour.

When no external force is applied on its end-effector, the LIP mechanism naturally returns to its equilibrium neutral configuration. This is essential for the proper functioning of the macro-mini system. Indeed, if the human operator lets go of the mechanism, the robot should



Figure 1.1 – Decoupled translational 3-dof parallel mechanism (Tripteron)(from [7]).

stop. However, the base prismatic joints of the Tripteron mechanism are not well suited for this type of behaviour. Therefore, the prismatic joints at the base of the Tripteron are replaced with parallelogram joints, yielding a $3-\Pi RRR$ passive mechanism, where Π stands for a passive parallelogram joint. Figure 1.2(a) shows a CAD model of the architecture of the mechanism. In each of the three legs, a parallelogram mechanism is attached to the base. Encoders are mounted on one of the fixed joints of the parallelogram mechanism in order to measure the corresponding joint coordinate. This rotational coordinate is readily transformed into a translational displacement of the end-effector using

$$p_i = \ell_p \cos \theta_i, \quad i = 1, 2, 3 \quad (1.2)$$

where, as shown in Fig. 1.2(b), p_i is one of the components of the displacement of the end-effector, θ_i is the angle at the base of the corresponding parallelogram, measured with the encoder and ℓ_p is the length of the pivoting bar of the parallelogram. Then, two intermediate links connect the parallelogram to the end-effector using three passive revolute joints with parallel axes. Two of the parallelograms, associated with the horizontal motion (X and Y motion), act as pendulums that automatically return to their neutral configuration under the effect of gravity when no external load is applied on the end-effector. This return action of the parallelogram introduces very little friction in the mechanism and is therefore ideal for application in the LIP mechanism. The third parallelogram, shown on the right-hand side in Fig. 1.2(a), produces the vertical motion and is therefore not in equilibrium in its neutral configuration. For this parallelogram, a spring is used to obtain the desired behaviour, i.e., to ensure that the equilibrium configuration is located in the neutral configuration. The geometric arrangement of the spring is illustrated in Fig. 1.2(b).

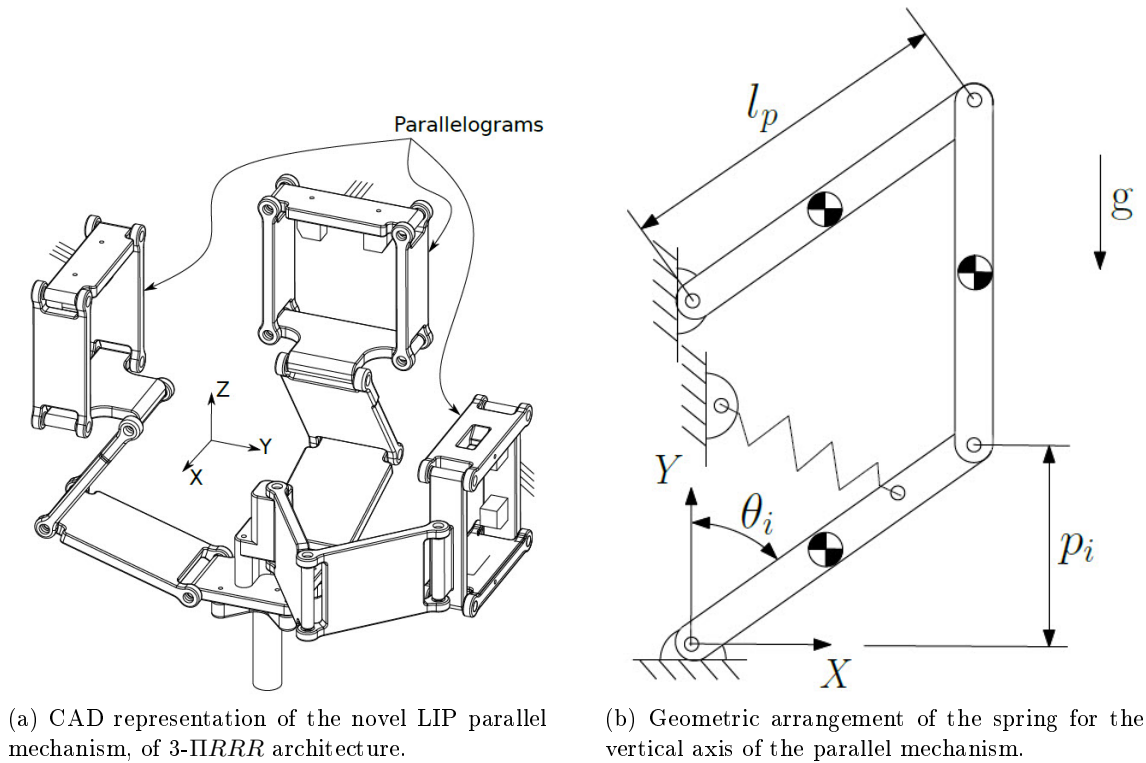


Figure 1.2 – Novel mini LIP parallel mechanism.

It should be pointed out that replacing the prismatic joints of the original Tripteron mechanism with parallelograms has no impact on the kinematic decoupling properties of the mechanism. Indeed, although parallelograms produce a coupled motion in two directions, the ‘parasitic’ component of the motion is annihilated by the passive motion of the other passive joints of the mechanism. This property is clearly described in [7, 10]. Indeed, as mentioned earlier, all three axes are completely decoupled, meaning that movement in one axis does not cause displacement in any of the remaining axes. Therefore, compared to the mini LIP mechanism proposed in [13], a key advantage of the mechanism proposed here is that the horizontal motion of the payload does not produce any parasitic vertical motion. In the LIP mechanism proposed in [13], when moving the payload horizontally, the mini mechanism induces a parasitic vertical motion, which means that the user feels a fraction of the weight of the payload that is being manipulated, which tends to return the payload to its neutral configuration. In the mechanism proposed here, the return action is independent from the mass of the payload and is strictly dependent on the mass of the moving links of the passive mechanism, which can be small and adjusted using counterweights mounted on the links.

Another significant advantage of the LIP mechanism proposed here is that it is much more compact and much simpler than the mechanism proposed in [13]. A visual comparison of the mechanisms is provided in Fig. 1.3. The designs shown in the figure are based on an identical

payload for both mechanisms in order to make the comparison fair. Based on these designs, the inertia perceived at the end-effector for motions in each direction is computed for each of the mechanisms and compared. The results are reported in Table 1.1. It can be observed that the parallel mechanism yields a much lower inertia in all directions.

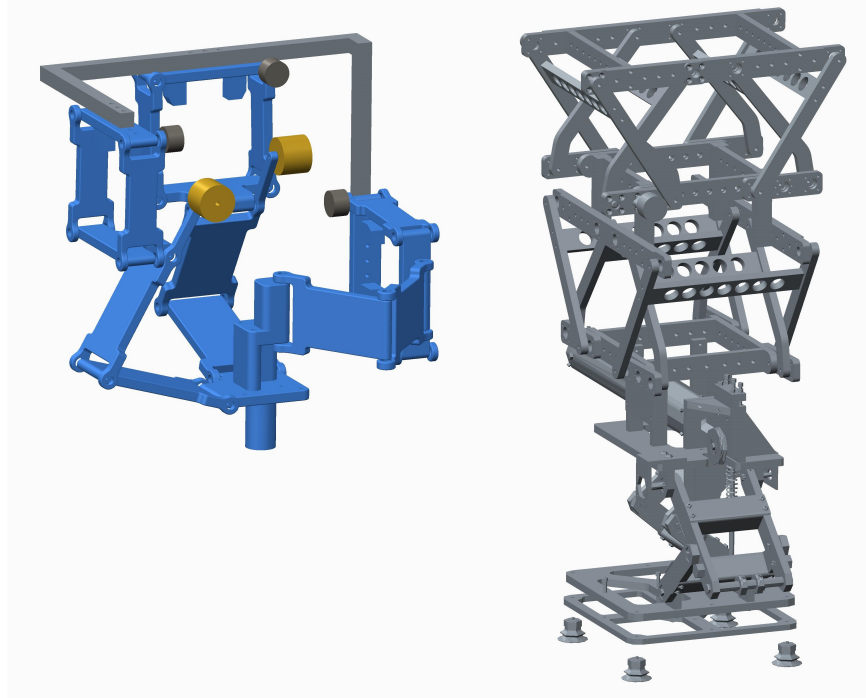


Figure 1.3 – Comparison of size and complexity of the mechanism proposed in this paper (left) and the mechanism proposed in [13] (right).

	Inertia [kg]		
	X-Axis	Y-axis	Z-axis
Serial Mechanism	24.75	18.25	7.5
Parallel Mechanism	9.8	9.8	5.7
Reduction [%]	60.4	46.3	24.0

Table 1.1 – Comparison of the inertia perceived at the end-effector for the serial LIP mechanism proposed in [13] and the parallel LIP mechanism proposed in this paper.

1.4.2 Static Balancing of the LIP mechanism

Although the LIP mechanism proposed in this work is kinematically decoupled, it is not necessarily statically decoupled. Indeed, since the mass of the legs is significant in comparison to

the mass of the parallelograms, the motion of the legs has an effect on the equilibrium configuration of the X and Y parallelograms. In other words, the neutral configuration along the X axis is dependent on the X parallelogram and on the Y leg. Also, the neutral configuration along the Y axis is dependent on the Y parallelogram and the X leg. Moreover, both X and Y legs affect the equilibrium configuration along the Z axis. Although these effects may not be noticeable by a human user, it is desirable to alleviate them completely by balancing the links of the legs of the LIP mechanism whose vertical position coordinate is configuration dependent.

The balancing of the leg links can be performed by mounting counterweights on the first link of the X and Y legs, i.e., the links that are attached to the parallelograms. From a static balancing perspective, each link can be replaced by two point masses located at the joints. Then, the mass of the two links can be considered equivalent to point masses located at three joints, namely, the parallelogram-link joint (PL joint), the link-link joint (LL joint) and the link-mobile-platform joint (LMP joint). Therefore, the mass of the proximal link is distributed between the PL joint and the LL joint, and the mass of the distal link is distributed between the LL joint and the LMP joint. The balancing is performed with respect to the parallelogram linkage. Therefore, the mass located at the PL joint does not need to be balanced. Also, the mass at the LMP joint is at the mobile platform. Since the platform is balanced by the gravity balancing mechanism and since this mass is not dependent on the configuration of the leg, it does not need to be balanced. Therefore, the only mass to be balanced is the one at the LL joint. The equivalent point mass at this joint corresponds to half the mass of the proximal link and half the mass of the distal link, and is located at one link length from the fixed base. A counterweight mounted on the extension of the proximal link behind the PL joint can be used for balancing based on the following balancing equation

$$\ell_{cw}m_{cw} = \frac{1}{2}\ell_{pl}(m_{pl} + m_{dl}), \quad (1.3)$$

where ℓ_{cw} is the distance between the centre of mass of the counterweight and the PL joint, m_{cw} is the mass of the counterweight, ℓ_{pl} is the length of the proximal link, m_{pl} is the mass of the proximal link and m_{dl} is the mass of the distal link. The geometric and mass parameters are illustrated schematically in Fig. 1.4.

Referring to (1.3), there are infinitely many solutions for the distance from the PL joint to the counterweight and the mass of the counterweight. Nonetheless, as shown in [15], a larger counterweight located closer to the pivot yields a lower inertia. In practice, the choice of the counterweights is constrained by mechanical interferences and other design criteria. In the prototype built in this work, the counterweights are located at a distance of $\ell_{cw} = \frac{1}{2}\ell_{pl}$ from the PL pivot, which, when substituted into (1.3), yields

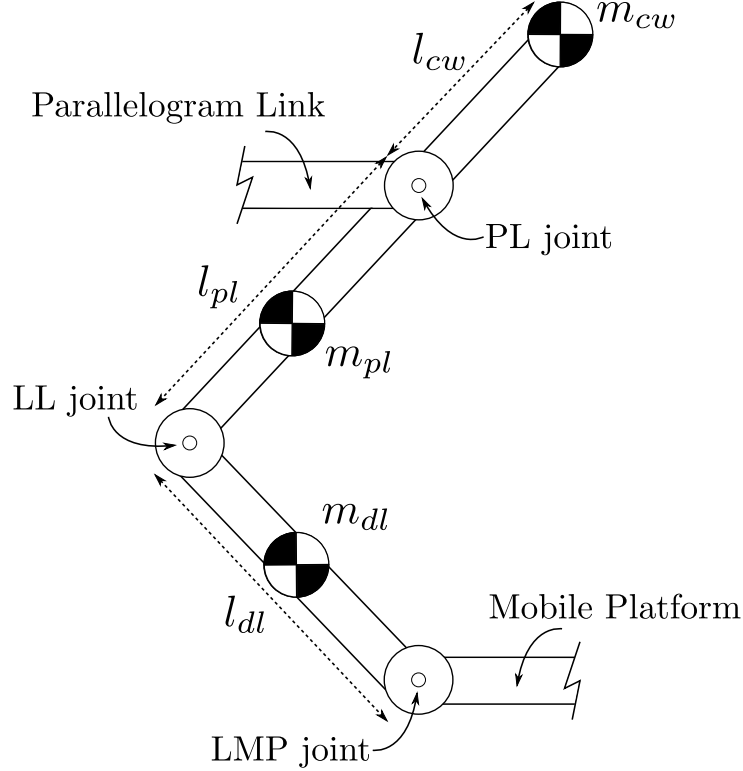


Figure 1.4 – Geometric and mass parameters for the statically balanced mechanism (X- and Y-axis).

$$m_{cw} = m_{pl} + m_{dl}. \quad (1.4)$$

The effect of the static balancing of the legs is demonstrated in the video accompanying this paper, which is described in Section 1.8.

1.4.3 HIA Mechanism

Based on the principle of underactuated redundancy, the dofs of the actuated macro manipulator must correspond to the dofs of the passive mechanism. Therefore, the macro manipulator is also a 3-dof translational robot. In this work, a 3-axis gantry system is used. The X and Y movements are given by the translation of a bridge and trolley system while the Z motion is provided by a telescopic mechanism. The LIP mechanism is attached to the end-effector of the gantry. A gantry system is chosen because it is prevalent in industrial assembly operations (especially in the automotive industry) and also because it provides a very large workspace in which experiments can be performed. The gantry system used here has a maximum workspace of 3.3 m, 2.4 m and 1.3 m, respectively in the X , Y and Z directions. In comparison, the mini-tripteron mechanism has a workspace of 0.102 m along each axis. Note that a larger or smaller gantry system could be used with the same LIP mechanism, the limiting factor with

respect to the LIP mechanism being the possible — and desirable — velocity and acceleration limits of the gantry. The macro-mini system is shown in Fig. 1.5.

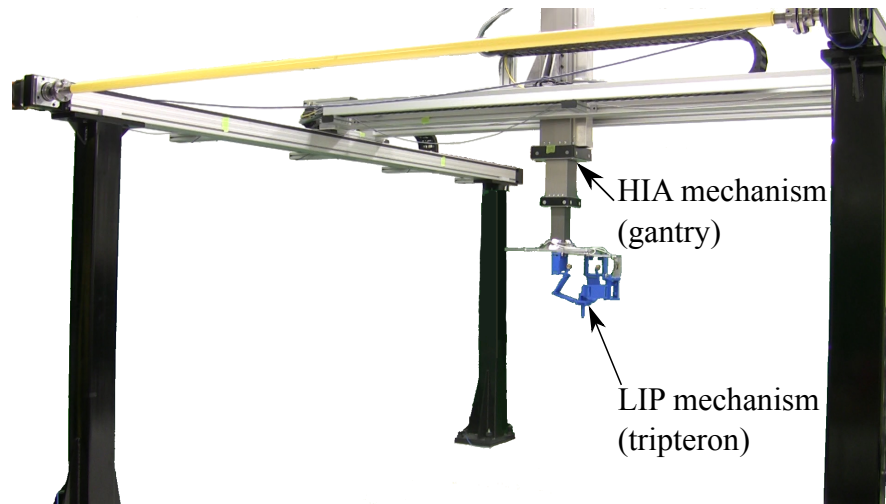


Figure 1.5 – Macro-mini robotic system for pHRI. The mini LIP mechanism is mounted on the end-effector of the macro HIA mechanism.

1.5 Kinematic Performance of the Macro-Mini Robot

A kinematic analysis of the macro-mini underactuated redundant robot is performed in order to determine its capabilities. Since all axes are decoupled in the current mechanism design, each of the three axes can be modeled as a one-dof manipulator. The analysis of a one-dof system is therefore presented. The limits of the experimental prototype of the macro-mini mechanism are then specified and they are used to determine the capabilities of the macro-mini robot.

In a macro-mini architecture, the operational limits are dictated by the size of the LIP mechanism's workspace and by the HIA mechanism's velocity and acceleration limits. In order to obtain an intuitive behaviour using the passive mechanism, the end-effector of the LIP mechanism must be kept within its workspace, meaning that the HIA mechanism must respond quickly enough to always re-position the LIP joints in or close to their neutral configuration. If the HIA mechanism is not fast enough, then the user will reach the limits of the LIP mechanism's workspace and the rendering of a low impedance interaction to the user will be limited and unintuitive.

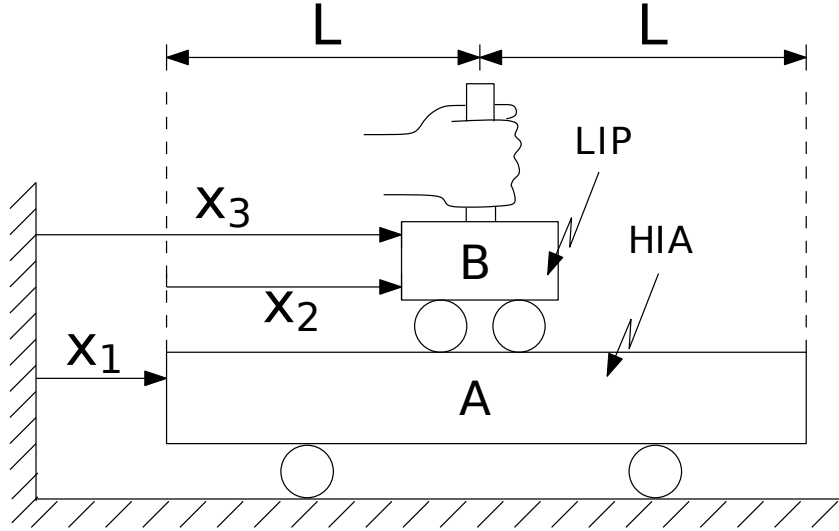


Figure 1.6 – Schematic representation of a 1-dof active-passive mechanism (taken from [12]).

Figure 1.6 represents a simple one-dof passive-active (macro-mini) mechanism. In this model, the rail connection between A and the base represents the macro HIA mechanism while the rail connection between A and B represents the mini LIP mechanism, whose range of motion is $2L$. The position of body A and body B with respect to the fixed frame are respectively noted x_1 and x_3 , while x_2 denotes the position of platform B with respect to platform A. It is now desired to establish the capability of this macro-mini robot to follow the motion produced by the operator (x_3) given the limited range of motion of the LIP mechanism ($-L \leq x_2 \leq L$) and the limited velocity and acceleration of the HIA mechanism. From Fig. 1.6, one has

$$x_3 = x_1 + x_2. \quad (1.5)$$

In order to evaluate the capabilities of the system, it is assumed that x_3 undergoes a harmonic motion, namely

$$x_3 = R \sin(\omega t) \quad (1.6)$$

where t is the time and where ω and R are respectively the frequency and the amplitude of the input motion. Assuming that the HIA mechanism is controlled to keep body B at the neutral (mid-range) configuration of the LIP mechanism, then the HIA mechanism driving body A reacts proportionally and in the same direction as body B . Its motion is therefore expressed as a harmonic motion of identical frequency and phase, namely

$$x_1 = D \sin(\omega t) \quad (1.7)$$

where D is the amplitude of motion of the macro HIA mechanism.

If the amplitude of motion of the end-effector (body B) is larger than the range of motion of the LIP mechanism, then the HIA mechanism must contribute accordingly with a displacement whose amplitude is given by

$$D = R - L. \quad (1.8)$$

Given the velocity and acceleration constraints of the actuator of the HIA mechanism, noted here $\dot{x}_{1,max}$ and $\ddot{x}_{1,max}$, it is possible to determine the maximum amplitude of the HIA mechanism as a function of the frequency of the motion using the first two time derivatives of (1.7), yielding

$$D_{max}^v = \frac{\dot{x}_{1,max}}{\omega}, \quad (1.9)$$

$$D_{max}^a = \frac{\ddot{x}_{1,max}}{\omega^2} \quad (1.10)$$

where D_{max}^v and D_{max}^a represent respectively the maximum amplitudes of x_1 given the velocity and acceleration constraints. Substituting (1.9) into (1.8), the maximum amplitude of input motion x_3 for a given frequency ω and the passive joint's motion range L is obtained as

$$R_{max}^v = \frac{\dot{x}_{1,max}}{\omega} + L. \quad (1.11)$$

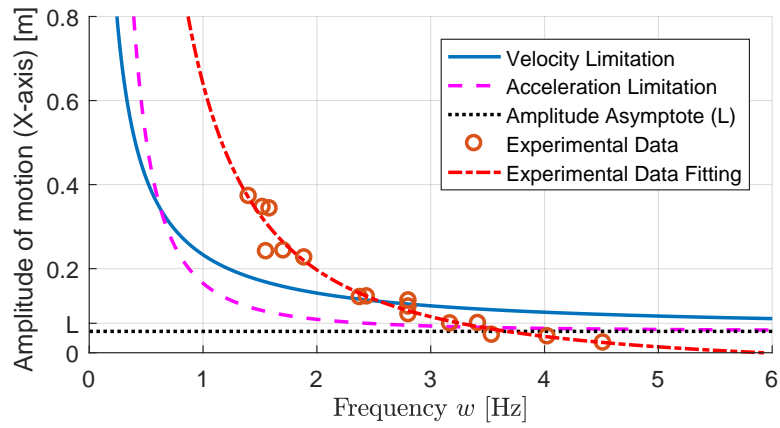
where R_{max}^v stands for the maximum range of input motion that is feasible due to the velocity constraint. Similarly, the relationship for R_{max}^a , the maximum range of input motion that is feasible due to the acceleration constraint, is obtained by substituting (1.10) into (1.8), yielding

$$R_{max}^a = \frac{\ddot{x}_{1,max}}{\omega^2} + L. \quad (1.12)$$

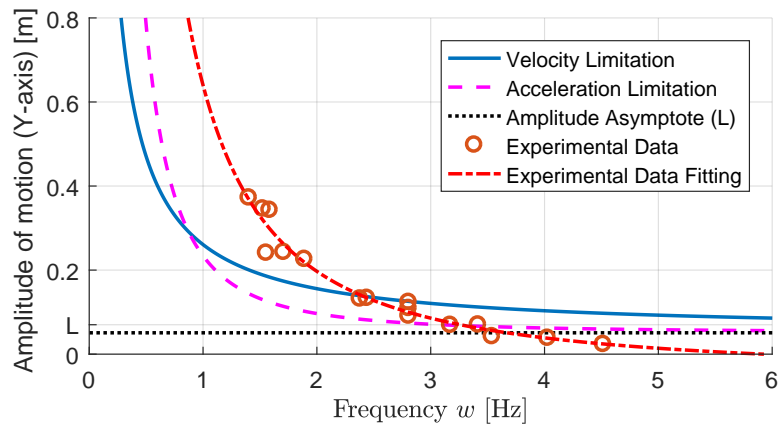
The boundaries on the amplitude of input motion as a function of the input frequency are depicted in Fig. 1.7, for each of the degrees of freedom of the Macro-Mini robot. The graphs are obtained using the limits of the HIA mechanism used in the prototype, which are reported in Table 1.2. The maximum displacement for the LIP mechanism is $L = 0.0508m$, for all axes. It can be observed that both limit curves (for velocity and acceleration) are located above $R = L$ since if the end-effector oscillates within the limits of the LIP mechanism, the input motion is always possible, at any frequency. It can also be observed, from equations (1.11) and (1.12), that a variation in L induces a linear shift of both limit curves. Therefore, this parameter is of great importance for the design of the passive mini mechanism. However, the performance of the actuators of the HIA mechanism is also to be considered to obtain an effective manipulator with a small passive joint range of motion. From Fig. 1.7, it is noted that the X and Y axes are quite similar in terms of limitation. However, the Z axis is clearly limited by its velocity. The experimental data presented in this figure will be explained in Section 1.7. It should also be pointed out that, although increasing L alleviates the limitations of the HIA mechanism, it also increases the size and mass of the LIP mechanism, which reduces the manipulation capabilities of the human operator. Therefore, a compromise must be selected in practice.

	Limitation		
	X-Axis	Y-axis	Z-axis
Velocity [m/s]	1.1451	1.3187	1.0230
Acceleration [m/s^2]	4.5201	7.2321	12.6562

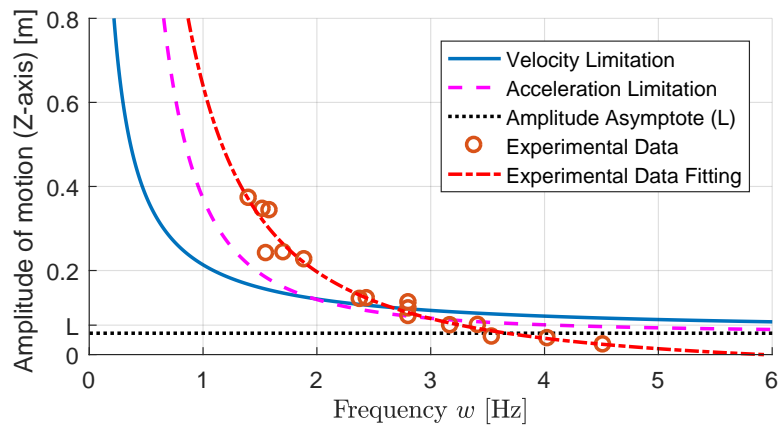
Table 1.2 – Velocity and acceleration limitations of the HIA mechanism used in the prototype.



(a) X-axis limitations



(b) Y-axis limitations



(c) Z-axis limitations

Figure 1.7 – Maximum feasible motion amplitude as a function of the frequency of the input movement.

1.6 Control of the Macro-Mini robot

A block-diagram of the controller is presented in Fig. 1.8. The inner control loop corresponds to the macro motor controller while the outer loop corresponds to the external input management, namely the output given by the mini mechanism which is transformed into an input for the macro mechanism. The inner loop control is lumped into block C_i while the LIP mechanism control is lumped into block C_o . These two blocks are detailed in the following subsections.

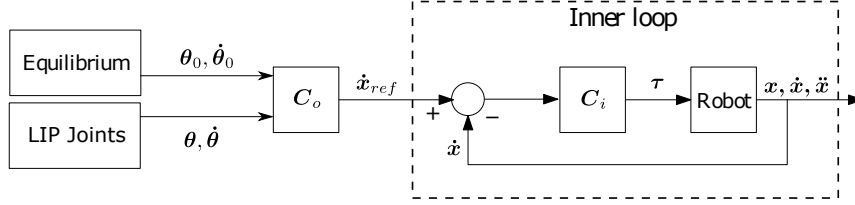


Figure 1.8 – Control architecture of the macro-mini robotic system using the parallel LIP mechanism.

1.6.1 HIA Motor Controller - Block C_i

The controller block C_i represents the HIA mechanism's motor control which consists of a proportional velocity regulator. The control equation is written as

$$\boldsymbol{\tau} = \mathbf{K}_p \boldsymbol{\epsilon}_v + \boldsymbol{\tau}_f = \mathbf{K}_p (\dot{\boldsymbol{x}}_{ref} - \dot{\boldsymbol{x}}) + \boldsymbol{\tau}_f \quad (1.13)$$

where $\boldsymbol{\tau}$ is the torque array for the HIA motors, \mathbf{K}_p is the proportional gain matrix, $\boldsymbol{\epsilon}_v$ is the array of velocity error and $\boldsymbol{\tau}_f$ is a torque array used to compensate for the dry friction. The array of velocity error $\boldsymbol{\epsilon}_v$ corresponds to the difference between the actual HIA mechanism's actuator velocity $\dot{\boldsymbol{x}}$ and the prescribed velocity, which is the output of the LIP control block C_o , noted $\dot{\boldsymbol{x}}_{ref}$.

1.6.2 LIP Mechanism Output - Block C_o

The outer block C_o computes the desired HIA mechanism velocity $\dot{\boldsymbol{x}}_{ref}$ using the LIP mechanism's joint neutral positions and velocities $\{\boldsymbol{\theta}_0, \dot{\boldsymbol{\theta}}_0\}$ and their current position and velocity $\{\boldsymbol{\theta}, \dot{\boldsymbol{\theta}}\}$. Using the angles measured from the sensors in the parallelograms of the LIP mechanism, the end-effector position can easily be translated into Cartesian coordinates. In the description that follows, the arrays $\{\boldsymbol{\theta}, \dot{\boldsymbol{\theta}}\}$ and $\{\boldsymbol{\theta}_0, \dot{\boldsymbol{\theta}}_0\}$ correspond respectively to the end-effector's current state and its equilibrium (neutral) state. The error between the current state and the equilibrium state is defined as $\boldsymbol{\epsilon}_\theta = (\boldsymbol{\theta}_0 - \boldsymbol{\theta})$. Also, since the desired neutral state is the state of rest, one has $\boldsymbol{\theta}_0 = \dot{\boldsymbol{\theta}}_0 = \mathbf{0}$. The output from the LIP mechanism can then be written as

$$\begin{aligned}
\dot{\mathbf{x}}_{ref} &= \mathbf{K}_{P_0}\boldsymbol{\epsilon}_\theta + \mathbf{K}_D\dot{\boldsymbol{\epsilon}}_\theta + \mathbf{K}_f\boldsymbol{\epsilon}_f \\
&= -\mathbf{K}_{P_0}\boldsymbol{\theta} - \mathbf{K}_D\dot{\boldsymbol{\theta}} + \mathbf{K}_f\boldsymbol{\epsilon}_f.
\end{aligned} \tag{1.14}$$

The first term of (1.14), namely $-\mathbf{K}_{P_0}\boldsymbol{\theta}$, is proportional to the relative position of the LIP mechanism with respect to its equilibrium position, with a gain matrix noted \mathbf{K}_{P_0} . The second term of (1.14), namely $-\mathbf{K}_D\dot{\boldsymbol{\theta}}$, is proportional to the velocity array of the LIP mechanism, with a derivative gain matrix noted \mathbf{K}_D . Finally, the third term of (1.14), namely $\mathbf{K}_f\boldsymbol{\epsilon}_f$, is proportional to a filtered (low-pass) version of the position vector $\boldsymbol{\epsilon}_\theta$, noted $\boldsymbol{\epsilon}_f$, with a gain matrix \mathbf{K}_f . This component generates a small and adjustable delay between the LIP mechanism displacement and the HIA mechanism response. It simulates a certain inertia that increases guidance intuitiveness. Indeed, while a very large inertia makes the control difficult, a very low inertia makes the control too responsive. The delay produced by this term can be adjusted either with the gain matrix \mathbf{K}_f or with the cutoff frequency of the low-pass filter.

The main difference between the controller used here and the one described in [13] is that the latter includes a nonlinear term in the computation of the output of the LIP mechanism. The aim of this term was to compensate for the vertical-axis bias introduced by the pendulum effect of the serial LIP mechanism. Since the parallel LIP mechanism used here does not produce any vertical bias, this term is unnecessary. Nevertheless, one could still use this nonlinear function in order to avoid reaching the LIP mechanism's workspace limits. Indeed, with this function, the HIA mechanism's response increases when the LIP mechanism moves away from its equilibrium configuration.

1.7 Experimental Results

The first experiment is related to the kinematic analysis of section 1.5. In order to put the performance of the proposed mechanism in perspective, experimental data was obtained to characterize the movement amplitude versus the maximum attainable frequency for a human arm moving along a given direction in space. This experiment provides a comparison between the proposed robotic system and the kinematic capabilities of the human arm.

The second experiment demonstrates the ability to use the proposed macro-mini mechanism effectively for the insertion of a peg in holes. This experiment is very similar to the one reported in [13]. Both the time and force needed to accomplish the task are measured and analyzed.

The third and final experiment consists in using the admittance controller developed in [13] with a force sensor in order to perform the peg-in-hole task mentioned above, thereby providing a benchmark for the proposed mechanism.

1.7.1 Single-dof experimental kinematic analysis

This first experiment aims at estimating the kinematic capabilities of the human arm and at comparing them with the limitations of the macro-mini mechanism determined above. To this end, the maximum amplitude of movement as a function of the motion frequency have been measured with the simple experimental set-up represented schematically in Fig. 1.9. In this one-dof system, a handle is mounted on a low-friction rail. The limits A and B are positioned at the same distance from the centre point. The time taken by a human user to move the handle as fast as possible from point A to B and from B to A was measured several times. This measurement gives the maximum frequency possible for a specific movement amplitude. This exercise was repeated several times with various distances between limits ($A'-B'$, $A''-B''$) and the results are plotted in Fig. 1.7.

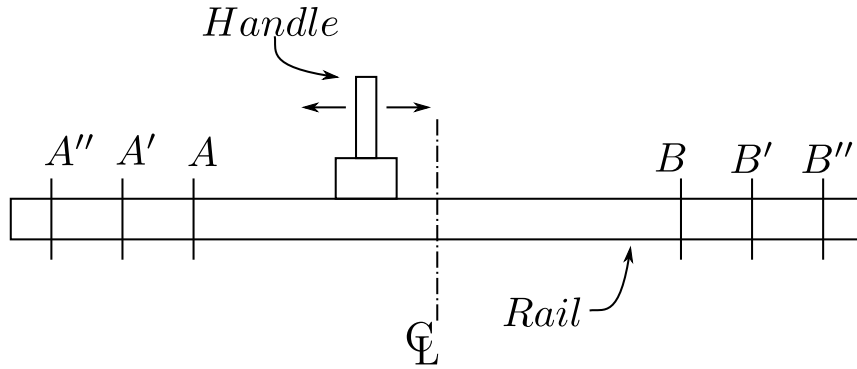


Figure 1.9 – Schematic representation of the experimental setup used to determine the human motion capabilities (amplitude as a function of the frequency).

It can be observed in Figure 1.7 that for small amplitude displacements, the proposed mechanism does not limit the human motion capabilities. However, as the amplitude increases, the mechanism becomes more limiting. Nevertheless, it should be pointed out that the experimental data represents the maximum speed at which a human operator could move the mechanism, which is not necessarily representative of industrial tasks.

1.7.2 Peg-in-Hole Experiment

The second experiment aims at quantifying the ease of fine manipulation and effectiveness of the macro-mini HIA-LIP mechanism. A comparison between the macro-mini HIA-LIP mechanism and a state-of-the-art admittance controller commonly used in pHRI [16] is conducted by performing a peg-in-hole task. The peg and the holed board used in [13] were used for this experiment. Figure 1.10 shows a representation of the holed board used and the sequence that the user has to accomplish. First, the peg starts at the centre of the board (position 0). The user has to move the peg to the first hole (position 1), insert it to a depth of approximately 2.5 cm and then withdraw it. Afterwards the peg has to be moved to the second hole, the

third hole and then the last one, while inserting and withdrawing the peg in each of the holes. After the peg is withdrawn from the last hole, it is returned to its original position at the centre of the board.

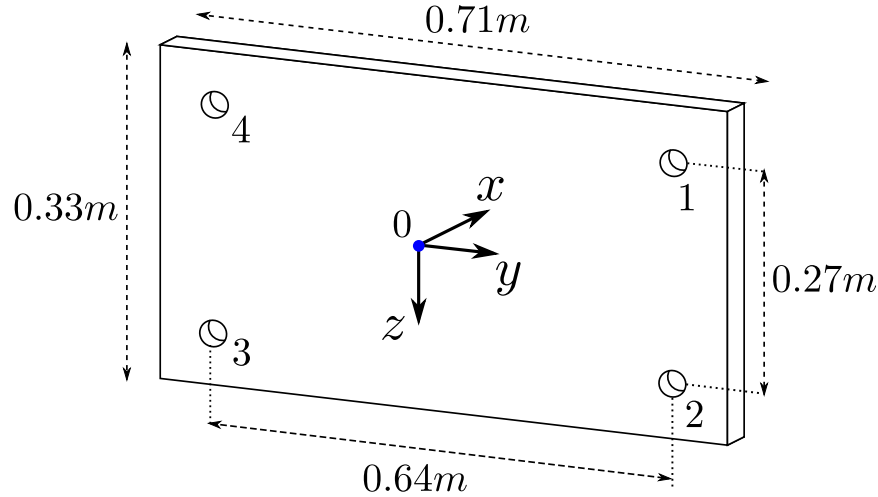


Figure 1.10 – Holed board used for the peg-in-hole experiment.

A group of ten volunteers, all male, aged between 23 and 52 years old participated in the peg-in-hole experiment. First, the subjects were asked to perform five trials of the peg-in-hole sequence as fast as possible using the HIA mechanism only with a force sensor mounted on its end-effector. In this case, the forces measured by the sensor at the base of the peg are used to move the HIA robot using an admittance controller. The admittance parameters used for this task are found heuristically in order to generate the fastest motions possible without producing unstable contacts ($m = 20$ kg and $c = 300$ Ns/m).

In the experiment, the time taken to complete the task was measured, as well as the interaction force between the user and the handle. The measured forces obtained from a typical trial are shown in Fig. 1.11. The peg insertion positions are highlighted at the top of the graph for reference. It can be observed that the forces reach values of the order of 60 N and that the time of execution is just under 25 s.

The subjects were then asked to perform five trials of the same peg-in-hole sequence using the macro-mini HIA-LIP mechanism. The handle of the LIP mini mechanism shown in Fig. 1.2(a) is replaced with the peg which serves as the handle. The peg is mounted horizontally in order to perform the task. A force sensor is attached to the base of the handle to measure the forces — in all three Cartesian directions — applied by the user on the handle when moving the mini LIP mechanism. The force measurements are not used in the controller.

The measured forces obtained from a selected trial are shown in Fig. 1.12. In this case the maximum force is around 2.3 N, which represents about 4% of the maximum forces obtained with the admittance controller. The time of execution is just over 9 s, which is significantly

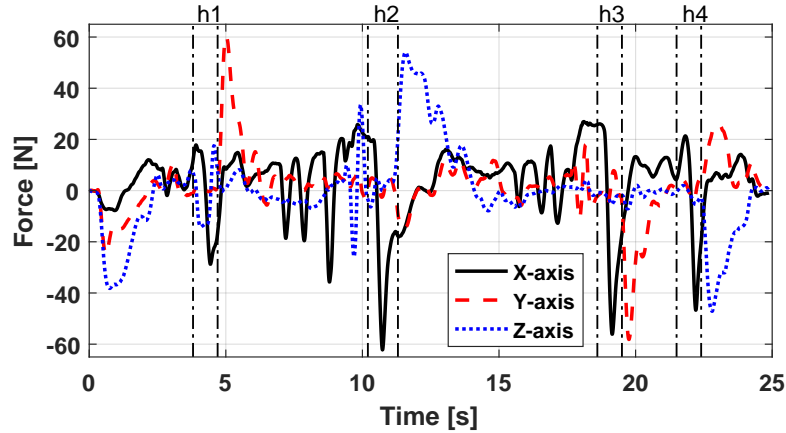


Figure 1.11 – Measured forces for the peg-in-hole experiment with the HIA mechanism only and admittance control.

faster than with the admittance controller.

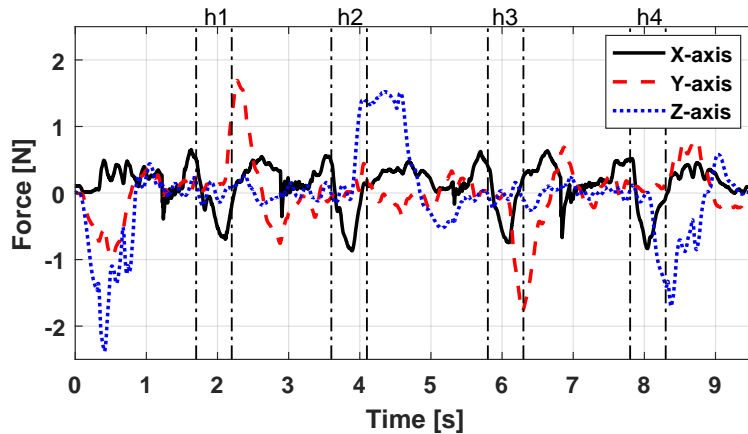


Figure 1.12 – Measured forces for the peg-in-hole experiment with the proposed LIP-HIA mechanism.

For each trial, the average value of the magnitude of the interaction force is computed. The average force and the time required to execute the task for each trial with the admittance control and the LIP-HIA control are then indicated on a graph, shown in Fig. 1.13. From this graph, it is clear that the force needed to perform the experiment is significantly lower when using the LIP-HIA mechanism, the mean force being 0.66 N compared to a mean force of 20.6 N for the admittance controller. The time to execute the task is also 2.4 times smaller with the LIP-HIA mechanism (average time of 11.7 s versus 28.6 s). A multivariate analysis of variance (MANOVA) was performed on the complete data set in order to investigate the statistical difference between the results obtained with the admittance controller and the results obtained using the impedance controller. The p-value obtained is 1.08E-70, which clearly shows that the results obtained with the two types of controllers are significantly

different from each other.

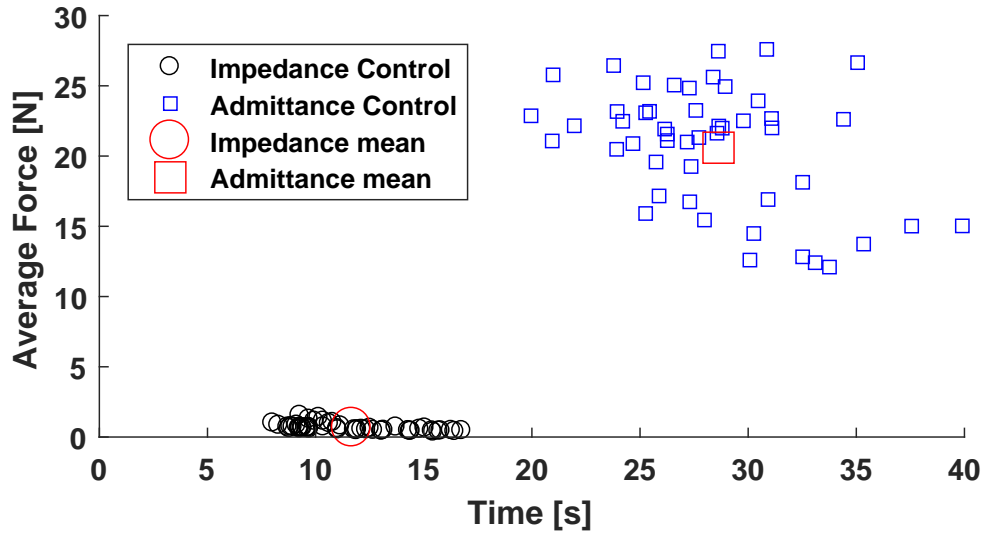


Figure 1.13 – Average force and time to execute the task for the 100 trials performed by the 10 volunteers.

At the end of the two series of trials, the subjects were asked to complete a short survey consisting of 4 questions, namely:

- Q1: Using the first control mode was _____ intuitive than using the second control mode.
- Q2: Using the first control mode was _____ tiresome than using the second control mode.
- Q3: Using the first control mode was _____ responsive than using the second control mode.
- Q4: Using the first control mode, I felt _____ secure than when using the second control mode.

The choice of answers were: 1- Far more, 2- More, 3- As, 4- Less, 5- Far less.

The results of the survey are presented in Table 1.3. Two points stand out from the survey: a large majority of the participants felt that the LIP mechanism was less tiresome and more responsive than the admittance control.

Globally, the results obtained demonstrate that the LIP mechanism provides a very intuitive control of the HIA mechanism. Additionally, the low-impedance mechanism allows the control of the gantry at high speed — movement between the holes — without any instability, while also providing the very precise motion required to insert the peg rapidly.

Question #	Far more -2	More -1	As 0	Less 1	Far less 2	Weighted average
1	0	0	20%	30%	50%	1.3
2	90%	10%	0	0	0	-1.9
3	0	0	0	30%	70%	1.7
4	0	0	0	70%	30%	1.3

Table 1.3 – Results of the qualitative survey on the user experience.

1.7.3 Discussion

Comparing the results reported above for the macro-mini system with those obtained with the admittance controller (see Figs. 1.11, 1.12 and 1.13) and considering the results of the survey, it is clear that the proposed approach yields a much more intuitive and effective interaction than the admittance controller based on a force sensor. Indeed, the forces applied by the human user are much lower and the time to complete the task is much smaller. Also, while inserting a peg in a hole with a small clearance is not a problem with the impedance controller, doing so using the admittance controller is much more difficult. Indeed, when the peg is inserted, the contact between the peg and the internal surface of the hole generates forces that are measured by the sensor. A command is then sent to move the HIA in the opposite direction, which causes a larger force to be measured when the peg hits the other side of the hole. This process may repeat itself and generate oscillations of the peg in the hole leading to instability, which may be a safety hazard. In the tests performed, a bounce-off mechanism was integrated in the admittance control algorithm in order to avoid such oscillations. Nevertheless, the manipulation was less intuitive.

1.8 Video Demonstration

A video demonstrating the effectiveness of the macro-mini robotic system accompanies this paper. The video first shows the intuitive behaviour and the stability of the macro-mini system throughout the large workspace of the HIA mechanism. The static decoupling is then demonstrated by comparing the mechanism’s behaviour with and without the counterweights. A fine motion exercise with high accelerations is then performed that consists in a user drawing on a piece of paper. Finally, the peg-in-hole experiment is shown both with the macro-mini control and the admittance control using a force sensor, comparing the time needed to perform the same task. The advantage of the novel macro-mini system based on the parallel LIP mechanism is clearly apparent on the video. It can be observed that the proposed system allows the user to move freely and intuitively. The task is completed in less than half the time

required with the admittance controller and the motion is much smoother. This is due to the very low mechanical impedance of the physical port of interaction between the user and the robot, which allows the user to display their own impedance.

1.9 Conclusion

In this paper, we introduced a new macro-mini architecture based on a 3-dof parallel LIP mechanism. First, the architecture of the mini LIP mechanism was presented. This architecture is based on the tripteron robot, in which the prismatic actuators were replaced with passive parallelograms equipped with encoders. The kinematic and static decoupling of the LIP mechanism was also addressed. The kinematic performance of the macro-mini system was then determined based on the workspace of the mini mechanism and the velocity and acceleration capabilities of the macro mechanism. A controller in which the motion of the mini mechanism is used as an input to the macro mechanism was then presented. Finally, experimental results clearly demonstrated the effectiveness of the proposed system. A comparison with the capabilities of the human arm showed that the mechanism can provide an intuitive and effective interaction that allows the user to display their own impedance. The intuitive behaviour of the system was clearly demonstrated through a peg-in-hole task and a comparison with an admittance controller based on a force sensor highlights the effectiveness of the proposed approach. The concept of macro-mini HIA-LIP system with underactuated redundancy is highly relevant to manufacturing applications, where intuitiveness and effectiveness are of the utmost importance in order to ensure an ergonomic and productive environment. The application to a 3-dof or 4-dof gantry-type system, as demonstrated in this paper, is particularly relevant since such devices are very common in industry.

1.10 Bibliography

- [1] Stephen P Buerger and Neville Hogan. Complementary stability and loop shaping for improved human–robot interaction. *IEEE Transactions on Robotics*, 23(2):232–244, 2007.
- [2] Alexandre Campeau-Lecours, Simon Foucault, Thierry Laliberté, Boris Mayer-St-Onge, and Clément Gosselin. A cable-suspended intelligent crane assist device for the intuitive manipulation of large payloads. *IEEE/ASME Transactions on Mechatronics*, 21(4):2073–2084, 2016.
- [3] Andrea Cherubini, Robin Passama, André Crosnier, Antoine Lasnier, and Philippe Fraisse. Collaborative manufacturing with physical human–robot interaction. *Robotics and Computer-Integrated Manufacturing*, 40:1–13, 2016.

- [4] Edward Colgate and Neville Hogan. An analysis of contact instability in terms of passive physical equivalents. In *Proceedings, 1989 international conference on robotics and automation*, pages 404–409. IEEE, 1989.
- [5] James Edward Colgate and Neville Hogan. Robust control of dynamically interacting systems. *International journal of Control*, 48(1):65–88, 1988.
- [6] JE Colgate. Coupled stability of multiport systems—theory and experiments. 1994.
- [7] Clement M Gosselin, Mehdi Tale Masouleh, Vincent Duchaine, Pierre-Luc Richard, Simon Foucault, and Xianwen Kong. Parallel mechanisms of the multipterion family: kinematic architectures and benchmarking. In *Proceedings 2007 IEEE International Conference on Robotics and Automation*, pages 555–560. IEEE, 2007.
- [8] CM Gosselin, X Kong, S Foucault, and IA Bonev. A fully decoupled 3-dof translational parallel mechanism. *Parallel Kinematic Machines International Conference*, pages 595–610, 2004.
- [9] Neville Hogan. On the stability of manipulators performing contact tasks. *IEEE Transactions on Robotics and Automation*, 4(6):677–686, 1988.
- [10] Xianwen Kong and Clement M Gosselin. Kinematics and singularity analysis of a novel type of 3-crr 3-dof translational parallel manipulator. *The International Journal of Robotics Research*, 21(9):791–798, 2002.
- [11] Jörg Krüger, Terje K Lien, and Alexander Verl. Cooperation of human and machines in assembly lines. *CIRP annals*, 58(2):628–646, 2009.
- [12] Pascal D Labrecque, Jacques-Michel Haché, Muhammad Abdallah, and Clément Gosselin. Low-impedance physical human-robot interaction using an active–passive dynamics decoupling. *IEEE Robotics and Automation Letters*, 1(2):938–945, 2016.
- [13] Pascal D Labrecque, Thierry Laliberté, Simon Foucault, Muhammad E Abdallah, and Clément Gosselin. Uman: A low-impedance manipulator for human–robot cooperation based on underactuated redundancy. *IEEE/ASME Transactions on Mechatronics*, 22(3):1401–1411, 2017.
- [14] Xavier Lamy, Frédéric Colledani, Franck Geffard, Yvan Measson, and Guillaume Morel. Achieving efficient and stable comanipulation through adaptation to changes in human arm impedance. In *2009 IEEE International Conference on Robotics and Automation*, pages 265–271. IEEE, 2009.
- [15] N Lauzier, C Gosselin, T Laliberté, and P Tremblay. Adaptive gravity compensation of decoupled parallel and serial manipulators using a passive hydraulic transmission.

Proceedings of the Institution of Mechanical Engineers, Part C: Journal of Mechanical Engineering Science, 223(12):2871–2879, 2009.

- [16] Alexandre Lecours, Boris Mayer-St-Onge, and Clément Gosselin. Variable admittance control of a four-degree-of-freedom intelligent assist device. In *2012 IEEE International Conference on Robotics and Automation*, pages 3903–3908. IEEE, 2012.
- [17] Wyatt S Newman and Yuandao Zhang. Stable interaction control and coulomb friction compensation using natural admittance control. *Journal of robotic systems*, 11(1):3–11, 1994.
- [18] Tadele Shiferaw Tadele, Theo de Vries, and Stefano Stramigioli. The safety of domestic robotics: A survey of various safety-related publications. *IEEE robotics & automation magazine*, 21(3):134–142, 2014.
- [19] Richard Q van der Linde and Piet Lammertse. Hapticmaster—a generic force controlled robot for human interaction. *Industrial Robot: An International Journal*, 30(6):515–524, 2003.
- [20] John T Wen, Dan O Popa, Gustavo Montemayor, and Peter L Liu. Human assisted impedance control of overhead cranes. In *Proceedings of the 2001 IEEE International Conference on Control Applications (CCA'01)(Cat. No. 01CH37204)*, pages 383–387. IEEE, 2001.

Chapter 2

Passive Macro-Mini Impedance Control Analysis

This chapter presents to the dynamic analysis of a simplified version of the passive macro-mini mechanism. The term 'passive' is used here to indicate that only the macro-mechanism is actuated while the mini-mechanism is unactuated. A standard impedance controller is firstly described and analyzed. Such a controller is shown to be experimentally unstable when used with the present macro-mini mechanism. Hence an alternative impedance controller is presented and analyzed. While theoretically more complex than the initial controller, it provides a more stable behaviour experimentally. The alternative controller also increases the intuitiveness of the control by reducing the response to high-frequency motion such as hand tremor. This is particularly useful for fine and precise motion.

2.1 Introduction

In the preceding chapter, the advantages of impedance control over admittance control for physical human-robot interaction were demonstrated. Such advantages include a more intuitive and effortless control by the operator of a high-impedance macro mechanism. This effectively reduces the operation times for large motion and at the same time increases the precision and stability of fine motion.

This chapter aims at presenting and analyzing in more detail the impedance controller of a macro-mini architecture. The controller presented in Chapter 1 (see eq. 1.14) is based on an impedance controller presented in [3]. While still considered an impedance controller, it is yet slightly different from the classical impedance control found in literature [1]. Even the controller presented in Chapter 1 and in [3] are slightly different. The former uses a low-pass filtered term of position in order to reduce high-frequency motion such as vibration while the latter uses a nonlinear function of position in order to artificially increase the mini mechanism's workspace. One similarity between these controllers is the absence of virtual mass M_d linked to the mini mechanism acceleration. It will be demonstrated in this chapter that the virtual mass M_d term of the impedance controller causes instability.

The standard impedance controller described in [1] is presented herein. Using the system dynamics, a theoretical stability analysis is performed based on the Laplace transform. Theoretical results are compared with experimental data acquired with a simplified macro-mini architecture. An alternative impedance control — based on the control approach presented in Chapter 1 — is described and analyzed theoretically. Empirical behaviours of the system are compared with the theoretical responses and with the standard impedance controller response.

This chapter is structured as follows. Section 2.2 describes the simplified macro-mini mechanism architecture as well as the experimental setup. The simplified macro-mini system's dynamic are presented in Section 2.3. The standard impedance controller is described in Section 2.4 together with the theoretical stability analysis and the experimental results obtained. Section 2.5 uses the same structure to present the alternative impedance controller. A brief conclusion is given in Section 2.6.

2.2 Experimental Setup

A simplified version of the macro-mini mechanism presented in Chapter1 is used throughout the following two chapters. Indeed, the fact that the mini-tripteron mechanism is decoupled in all three axis allows us to use a single axes mechanism for the study. The results can easily be generalized to a three-axis decoupled mechanism afterwards.

The experimental setup consists of a cart — considered herein as the macro-mechanism — mounted on a linear rail driven by a ball screw which is actuated by a DC motor. A backdrivable motor is mounted on the cart and a pendulum-like link is attached to the shaft of the backdrivable motor. This pendulum is referred to as the mini-mechanism. In this chapter the motor of the pendulum is only used to generate constant impulse for the experimental analysis, the current in the motor is always null at any other given time. A photo and a schematic of the experimental setup are provided in figures 2.1 and 2.2. The macro motor is a RDM-103 (series 2008) built by Servo System, the rail is built by Thomson (model 2HBM100YPHL) and the encoder is a DA15-1000-5VLD (serie 256, ADC-256D) built by Tamagawa. The mini mechanism motor is a Maxon DC motor with integrated encoder (model 500267). The mini mechanism motor is not activate for the test performed in this chapter.

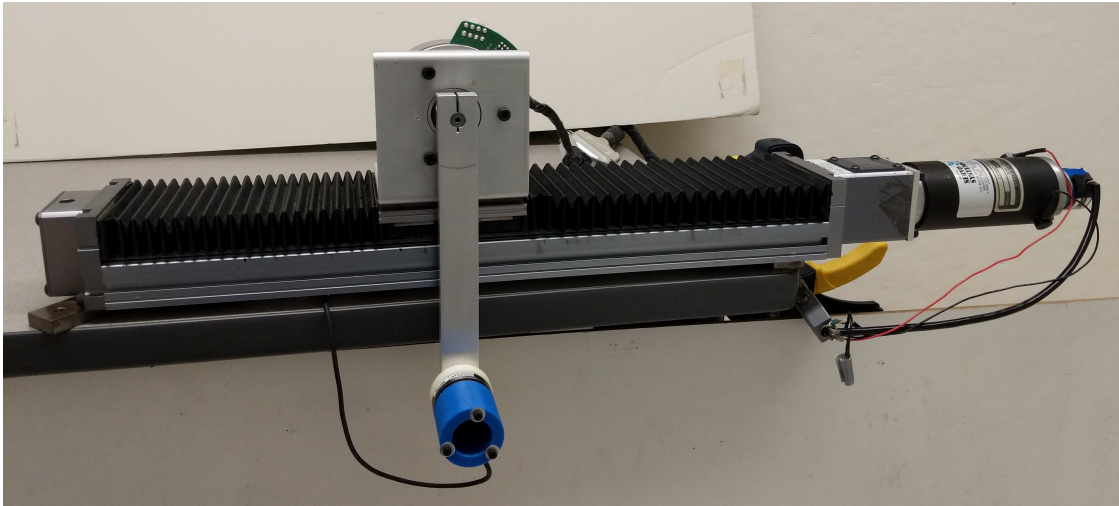


Figure 2.1 – Photo of the macro-mini simplified mechanism used for the experimental test.

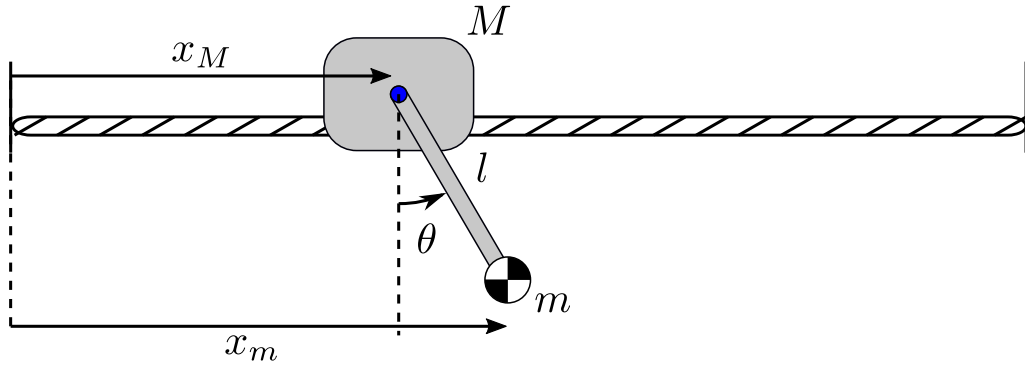


Figure 2.2 – Schematic of the experimental setup used in Chapters 2 and 3.

The table below lists the parameters of the experimental setup with their corresponding variable nomenclature that will be used in the following sections. The subscripts M and m respectively refer to the macro and mini-mechanism.

Definition	Variable	Value
Macro Motor Torque Constant	τ_{kM}	0.0967 Nm/amp
Macro Terminal Resistance	R_M	1.6 Ω
Macro Linear Resolution	x_R	2.5e-6 m
Macro Maximum Current	I_M^{max}	4 amp
Ball Screw Efficiency	η	0.9
Ball Screw Lead	ρ	0.01 m
Macro Mass	M	1.4 kg
Mini Motor Torque Constant	τ_{km}	0.231 Nm/amp
Mini Maximum Current	I_m^{max}	4.06 amp
Mini Mass	m	0.3 kg
Mini Pendulum Length	l	0.19 m
Mini Angular Resolution	θ_R	3.835e-4 rad

Table 2.1 – Macro-mini experimental parameters and variables.

2.3 System's Dynamic Analysis

This section presents the dynamic analysis of the experimental setup shown in figure 2.2. The system has two degrees of freedom. Each one of these degrees of freedom is explored separately and the resulting dynamic equations are then assembled.

Figure 2.3 shows a more detailed schematic of the system with the force and torque being applied to the system. For analysis simplicity, the origin of the reference frame $(\hat{i}, \hat{j}, \hat{k})$ is located on the axis of rotation of the mini mechanism.

The macro mechanism of mass M is mounted on a rail and is moving along the \hat{i} -direction. Its displacement is indicated by vector $\vec{x}_M(t)$. The force $\vec{F}(t)$ applied on the macro is the force generated by the motor, its command coming from the controller.

The mini mechanism rotation is defined by angle $\theta(t)$, the link length is l and end-effector mass is m . The gravitational acceleration is represented by \vec{g} and the velocity of mass m is given by $\vec{v}_m(t)$. An external force $\vec{f}_h(t)$ is applied to the mini mechanism by the user. The torque $\tau_c(t)$ represents the possible torque that can be applied by the motor of the mini mechanism. However, for this chapter, this torque is considered to be zero at any given times ($\tau_c(t) = 0$).

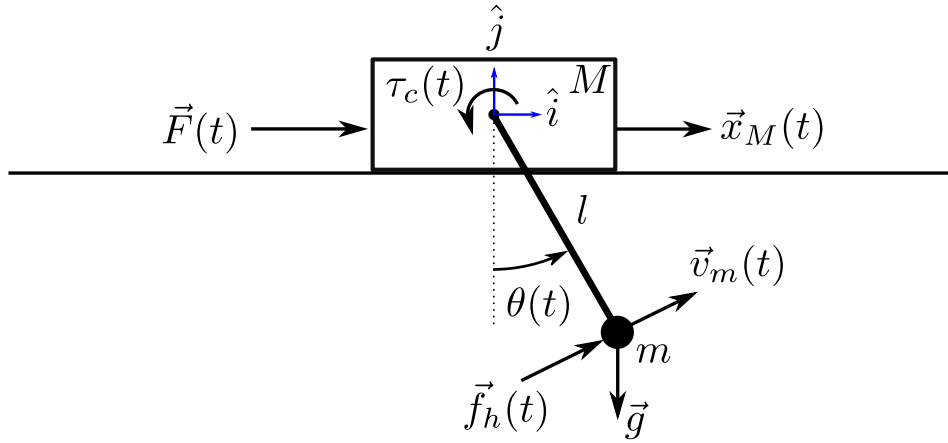


Figure 2.3 – Representation of the simplified macro-mini passive mechanism.

Translational Dynamics of the Macro Mechanism

The dynamic analysis of the translation of the macro mechanism shows that two forces must be considered, the first one being the external force $F(t)$ applied by the actuator and the second being the reaction force $F_m(t)$ applied by the mini mechanism on the macro mechanism, which is due to the acceleration of mass m . The dynamic equation is

$$\sum F_i = M\ddot{x}_M(t) = F(t) - F_m(t) \quad (2.1)$$

where $\ddot{x}_M(t)$ represents the acceleration of the macro mechanism. To obtain the reaction force $F_m(t)$, the velocity of the mini $\vec{v}_m(t)$ must be projected on the \hat{i} -axis, namely

$$v_i(t) = \dot{x}_M(t) + v_m(t) \cos(\theta(t)) \quad (2.2)$$

where $v_m(t)$ can easily be described with the angular velocity $\dot{\theta}(t)$ using

$$v_i(t) = \dot{x}_M(t) + l\dot{\theta}(t) \cos(\theta(t)) \quad (2.3)$$

Since the force is expressed in term of acceleration, the velocity $v_i(t)$ must be differentiated to obtain the acceleration $a_i(t)$

$$a_i(t) = \ddot{x}_M(t) + l\ddot{\theta}(t) \cos(\theta(t)) - l\dot{\theta}^2(t) \sin(\theta(t)) \quad (2.4)$$

Hence the force $F_m(t)$ can be written as follow

$$F_m(t) = m\ddot{x}_M(t) + ml\ddot{\theta}(t) \cos(\theta(t)) - ml\dot{\theta}^2 \sin(\theta(t)) \quad (2.5)$$

Substituting eq. 2.5 into eq. 2.1, the final dynamic equation can then be written as

$$F(t) = (M + m)\ddot{x}_M(t) + ml\ddot{\theta}(t) \cos(\theta(t)) - ml\dot{\theta}^2(t) \sin(\theta(t)) \quad (2.6)$$

Using the small angle approximations $\{\sin(\theta) \approx \theta; \cos(\theta) \approx 1\}$ and considering the angular velocity to be very small $\{\dot{\theta}(t) \approx 0\}$ further simplifies the dynamic equation, yielding

$$F(t) = (M + m)\ddot{x}_M(t) + ml\ddot{\theta}(t) \quad (2.7)$$

Rotational Dynamics

The dynamic analysis is then completed for the second degree of freedom (rotation around axis \hat{k}). The dynamic equation is

$$\sum \tau_{\hat{k}}(t) = I\ddot{\theta}(t) \quad (2.8)$$

where I represents the moment of inertia of mass m (considered a point mass) in rotation around axis \hat{k} and is expressed by

$$I = ml^2 \quad (2.9)$$

There are four terms to the torque summation. The first one being the torque directly applied to the mini mechanism through an electric motor, denoted here $\tau_c(t)$. The second term $\tau_g(t)$ is related to gravity, the third term $\tau_x(t)$ is a reaction torque created by the macro acceleration $\ddot{x}_M(t)$ and the fourth term is the torque $\tau_h(t)$ generated by the external force $f_h(t)$ applied by the user on the mini. These torques are given below.

$$\sum \tau_{\hat{k}}(t) = ml^2\ddot{\theta}(t) = \tau_c(t) + \tau_g(t) + \tau_x(t) + \tau_h(t) \quad (2.10)$$

$$\tau_c(t) = 0$$

$$\tau_g(t) = -mgl \sin \theta(t) \quad (2.11)$$

$$\tau_x(t) = -ml\ddot{x}(t) \cos \theta(t)$$

$$\tau_h(t) = lf_h(t)$$

Therefore the second dynamic equation can be written as

$$ml^2\ddot{\theta}(t) = -mgl \sin(\theta(t)) - ml\ddot{x}_M(t) \cos(\theta(t)) + lf_h(t) \quad (2.12)$$

Using the small angle approximation and dividing all terms by l in eq. 2.12 yields the final dynamic relation for the rotation.

$$ml\ddot{\theta}(t) = f_h(t) - mg\theta(t) - m\ddot{x}_M(t) \quad (2.13)$$

Complete Dynamic Equation

The two dynamic equations derived above can be combined to obtain a dynamic equation that is independent from $\ddot{x}_M(t)$. Solving eq. 2.13 for $\ddot{x}_M(t)$ yields

$$\ddot{x}_M(t) = \frac{1}{m} \left[-ml\ddot{\theta}(t) - mg\theta(t) + f_h(t) \right] \quad (2.14)$$

$$\ddot{x}_M(t) = -l\ddot{\theta}(t) - g\theta(t) + \frac{f_h(t)}{m} \quad (2.15)$$

Substituting eq. 2.15 into eq. 2.7 then leads to

$$F(t) = f_h(t) \frac{M+m}{m} - g(M+m)\theta(t) - Ml\ddot{\theta}(t). \quad (2.16)$$

Equation 2.16 will be used extensively in the following sections to obtain the theoretical response of the system with different controllers. It should be pointed out that this dynamic equation is only valid for small angles ($\theta(t) \ll 1$) and that friction was neglected in the analysis.

2.4 Standard Impedance Controller

Standard impedance control consists in linking motion and force using a basic mechanical system consisting of a virtual mass, a virtual damping and a virtual stiffness. A combination of these three components can be used to represent most dynamic interactions. Such a controller was firstly described in [1].

Impedance control can be divided into two categories: impedance and admittance control. Unfortunately, too often in the literature the term impedance control is used for admittance control.

Admittance controllers use a force input — usually measured by a force sensor at the robot control point (e.g. wrist of a serial robot) — and convert it into a desired motion using a combination of virtual mass, damping and stiffness. The system reactivity depends on the combination of these elements. For a specific force input, the system will accelerate faster if the virtual mass is smaller. Admittance control is widely used in industry since it provides a simple control that can be adjusted for specific tasks and because a force sensor is easily integrated. However there are some disadvantages to admittance control. Indeed, the controller can be adjusted for large and quick motion by reducing the virtual mass. For finer motion, such as inserting a peg in a hole, the virtual mass needs to be increased to reduce high frequency motion. Hence the controller cannot be used for a wide variety of motion and needs to be modified on-line.

On the contrary, impedance control uses a motion as input and transforms this into a desired force to be applied on the system. The relation between the motion and the force still comes from a combination of a virtual mass, damping and stiffness. If the motion measurement mechanism is properly designed to have very low-impedance, the same combination of virtual

mass, damping and stiffness can be used for both fine and large motion. This is due to the fact that the impedance felt by the user is reduced to the impedance of the measurement mechanism instead of the whole system when using a force sensor. The downside of the impedance control is the design of the motion measurement mechanism. It must be small enough to fit at the end-effector of the controlled system, but not too small to ensure the mechanism workspace's allows for intuitive control.

This section aims at presenting an analysis of using such a standard impedance controller with the mini-macro architecture presented in Chapter 1. The controller presented here was implemented and experimental results are compared to those obtained with the theoretical stability analysis.

2.4.1 Controller Description

The controller described here uses all three characteristic terms: virtual mass M_d , virtual damping C_d and virtual stiffness K_d . The impedance control aims at linking the input motion of the mini mechanism to a desired force to be applied on the macro mechanism. In this case, the input motion corresponds to the mini mechanism motion $\{p(t), \dot{p}(t), \ddot{p}(t)\}$ and the output corresponds to the force $F(t)$ to be applied on the macro mechanism. The impedance controller equation is written as

$$F(t) = M_d \ddot{p}(t) + C_d \dot{p}(t) + K_d p(t) \quad (2.17)$$

It is noted that, in order to ease the reading, the gain units are not written explicitly in the following subsections. Indeed, the virtual mass M_d units are [kg], the virtual damping C_d units are [kg/s] and the virtual stiffness K_d units are [kg/s²] or more commonly used [N/m].

Since the mini mechanism motion is measured using an angular encoder, the motion described by $\{p(t), \dot{p}(t), \ddot{p}(t)\}$ is converted into angular motion using the following relations.

$$\begin{aligned} p(t) &= l \sin(\theta(t)) \\ \dot{p}(t) &= l \dot{\theta}(t) \cos(\theta(t)) \\ \ddot{p}(t) &= l \ddot{\theta}(t) \cos(\theta(t)) - l \dot{\theta}^2(t) \sin(\theta(t)) \end{aligned} \quad (2.18)$$

Using the small angle approximations and assuming that $\dot{\theta}^2(t)$ is small, these relations simplify to

$$\begin{aligned}
p(t) &\approx l\theta(t) \\
\dot{p}(t) &\approx l\dot{\theta}(t) \\
\ddot{p}(t) &\approx l\ddot{\theta}(t)
\end{aligned} \tag{2.19}$$

The controller equation can be rewritten with these approximations, namely

$$F(t) = M_d l \ddot{\theta}(t) + C_d l \dot{\theta}(t) + K_d l \theta(t) \tag{2.20}$$

Since the DC motor is controlled using a current $I_M(t)$ input, the controller output force $F(t)$ must be converted into a current. The force $F(t)$ can be converted into a torque $\tau_M(t)$ using the following equation

$$\tau_M(t) = \frac{\rho}{2\pi\eta} F(t) \tag{2.21}$$

The motor torque constant τ_{kM} is then used get the current from the torque $\tau_M(t)$, namely

$$I_M(t) = \frac{\tau_M(t)}{\tau_{kM}} \tag{2.22}$$

where ρ represents the ball screw lead (in metre) and η corresponds to the ball screw efficiency.

2.4.2 System Transfer Function $H(s)$

With the dynamic eq. 2.16 and the standard impedance controller eq. 2.20, the system response $\theta(t)$ caused by an external perturbation $f_h(t)$ can be theoretically computed using Laplace analysis. In this case, the system must return to its equilibrium state $\{\theta(t) = 0, \dot{\theta}(t) = 0, \ddot{\theta}(t) = 0\}$ as fast as possible when it is perturbed.

Equation 2.16 can be substituted into eq. 2.20 to yield

$$f_h(t) \frac{M+m}{m} - g(M+m)\theta(t) - Ml\ddot{\theta}(t) = M_d l \ddot{\theta}(t) + C_d l \dot{\theta}(t) + K_d l \theta(t) \tag{2.23}$$

Solving for the external force $f_h(t)$ then yields

$$f_h(t) = \frac{m}{m+M} \left[M_d l \ddot{\theta}(t) + C_d l \dot{\theta}(t) + K_d l \theta(t) + g(m+M)\theta(t) + Ml\ddot{\theta}(t) \right] \tag{2.24}$$

Taking the Laplace transform of the above equation gives

$$F_H(s) = \Theta(s) \frac{m}{m+M} \left[(M_d l + M l) s^2 + (C_d l) s + (K_d l + g(M + m)) \right] \quad (2.25)$$

where $F_H(s)$ and $\Theta(s)$ are respectively the Laplace transform of $f_h(t)$ and $\theta(t)$. The system's transfer function $H(s)$ is given by

$$H(s) = \frac{\Theta(s)}{F_H(s)} = \frac{m+M}{mMl} \left[\frac{1}{a_2 s^2 + a_1 s + a_0} \right] \quad (2.26)$$

with

$$\begin{aligned} a_0 &= \left(\frac{K_d}{M} + \frac{g}{l} \left(1 + \frac{m}{M} \right) \right) \\ a_1 &= \frac{C_d}{M} \\ a_2 &= \frac{M_d}{M} + 1 \end{aligned} \quad (2.27)$$

The transfer function $H(s)$ of the system will be used in the next subsections for the theoretical stability analysis.

2.4.3 Theoretical Stability Analysis

One of the most common external perturbations used for system stability analysis is the unit-impulse — Dirac delta function — because it represents common real-life perturbations and its representation in the Laplace domain is quite simple (see eq. 2.28).

$$\mathcal{L}\{\delta(t)\} = 1 \quad (2.28)$$

Setting the external perturbation to $F_H(s) = 1$ in eq. 2.26 yields

$$\Theta(s) = \frac{m+M}{mMl} \left[\frac{1}{\left(\frac{M_d}{M} + 1 \right) s^2 + \frac{C_d}{M} s + \left(\frac{K_d}{M} + \frac{g}{l} \left(1 + \frac{m}{M} \right) \right)} \right] = \frac{m+M}{mMl} \left[\frac{1}{a_2 s^2 + a_1 s + a_0} \right] \quad (2.29)$$

Now, this expression represents a second-order homogeneous differential equation. The fractional coefficient $\frac{m+M}{mMl}$ is an amplitude factor, only affecting the magnitude of the system response but not its behaviour. The above relation can be simplified and written as

$$\Theta(s) = G \frac{1}{a_2 s^2 + a_1 s + a_0} \quad (2.30)$$

In this form, one can see that the equation represents the transfer function of a second-order low-pass filter. Therefore the amplitude response $\theta(t)$ will be higher for low-frequency perturbations $f_h(t)$ than for high-frequency ones. Furthermore, the system's equation can be conveniently described in terms of a damping ratio and cutoff frequency $\{\zeta, \omega_0\}$. A common formulation for a second-order low-pass filter is presented in eq. 2.31.

$$H_{LP}(s) = K \frac{1}{s^2 + 2\zeta\omega_0 s + \omega_0^2} \quad (2.31)$$

From eq. 2.26 and eq. 2.31, the following relation can be stated

$$\begin{aligned} \omega_0^2 &= \frac{a_0}{a_2} \\ 2\zeta\omega_0 &= \frac{a_1}{a_2} \end{aligned} \quad (2.32)$$

and the relations between the controller's gains $\{M_d, C_d, K_d\}$ and the filter parameters $\{\zeta, \omega_0\}$ can be obtained from eq. 2.32 as

$$\begin{aligned} \omega_0^2 &= \frac{a_0}{a_2} = \frac{\left(\frac{K_d}{M} + \frac{g}{l}\left(1 + \frac{m}{M}\right)\right)}{\frac{M_d}{M} + 1} = \frac{K_d + \frac{g}{l}(m + M)}{M_d + M} \\ \omega_0 &= +\sqrt{\frac{K_d + \frac{g}{l}(m + M)}{M_d + M}} = +\sqrt{\frac{K_d + \frac{g}{Al}(m + M)}{M_d + M}} \\ 2\zeta\omega_0 &= \frac{a_1}{a_0} = \frac{\frac{C_d}{M}}{\frac{M_d}{M} + 1} = \frac{C_d}{M_d + M} \\ 2\zeta\omega_0 &= 2\zeta\sqrt{\frac{K_d + \frac{g}{l}(m + M)}{M_d + M}} \end{aligned} \quad (2.33)$$

Using the last two lines above, one has

$$2\zeta\sqrt{\frac{K_d + \frac{g}{l}(m + M)}{M_d + M}} = \frac{C_d}{M_d + M} \quad (2.34)$$

Squaring both sides and solving for ζ then gives

$$\zeta = \frac{C_d}{2\sqrt{(M_d + M)(K_d + \frac{g}{l}(m + M))}}$$

$$\omega_0 = +\sqrt{\frac{K_d + \frac{g}{l}(m + M)}{M_d + M}}.$$
(2.35)

Hence, from eq. 2.35, the damping ratio is a function of all gains while the cutoff frequency is only a function of the virtual mass and stiffness.

The desired system response can be described using the damping ratio ζ , the angular cutoff frequency ω_0 and the decay ratio $\alpha = \zeta\omega_0$. Parameter α gives the decaying exponential rate of the response. If its value is high, the system response decreases rapidly while if its value is low, the system response decays slowing to the equilibrium state.

A value of ($\zeta > 1$) means that the system is over-damped. This means that the system will tend to slow down while reaching the equilibrium position without oscillating around the equilibrium position. A value in the domain ($0 < \zeta < 1$) means that the system is under-damped and will therefore overshoot the equilibrium position and oscillate around it before reaching equilibrium. A critically damped system occurs when ($\zeta = 1$). At this damping ratio, the system will have the fastest response without oscillation. A critically damped system would theoretically be the best system in terms of rapidity and stability. However in practice, due to unmodeled and uncontrolled forces such as friction, an over-damped system is preferable for stability.

Above the cutoff frequency ω_0 the system response is decreasing linearly with the perturbation frequency. In our case, we would like to have the same response for much of the human bandwidth domain, hence the angular cutoff frequency must be higher than the standard human arm motion frequency. Herein, the same cutoff frequency used in Chapter 1 is again employed ($\omega_0 = 100$ rad/s).

Since there are three variables $\{M_d, C_d, K_d\}$ and only two equations (see eq. 2.35), there are infinitely many solutions. For the purpose of this analysis, one of the gains is used as an independent variable. The remaining gains are functions of it. The variable gain used below is the virtual mass M_d . One can then write

$$K_d = \omega_0^2(M_d + M) - \frac{g}{l}(m + M)$$

$$C_d = 2\zeta\omega_0(M_d + M)$$
(2.36)

Using the following two conditions for stability

$$\begin{aligned} M_d &\geq 0 \\ K_d &\geq 0 \end{aligned} \tag{2.37}$$

the following relation is obtained

$$M_d > \frac{g}{l\omega_0^2}(m + M) - M \tag{2.38}$$

The result of using the virtual stiffness K_d instead as the independent variable is presented below. The equations are formulated as

$$\begin{aligned} M_d &= \frac{K_d + \frac{g}{l}(m + M)}{\omega_0^2} - M \\ C_d &= \frac{2\zeta}{\omega_0}(K_d + \frac{g}{l}(m + M)) \end{aligned} \tag{2.39}$$

with the following constraints

$$\begin{aligned} K_d &\geq 0 \\ K_d &\geq M\omega_0^2 - \frac{g}{l}(m + M) \end{aligned} \tag{2.40}$$

Note that the virtual damping C_d cannot be used as an independent variable since it appears only in the expression of the damping ratio ζ (see eq. 2.35).

Since the robot is position controlled — related to $\theta(t)$ — it is more logical to set the virtual stiffness K_d as the independent variable. This is the implementation used in the following experimental section.

Figure 2.4 shows three different simulated responses $\theta(t)$. All responses were computed using $K_d = 20000 \text{ kg/s}^2$. The remaining gains were computed using eq. (2.39).

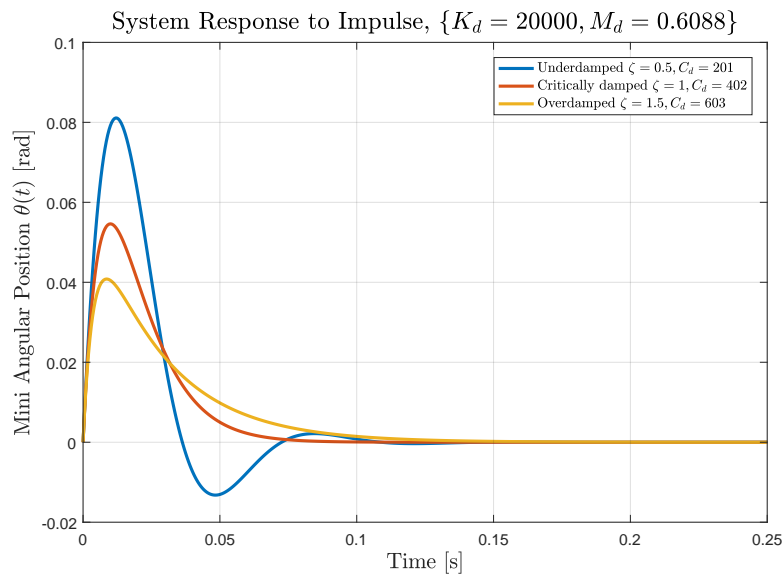


Figure 2.4 – Simulated response for over-damped $\zeta = 1.5$, under-damped $\zeta = 0.5$ and critically damped $\zeta = 1$ sets of gains.

2.4.4 Experimental Stability Analysis

The previously presented theoretical analysis provides some insight on how to adjust the various control gains $\{M_d, C_d, K_d\}$ to obtain a stable system. However, the dynamic model might not be precise enough to directly use these computed gains. In this case, an experimental method might be used to adjust the gains in sequence, starting with the virtual stiffness K_d , followed by the virtual damping C_d and finally with the virtual mass M_d . The method described in [4] is used here to experimentally set the controller gains.

In order to generate reliably constant impulse on the mini mechanism, a torque impulse was sent to the mini-mechanism motor. The amplitude of the impulse is 2 amp and its duration is 0.1 s.

Setting K_d with $M_d = C_d = 0$

Initially, the virtual mass and damping are set to zero and the virtual stiffness is slowly increased until the system response is quick with small damped oscillation. Figure 2.5 shows the response of the mini and macro mechanism.

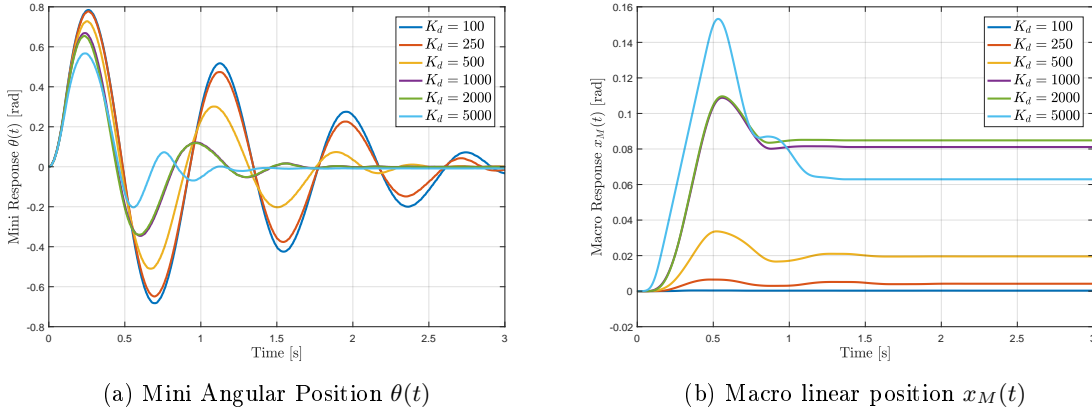


Figure 2.5 – Experimental response for multiple virtual stiffness K_d values. $\{M_d = C_d = 0\}$

From figure 2.5, an appropriate domain for the virtual stiffness K_d seems to be around $[1000, 2000]$. Note that this domain was qualitatively selected and one could use a value outside it without problem.

Figure 2.6 shows a comparison between the experimental and simulated response with $\{K_d = 1000, C_d = 0, M_d = 0\}$. The simulated response is unstable, oscillating indefinitely like a pendulum. This is to be expected when using a frictionless theoretical model controlled only using the mini angular position $\theta(t)$. Indeed, in this case the macro velocity is directly linked with the oscillating position of the mini, without any other damping control. Therefore, the macro motion sustains the mini mechanism oscillating motion. This behaviour could also have

been predicted from the damping ratio coefficient (see eq. 2.35) which is null in this specific case.

In the experimental setup, the damping comes from the friction at the mini mechanism rotation point. Also, the macro mechanism does not move directly at the desired velocity due to friction at the ball screw.

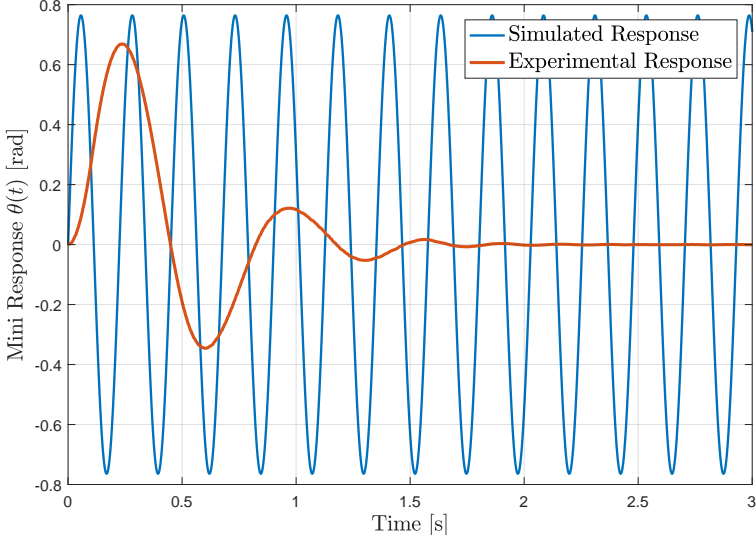


Figure 2.6 – Comparison of a simulated and an experimental response for a selected virtual stiffness value. $\{K_d = 1000, M_d = C_d = 0\}$

Setting C_d , with $M_d = 0$ and $K_d = 1000$

Using the value $K_d = 1000$ as virtual stiffness, the virtual damping is now increased slowly until the oscillations around the equilibrium position are reduced. The experimental results are shown in figure 2.7.

Increasing the virtual damping C_d reduces the macro and mini oscillations around their respective equilibrium position. This effect is better seen when comparing the curve $C_d = 50$ and $C_d = 800$. However, if the damping is too high the macro position tends to return closer to its initial position. This is due to the fact that while the mini position quickly returns to its equilibrium position $\theta(t) = 0$, the velocity is not immediately null at this moment, therefore the macro command velocity $\dot{x}(t)$ is also non-zero. The macro and mini will therefore move on the opposite direction — with regards to the initial impulse direction — with a decreasing velocity while the mini position remains fairly close to its equilibrium.

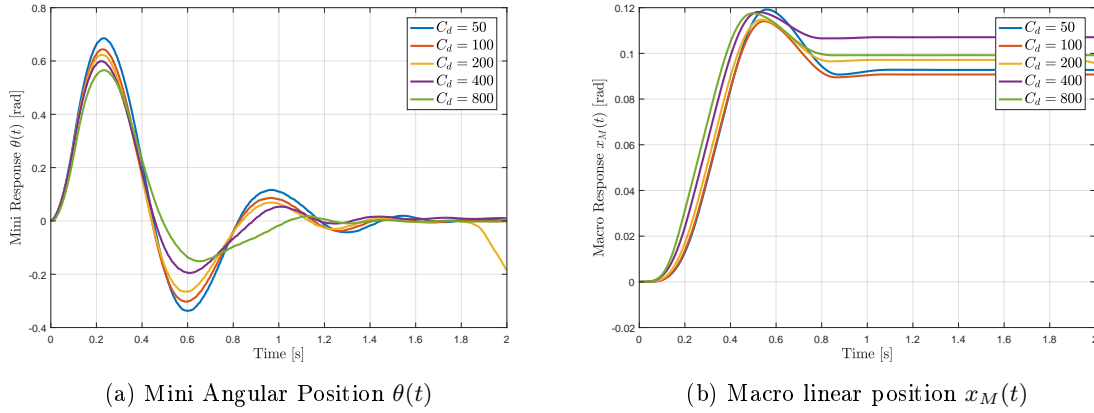


Figure 2.7 – Experimental response for multiple virtual damping C_d values. $\{K_d = 1000, M_d = 0\}$

Using these results, the virtual damping C_d should be chosen with a value in the domain $[400; 800]$. With these two gains, the theoretical damping ratio should respectively be $\zeta = 5.125$ and $\zeta = 10.25$, which effectively represent over-damped systems. A comparison of the experimental and simulated response is shown in figure 2.8 for the following gain settings: $M_d = 0$, $C_d = 400$, $K_d = 1000$. The simulated response corresponds to an over-damped system while the experimental response corresponds to an under-damped response.

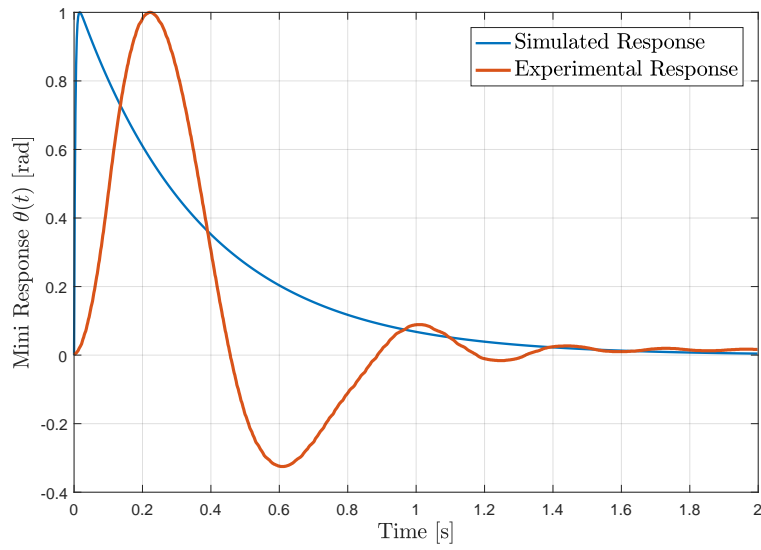


Figure 2.8 – Comparison between simulated and experimental response for a selected virtual stiffness and damping. $\{K_d = 1000, C_d = 400, M_d = 0\}$

Setting M_d , with $K_d = 1000$ and $C_d = 400$

Using the previously obtained virtual stiffness $K_d = 1000$ and damping $C_d = 400$, the virtual mass M_d can now be slowly increased in order to reach a good compromise between quick response and intuitive motion. The relation between the virtual mass M_d and the damping ratio can easily be seen in eq. 2.35. An increase in the virtual mass M_d reduces the damping ratio ζ . At a specific mass — in this particular case $M_d = 35.37$ kg — the system shall become critically damped. Hence the user must be careful when tuning this parameter. Simulated response for different virtual masses are shown in figure 2.9. As expected, the mini response becomes underdamped as the virtual mass is increased.

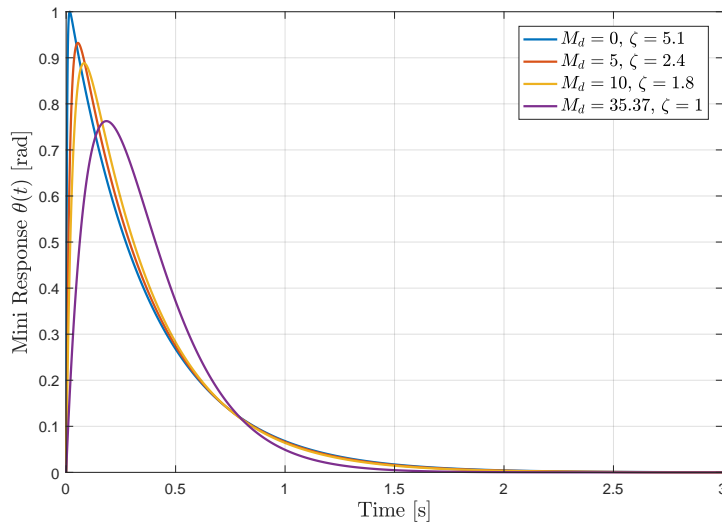
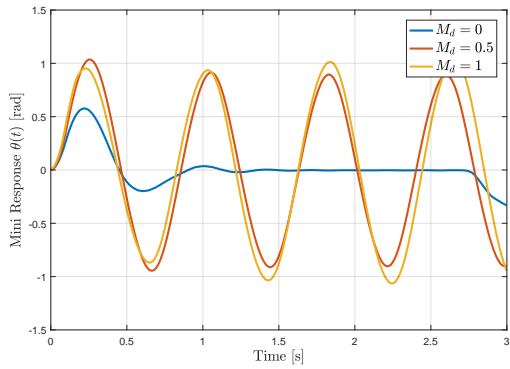


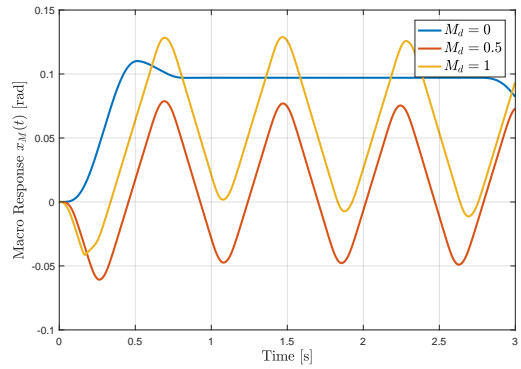
Figure 2.9 – Theoretical response for different values of the virtual mass. Curves were normalized in amplitude. $\{K_d = 1000, C_d = 400\}$

In the experiment however, the system becomes unstable as soon as the virtual mass is non-zero. Figure 2.10 shows the experimental response for $M_d = 0$, $M_d = 0.5$ and $M_d = 1$.

The discrepancy between the theoretical and experimental response can be explained by several factors. First, it must be noted that the acceleration signal $\ddot{p}(t)$ is obtained by numerically differentiating (twice) the position signal $p(t)$. Such a numerical process is very sensitive to signal noise. Another explanation could be the initial measured acceleration that is very high due to the initial numerical difference. Such a value will induce a jerk motion to the macro mechanism.



(a) Mini Angular Position $\theta(t)$



(b) Macro linear position $x_M(t)$

Figure 2.10 – Experimental response for multiple virtual mass M_d values. $\{K_d = 1000, C_d = 400\}$

2.4.5 Discussion

The standard impedance controller (see eq. 2.17) was analyzed theoretically using the Laplace transform analysis. While this method is quite powerful, discrepancies between the model and the experimental setup render its use less efficient.

In theory, a controller with only a stiffness gain K_d should not be stable. However experiments showed the response to be underdamped due to unmodeled friction at the mini mechanism joint.

Another difference is the response obtained when using a non-zero virtual mass M_d . In theory the virtual mass M_d can be tuned in order to obtain a quicker response (i.e. reducing the damping ratio). However the operator must take extra care with this gain since it can make the controller underdamped. In the case presented, the theoretical virtual mass M_d to obtain a critically damped system was about 35 kg. In practice, even a mass of 0.5 kg renders the system unstable. Such a difference can be explained in part by the numerical differentiation process used, which is quite sensitive to signal noise.

With regards to the experimental results obtained with a non-zero virtual mass M_d , one can see that another option to get a lower damping ratio (i.e. faster response) is to increase the virtual stiffness K_d . On the other hand, only using an higher virtual stiffness ($K_d \geq 1000$) with the same damping ratio ($C_d = 400$) makes the control slightly non intuitive to the operator since the system is too sensitive to small position variation. For motion with large amplitude, the controller provides quick and rough response. However, the controller is far too sensitive for fine and precise motion.

2.5 Frequency-Dependent Stiffness Controller

As described in the previous section, using a non-zero virtual mass M_d in the impedance controller generates instability because of the small interaction of the passive mini mechanism and the noise level in the mini acceleration signal $\ddot{p}(t)$. A controller using the virtual damping and stiffness term provides stable control but lacks intuitiveness, mostly for fine and precise motion.

Increasing the inertia of the mini mechanism could be an option to improve fine motion as it would filter the high-frequency motion of the operator. However this would mean that the operator will fatigue faster when using the system for longer periods.

Another means of emulating a small inertia in the controller is proposed here. It is shown in [2] that a delay in the admittance control generates an increase in perceived inertia by the user. While a too long delay makes the admittance controller impractical, a small delay in the controller could induce just enough virtual inertia to make the control more intuitive. The same principle could be applied here for an impedance controller.

It is proposed here to add a small delay on the position control term $p(t)$ by adding a virtual stiffness term K_f that is linked to a low-pass filtered version of $p(t)$. This means that the control will be more sensitive to low frequency motion, effectively reducing the system's response to high frequency motion such as trembling of the hand for fine motion. The cutoff frequency of the low-pass filter is chosen to render the control responsive in the standard human-arm bandwidth and reduce response to higher frequency motion like oscillations caused by human tremor. Hence the control shall be intuitive not only for large and imprecise motion but also for fine manipulation.

2.5.1 Controller Description

The controller presented here is based on the controller used in Chapter 1, except that the output is a force $F(t)$ instead of a desired velocity $\dot{x}_M(t)$. The force output $F(t)$ is transformed into a torque $\tau_M(t)$ using eq. 2.21 before being sent to the macro mechanism. The controller equation is shown below.

$$F(t) = C_d \dot{p}(t) + K_d p(t) + K_f p_f(t) \quad (2.41)$$

Herein, $p(t)$ represents the position of the mini mechanism along the x -axis and the term $p_f(t)$ represents a low-pass filtered version of this position $p(t)$. The term K_f is also representing a virtual stiffness. Again, eq. 2.41 can easily be converted into the same form as eq. 2.20 using the same angle approximation. This yields the following final control equation.

$$F(t) = lC_d\dot{\theta}(t) + lK_d\theta(t) + lK_f\theta_f(t) \quad (2.42)$$

The virtual stiffness terms K_d and K_f are used together because a response to high frequency motion is still desired. Only using the K_f term would completely eliminate the response to any motion above the cutoff frequency.

2.5.2 System Response to a Unit Impulse

The same theoretical stability analysis is performed for this alternative controller, using the dynamic eq. 2.16 and the controller eq. 2.42.

$$f_h(t)\frac{M+m}{m} - g(M+m)\theta(t) - Ml\ddot{\theta}(t) = lC_d\dot{\theta}(t) + lK_d\theta(t) + lK_f\theta_f(t) \quad (2.43)$$

Solving for the external force $f_h(t)$ yields

$$f_h(t) = \frac{m}{M+m} \left[C_d l \dot{\theta}(t) + K_d l \theta(t) + K_f l \theta_f(t) + (M+m)g\theta(t) + Ml\ddot{\theta}(t) \right] \quad (2.44)$$

Using the Laplace transform on the above equation gives

$$F_H(s) = \frac{m}{M+m} \left[K_d l \Theta(s) + C_d l s \Theta(s) + K_f l \Theta_f(s) + (M+m)g\Theta(s) + Ml s^2 \Theta(s) \right] \quad (2.45)$$

The low-pass filtered $\Theta_f(s)$ can easily be related to $\Theta(s)$ in the Laplace domain via the low-pass filter transfer function where ω_c represents the low-pass cutoff angular frequency.

$$\Theta_f(s) = \frac{\omega_c}{s + \omega_c} \Theta(s) \quad (2.46)$$

Substituting eq. 2.46 into eq. 2.45 then yields

$$F_H(s) = \Theta(s) \frac{m}{M+m} \left[C_d l s + K_d l + \frac{K_f l \omega_c}{s + \omega_c} + (M+m)g + Ml s^2 \right] \quad (2.47)$$

which can be written as

$$\frac{\Theta(s)}{F_H(s)} = \frac{M+m}{mMl} \frac{b_1 s + b_0}{a_3 s^3 + a_2 s^2 + a_1 s + a_0} \quad (2.48)$$

with

$$\begin{aligned}
b_0 &= \omega_c \\
b_1 &= 1 \\
a_0 &= \left(\frac{1}{M} (K_d + K_f) + \frac{g}{l} \left(1 + \frac{m}{M} \right) \right) \omega_c \\
a_1 &= \frac{1}{M} (K_d + C_d \omega_c) + \frac{g}{l} \left(1 + \frac{m}{M} \right) \\
a_2 &= \omega_c + \frac{C_d}{M} \\
a_3 &= 1
\end{aligned} \tag{2.49}$$

2.5.3 Theoretical Stability Analysis

Starting from eq. 2.48 and setting the external perturbation to $F_H(s) = 1$ yields

$$\Theta(s) = \frac{M + m}{mMl} \frac{s + b_0}{a_3 s^3 + a_2 s^2 + a_1 s + a_0} \tag{2.50}$$

This system is more complex than the standard impedance controller analyzed previously, mostly due to the low-pass filtered term $K_f \theta_f(t)$ used instead of the virtual mass term $M_d \ddot{\theta}(t)$. Indeed, the former adds a zero and a pole to the system, which previously had only two poles.

While the previous system was easily analyzed using the damping ratio ζ and angular cutoff frequency ω_0 , this system is more complex and such parameters cannot be used. Instead, the poles of the system defined from the zeros of the denominator ($a_3 s^2 + a_2 s^2 + a_1 s + a_0$) are used to predict the system response. Since the denominator is a cubic polynomial function, the roots are found using the following equations.

$$\begin{aligned}
\Delta &= 18a_3 a_2 a_1 a_0 - 4a_2^3 a_0 + a_2^2 a_1^2 - 4a_3 a_1^3 - 27a_3^2 a_0^2 \\
\Delta_0 &= a_2^2 - 3a_3 a_1 \\
\Delta_1 &= 2a_2^3 - 9a_3 a_2 a_1 + 27a_3^2 a_0 \\
C &= \sqrt[3]{\frac{\Delta_1 \pm \sqrt{-27a_3^2 \Delta}}{2}} \\
x &= -\frac{1}{3a_3} \left(a_2 + C + \frac{\Delta_0}{C} \right)
\end{aligned} \tag{2.51}$$

The cubic discriminant Δ can be used to determine the nature of the system's response. Indeed, when $\Delta > 0$, the polynomial has 3 distinct real roots, hence the system is over-damped. When the discriminant $\Delta < 0$, then the polynomial has one real root and two

complex conjugate roots, which means that the system is under-damped and will therefore oscillate around the equilibrium position. When the discriminant is equal to zero ($\Delta = 0$), then the polynomial's roots are all real and there is a multiple root. This case represents the critically damped system. Note that for stability, all roots must have a negative real part.

Similarly to the case of the standard impedance controller, the objective is to be able to define a variable gain that will be used to compute the remaining gains in order to get a critically damped system. While a critically damped system is theoretically possible, in practice an over-damped system is better suited to reduce the probability of obtaining unstable behaviours.

Critically Damped System $\{\Delta = 0, \Delta_0 = 0\}$

For a system to be critically damped, all its poles must be strictly negative real values. A positive — or null — pole makes the system unstable and complex conjugate poles make the system oscillatory. For a third-order polynomial, this means that its discriminant Δ must be greater than zero. For a critically damped system, the real roots must be identical (multiple root). This happens only when the two following conditions are met:

$$\begin{aligned}\Delta &= 0 \\ \Delta_0 &= 0\end{aligned}\tag{2.52}$$

In that case, the multiple real root is defined by the following expression

$$x = -\frac{a_2}{3a_3} = -\frac{a_2}{3}\tag{2.53}$$

The system is stable if and only if the multiple roots are a real negative value. Hence the following condition is found

$$-\frac{a_2}{3} < 0\tag{2.54}$$

or simply

$$a_2 > 0\tag{2.55}$$

which corresponds to

$$\frac{C_d}{M} + \omega_c > 0\tag{2.56}$$

or

$$C_d > -\omega_c M \quad (2.57)$$

Since both constants $\{M, \omega_c\}$ have a positive value, the final condition is

$$C_d > 0 \quad (2.58)$$

Since a condition is defined for C_d , this gain will be used as a variable to compute the remaining two gains $\{K_d, K_f\}$. A relation between K_d and C_d is found using the condition $\Delta_0 = 0$.

$$\begin{aligned} \Delta_0 &= 0 \\ a_2^2 - 3a_1 &= 0 \\ a_2^2 &= 3a_1 \\ \left[\frac{C_d}{M} + \omega_c \right]^2 &= 3 \left[\frac{1}{M} (K_d + C_d \omega_c) + \frac{g}{l} \left(1 + \frac{m}{M} \right) \right] \\ \frac{C_d^2}{M^2} + \frac{2C_d \omega_c}{M} + \omega_c^2 &= \frac{3K_d}{M} + \frac{3C_d \omega_c}{M} + \frac{3g}{l} \left(1 + \frac{m}{M} \right) \end{aligned} \quad (2.59)$$

Solving the above equation for K_d yields

$$K_d = \frac{1}{3} \left[\frac{C_d^2}{M} - C_d \omega_c + \omega_c^2 M - \frac{3g}{l} (M + m) \right] \quad (2.60)$$

An expression to obtain the gain K_f from C_d is found using the condition $\Delta = 0$.

$$K_f = \frac{1}{27} \left[\frac{-8\omega_c^3 M^3 + C_d^3 + 12C_d \omega_c^2 M^2 - 6C_d^2 \omega_c M}{M^2 \omega_c} \right] \quad (2.61)$$

Over-damped System $\{\Delta = 0, \Delta_0 \neq 0\}$

While in theory a critically damped system provides the best response in terms of stability and responsiveness, in practice an over-damped system provides a more stable system. This is due to the fact that a slight error in any of the parameters of the model may make the system go from critically damped to either over-damped or under-damped. For this reason, an over-damped system is usually preferable.

For the current system to be over-damped, all its poles must have real negative values, and more than one root is needed. This means that the cubic function discriminant must again

meet the condition ($\Delta \geq 0$). For the sake of simplicity, we will use the condition $\Delta = 0$. In order to have more than one pole — difference with the critically damped system — the condition on Δ_0 becomes $\Delta_0 \neq 0$.

$$\begin{aligned}\Delta_0 &\neq 0 \\ \Delta_0 &= a_2^2 - 3a_1 \neq 0 \\ a_2^2 &\neq 3a_1\end{aligned}\tag{2.62}$$

Using this first condition, the following expression for K_d is obtained

$$K_d \neq \frac{1}{3} \left[\frac{C_d^2}{M} - C_d \omega_c + \omega_c^2 M - \frac{3g}{l}(M + m) \right]\tag{2.63}$$

Now, looking at the poles x_1 and x_2 of the system, we have the following conditions for a stable system.

$$\begin{aligned}x_1 &= \frac{9a_0 - a_2 a_1}{2\Delta_0} < 0 \\ x_2 &= \frac{4a_2 a_1 - 9a_0 - a_2^3}{\Delta_0} < 0\end{aligned}\tag{2.64}$$

For the critically damped system, the evaluation of the single root was simple as it provides the stable limits of C_d . For the over-damped case, the problem is ill-posed since we have two inequalities with three variables $\{K_d, C_d, K_f\}$.

Expressions for K_d and K_f as functions of C_d — such as the expression found for the critically damped system — cannot be obtained here. However, the provided conditions can be used to verify that the gains $\{K_d, C_d, K_f\}$ are in the stable region.

The complete expressions from eq. 2.64 are presented below for reference.

$$\begin{aligned}x_1 &= -\frac{1}{2} \left[\frac{-8w_c M l K_d - 9w_c M l K_f - 8w_c M^2 g - 8w_c M g m + C_d l K_d}{l C_d^2 l C_d w_c M + l w_c^2 M^2 - 3M l K_d - 3g M^2 - 3g M m} \right] + \\ &\frac{1}{2} \left[\frac{C_d^2 l w_c + C_d g M + C_d g m + w_c^2 M l C_d}{l C_d^2 l C_d w_c M + l w_c^2 M^2 - 3M l K_d - 3g M^2 - 3g M m} \right] < 0\end{aligned}\tag{2.65}$$

$$x_2 = - \left[\frac{-4MC_d l K_d - MC_d^2 l \omega_c - 4C_d g M^2 - 4MC_d g m + 5\omega_c M^2 l K_d}{M(lC_d^2 - lC_d \omega_c M + l\omega_c^2 M^2 - 3MlK_d - 3gM^2 - 3gMm)} \right] + \left[\frac{-\omega_c^2 M^2 l C_d + 5\omega_c M^3 g m + 9\omega_c M^2 l K_f + lC_d^3 + l\omega_c^3 M^3}{M(lC_d^2 - lC_d \omega_c M + l\omega_c^2 M^2 - 3MlK_d - 3gM^2 - 3gMm)} \right] < 0 \quad (2.66)$$

Methodology

Even though no analytical solution was obtained to correctly set the gains to get an over-damped system, a methodology is proposed here that uses the relations obtained for the critically damped system. It is hypothesized here that an over-damped behaviour can be reached from a critically damped system by slightly modifying its gains.

The same conditions — see below — are used to ensure stability.

$$\begin{aligned} \Delta &= 0 \\ \Delta_0 &\neq 0 \\ x_1 &< 0 \\ x_2 &< 0 \end{aligned} \quad (2.67)$$

The first step is to set a strictly positive (non-zero) virtual damping value C_d .

$$C_d > 0 \quad (2.68)$$

Then we get an expression for K_d using eq. 2.60, but the virtual damping C_d is instead replaced with γC_d , where γ is a real coefficient.

$$K_d = \frac{1}{3} \left[\frac{(\gamma C_d)^2}{M} - \gamma C_d \omega_c + \omega_c^2 M - \frac{3g}{l} (M + m) \right] \quad (2.69)$$

The condition $\Delta = 0$ is then used to get an expression for the remaining term K_f .

$$\begin{aligned} K_f &= \left[\frac{-8\omega_c^3 M^3 + 6\omega_c^2 M^2 C_d + 6\omega_c^2 M^2 \gamma C_d - 3\omega_c M C_d^2 \gamma + 3\omega_c M C_d^2 - 6\omega_c M \gamma^2 C_d^2}{27M^2 \omega_c} \right] \\ &+ \left[\frac{-2C_d^3 + 3\gamma^2 C_d^3 + 2\sqrt{-C_d^3(\gamma - 1)^3(C_d \gamma + C_d - \omega_c M)^3}}{27M^2 \omega_c} \right] \end{aligned} \quad (2.70)$$

If $\gamma = 1$, then eq. 2.69 and eq. 2.70 become respectively eq. 2.60 and eq. 2.61. The system would then be critically damped.

Now only the coefficient γ needs to be defined in order to get an over-damped system. We therefore need to define a domain within which γ provides real negative roots. The root eq. 2.64 is shown below with the factor γ .

$$x_1 = -\frac{1}{3} \left[\frac{\omega_c M C_d^2 \gamma^2 - \omega_c^2 M^2 \gamma C_d + \omega_c^2 M^2 C_d - \omega_c M C_d^2 \gamma}{M C_d (-C_d + \omega_c M + C_d \gamma^2 - \gamma \omega_c M)} \right] - \frac{1}{3} \left[\frac{-C_d^3 + \gamma^2 C_d^3 + \sqrt{-C_d^3 (\gamma - 1)^3 (C_d \gamma + C_d - \omega_c M)^3}}{M C_d (-C_d + \omega_c M + C_d \gamma^2 - \gamma \omega_c M)} \right] < 0 \quad (2.71)$$

$$x_2 = -\frac{1}{3} \left[\frac{\gamma^2 C_d^3 - \omega_c M C_d^2 \gamma + \omega_c^2 M^2 C_d + \omega_c M C_d^2 \gamma^2 + \omega_c^2 M^2 \gamma C_d}{M C_d (-C_d + \omega_c M + C_d \gamma^2 - \gamma \omega_c M)} \right] - \frac{1}{3} \left[\frac{-C_d^3 - 2\sqrt{-C_d^3 (\gamma - 1)^3 (C_d \gamma + C_d - \omega_c M)^3}}{M C_d (-C_d + \omega_c M + C_d \gamma^2 - \gamma \omega_c M)} \right] < 0 \quad (2.72)$$

Starting with the over-damped system condition, i.e. that the roots be real (not complex conjugates) simplifies the previous conditions to

$$\sqrt{-C_d^3 (\gamma - 1)^3 (C_d \gamma + C_d - \omega_c M)^3} \rightarrow \text{Real} \quad (2.73)$$

Hence

$$-C_d^3 (\gamma - 1)^3 (C_d \gamma + C_d - \omega_c M)^3 > 0 \quad (2.74)$$

By definition, $C_d^3 > 0$, hence the previous inequality is true if and only if

$$\text{sign}[(\gamma - 1)^3] \neq \text{sign}[(C_d \gamma + C_d - \omega_c M)^3] \quad (2.75)$$

From the left-hand side of 2.75

$$\begin{aligned} (\gamma - 1)^3 &< 0 \text{ when } \gamma < 1 \\ (\gamma - 1)^3 &> 0 \text{ when } \gamma > 1 \end{aligned} \quad (2.76)$$

and from the right-hand side

$$\begin{aligned}
(C_d\gamma + C_d - \omega_c M)^3 &< 0 \text{ when } \gamma < \frac{\omega_c M}{C_d} - 1 \\
(C_d\gamma + C_d - \omega_c M)^3 &> 0 \text{ when } \gamma > \frac{\omega_c M}{C_d} - 1
\end{aligned} \tag{2.77}$$

Hence, the roots $\{x_1, x_2\}$ and the term K_f are real for the following domain of γ :

$$\begin{aligned}
\left[\frac{\omega_c M}{C_d} - 1 < \gamma < 1 \right] &\text{ if } \left(\frac{\omega_c M}{C_d} < 2 \right) \\
\left[1 < \gamma < \frac{\omega_c M}{C_d} - 1 \right] &\text{ if } \left(\frac{\omega_c M}{C_d} > 2 \right)
\end{aligned} \tag{2.78}$$

Equation. 2.78 provides a bounded domain for which the roots are real and where the solution might be an over-damped system. It is proposed to start from $\gamma = 1$ and either slowly increase (or decrease) its value.

The proposed methodology is summarized below. While it does not give a proven γ domain for which the system is over-damped, it proposes a bounded trial-and-error method with a clear starting point ($\gamma = 1$) which comes from physical insight (i.e. critically damped system). The methodology can be stated as follow:

1. Select a strictly positive real virtual damping value $C_d > 0$.
2. Compute the boundary for γ using eq. 2.78.
3. Starting from $\gamma = 1$, either increase or decrease γ depending on its previously computed domain. Compute the roots $\{x_1, x_2\}$ using eq. 2.71 and eq. 2.72. Verify that they are negative.
4. Compute the gains K_p and K_f using eq. 2.69 and eq. 2.70 respectively.
5. Compute the system response $\theta(t)$ using eq. 2.48. If the response is satisfactory (sufficiently over damped), then select the computed gains $\{C_d, K_d, K_f\}$.

Example

The current example uses the experimental parameters given in Section 2.2. The virtual damping is selected to be $C_d = 400$ kg/s and the frequency $\omega_c = 100$ rad/s. The boundaries of γ are initially computed using eq. 2.78.

$$\frac{\omega_c M}{C_d} = 0.35 \tag{2.79}$$

$$-0.65 < \gamma < 1 \quad (2.80)$$

Figure 2.11 shows the simulated response for several values of γ in this range. The relation between γ and the type of response is observed. First, it is noted that the responses obtained when using the boundary values of the coefficient (in this case $\gamma = -0.65$ and $\gamma = 1$) are identical, i.e. a critically damped response.

The response obtained at the centre of the coefficient domain ($\gamma = 0.175$) is the most damped. As the value of the coefficient gets closer to one of the boundaries, the response obtained gets closer to the critically damped response. The system response was also computed for $\gamma = 1.5$, which is outside the damped boundary. For this value of γ , the response is indeed underdamped.

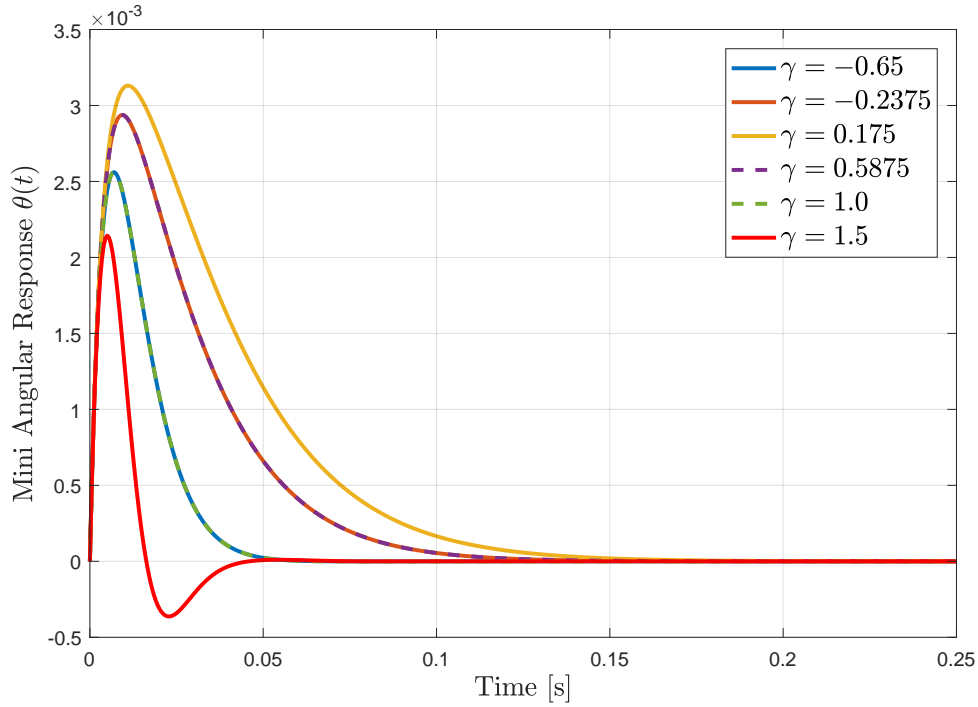


Figure 2.11 – Simulated response of the system for different values of γ using the proposed methodology for an over-damped system gain sets.

2.5.4 Experimental Stability Analysis

As already explained in Section 2.4, the discrepancies between the theoretical model and the experimental setup forces us to use an empirical methodology to set stable gains. When the virtual stiffness K_f is equal to zero, the system reverts back to the standard impedance controller with a zero virtual mass ($M_d = 0$). Therefore, the same value of virtual stiffness ($K_d = 1000$) and virtual damping ($C_d = 400$) previously found can be used safely again, only the virtual stiffness K_f needs to be set. As stated before, increasing the response in position

— by adding the term K_f in the controller — should reduce the original damping ratio of the standard impedance.

The same gain values used for the standard impedance controller were tried here for the new frequency-dependent stiffness gain K_f . The results obtained are shown in figure 2.12. Compared with the virtual mass M_d term of the standard impedance controller, the new virtual stiffness term K_d provides a stable response to external perturbations.

The system responses retain the same form for any value of K_f that was tested. Increasing the new virtual stiffness K_f provides a slightly faster response to perturbation. From the curve below, the best response could subjectively be selected to be $K_f = 500$ since it provides a quicker response without increasing the oscillation significantly. Using the combination of virtual stiffness $\{K_d = 1000, K_f = 500\}$ means that manipulation with a motion frequency below ω_c should have a 50% higher response than for higher frequency motion.

While this is not apparent on the graphs, the system response feels more intuitive with the new virtual stiffness term K_f . The system is more responsive to standard motion amplitude and frequency while effectively reducing the high frequency motion such as hand trembling.

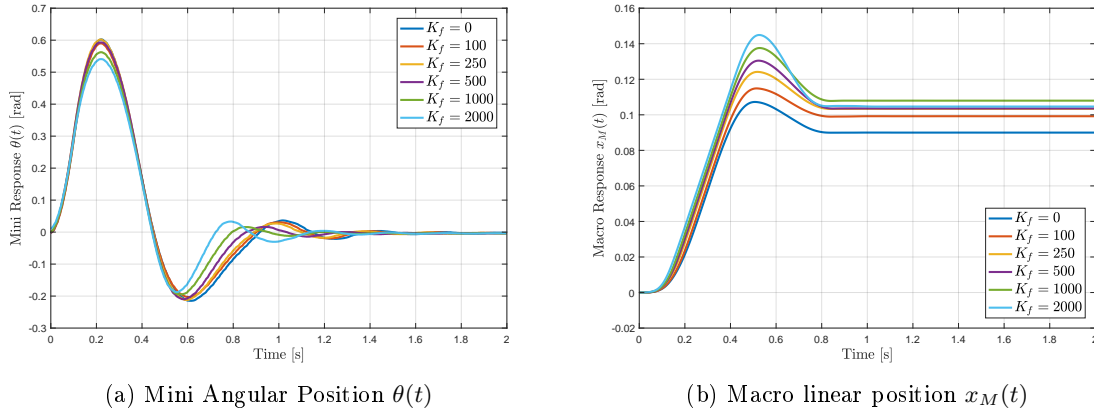


Figure 2.12 – Experimental response for multiple values of frequency-dependent virtual stiffness K_f . $\{K_d = 1000, C_d = 400\}$

2.5.5 Discussion

An alternative impedance controller was presented here in order to solve the instability problem of the standard impedance control when using a non-zero virtual mass M_d . The new controller uses an additional stiffness term that is linked to a filtered (low-pass) position signal $p(t)$.

The proposed alternative controller provides a quick and stable response, both for large amplitude and precise motions. Experimental results showed that stability is not an issue, even for high values of the stiffness.

The theoretical analysis was more complex than for the standard impedance controller since the transfer function of the system has an additional pole. In other words, the system is no more a classical second-order low-pass filter and hence cannot be analyzed solely using a damping ratio ζ and a cutoff frequency ω_0 .

A methodology was however provided in order to safely go from a critically damped system to an over-damped system, using a mathematical analysis of the transfer function poles.

It could be argued that only the filtered virtual stiffness K_f could be used (with the virtual damping C_d). However the original virtual stiffness K_d gain provides a baseline response in position for both low and high-frequency motion. This baseline gain yields an intuitive control.

2.6 Conclusion

A simplified version of the passive macro-mini architecture was presented in this chapter. This simplified mechanism consists of a pendulum of mass m attached to a passive angular joint with an encoder and a motor is attached to a cart of mass M (including the motor mass) that is moved linearly along a rail. The motor mounted on the cart is not actuated. The linear movement is provided by a ball screw system with a DC motor.

The system dynamics were described in terms of the mini angular motion $\theta(t)$ and the force generated by the macro mechanism $F(t)$. Then, two different impedance controllers were presented. These controllers compute the desired force $F(t)$ to be applied to the macro mechanism as a function of the mini mechanism angular motion $\theta(t)$. Both controllers were theoretically and experimentally analyzed.

The first controller consists of the standard impedance control firstly described in [1], consisting of a virtual mass M_d , damping C_d and stiffness K_d . The stability of the system in response to a unit-impulse force $f_h(t)$ was presented. Relations between the different impedance terms were obtained in order to get either an under-damped, over-damped or critically damped system. Empirical data were acquired to compare the response with simulations. Comparison between the theoretical and experimental responses showed discrepancies between the experimental setup and the model. These differences can mostly be explained by the friction at

the mini mechanism joint that was not modeled, the small angle approximation used and the numerical differentiation used to obtain the velocity and acceleration signal from the measured position. Stable responses were obtained when using the terms C_d and K_d , however the use of a non-zero virtual mass M_d causes the system to become unstable.

In order to address the stability issue related to the virtual mass M_d of the standard impedance controller, this term was replaced by another virtual stiffness term K_f which is linked to a low-pass version of the position of the mini mechanism $\theta_f(t)$. It was found in the literature that a small delay in an admittance controller is felt by the operator as a small inertia. The same principle was used here for an impedance controller. Using the low-pass term $K_f\theta_f(t)$ generates a small delay in the stiffness term that is felt by the user as a simulated inertia. The theoretical stability of such a controller was presented. An analytical expression to obtain a critically damped system was found and a methodology was proposed to safely go from a critically damped system to an over-damped system. Experimental results demonstrated that the replacement of the term $M_d\ddot{\theta}(t)$ by $K_f\theta_f(t)$ solves the instability problem and helps to reduce high-frequency motion such as hand tremor. This additional virtual inertia helps for fine and precise motion that is affected by the human tremor.

2.7 Bibliography

- [1] Neville Hogan. Impedance control: An approach to manipulation. In *1984 American control conference*, pages 304–313. IEEE, 1984.
- [2] Irene A Kuling, Jeroen BJ Smeets, Piet Lammertse, Bram Onneweer, and Winfred Mugge. Delays in admittance-controlled haptic devices make simulated masses feel heavier. *PloS one*, 10(9):e0138023, 2015.
- [3] Pascal D Labrecque, Jacques-Michel Haché, Muhammad Abdallah, and Clément Gosselin. Low-impedance physical human-robot interaction using an active–passive dynamics decoupling. *IEEE Robotics and Automation Letters*, 1(2):938–945, 2016.
- [4] Pascal D Labrecque, Thierry Laliberté, Simon Foucault, Muhammad E Abdallah, and Clément Gosselin. Uman: A low-impedance manipulator for human–robot cooperation based on underactuated redundancy. *IEEE/ASME Transactions on Mechatronics*, 22(3):1401–1411, 2017.

Chapter 3

Active Macro-Mini Architecture and Control Strategies

This chapter aims at presenting how an active mini mechanism can be used to generate haptic feedback, to reduce payload oscillations during planned motion and to detect environment collision for safe human-robot interactions. Several types of virtual environment interactions are presented including wall and moveable object collision and addition of a virtual mass at the mini mechanism end-effector to modify the impedance felt by the user. The limits of such haptic feedback rendering are also discussed in depth. During planned trajectory motion of the macro mechanism, the mini active joint is used to reduce payload oscillation by compensating for the gravitational and macro mechanism accelerations. The system dynamics presented in Chapter 2 is again used here for both oscillation reduction and the collision detection, which is almost a prerequisite for physical human-robot interaction.

3.1 Introduction

The passive macro-mini architecture presented in Chapters 1 and 2 provides a very efficient interface for physical-human robot interactions (pHRI). Indeed the low-impedance of the mini mechanism allows intuitive and effortless manipulations of a high-impedance macro mechanism such as a three-degree-of-freedom gantry robot. Such intuitive control is difficult to obtain with more common admittance controllers where the robot motion is computed from force sensor measurements.

Nonetheless, the previously described passive macro-mini architecture — where only the mini mechanism is passive — still has some limitations. Firstly, the only means to provide haptic feedback to the user is by controlling the macro mechanism in order for the mini mechanism to hit its workspace limit. This greatly limits the type of haptic feedback that can be rendered and also affects the life expectancy of the mechanism.

Another problem with the passive mini joint arises with the motion planning of the macro mechanism. For safety reasons, the defined trajectories must take into consideration the passive link as the payload may overshoot and oscillate during the motion. This problem is usually called the overhead crane problem and is extensively covered in the literature [22, 25, 30].

One advantage of the admittance over impedance control is the ability to easily detect environment interaction through the force sensor measurement. Such collision detection is of paramount importance for collaborative robots and mechanisms. Although more complex, there are still robust methods to detect such collision from the mini mechanism encoder system and a proper dynamic model [14].

One possible approach to resolve the above issues and disadvantages is to add a back-drivable motor to each of the joints of the mini mechanism. Back-drivability is of capital importance to maintain a low impedance at the mini mechanism for intuitive and effortless pHRI.

This chapter aims at describing how to add and control the active mini mechanism in order to provide haptic feedback, reduce payload oscillation during planned trajectory motion and detect environment collision using the mini mechanism encoding system. The chapter is structured as follows.

Section 3.2 describes three different virtual object interactions using the active macro-mini architecture. The first virtual object consists of a simple, unmovable wall interaction. The second interaction consists of an inelastic collision with a virtual mass. The last haptic feedback described and demonstrated is the addition of a virtual mass attached to the mini end-effector. For the last interaction the stability of the whole system is once more proven with the same method as in Section 2. All haptic feedback interactions were implemented and experimentally evaluated.

Section 3.3 presents a simple planned trajectory motion for the macro mechanism to move from point A to point B. The effect of such motion on the passive mechanism joint is investigated. Then, the back-drivable motor added to the mini joint is used in accordance to the dynamic model to reduce the oscillation produced by the macro acceleration $\ddot{x}_M(t)$. The dynamic model developed in Chapter 2 is again used to compute the required mini mechanism torque $\tau_c(t)$.

Section 3.4 outlines a method to detect environment collision during planned trajectory motion described in Section 3.3. The described method is implemented and tested on the simplified macro-mini of Chapter 2. A force sensor was added to the mini end-effector to measure and compare collision detection with a more conventional approach used in admittance control.

The chapter is then closed with a brief conclusion in Section 3.5, providing a quick summary of what was accomplished with the active mini mechanism and insight on future work.

3.2 Impedance Control with Haptic Feedback

The addition of a backdrivable motor at the mini mechanism joint provides the possibility to render haptic feedback to the user while controlling the macro mechanism with the controller described in Chapter 2. This new possibility can be used to simulate virtual environment constraints such as wall or object like tables, chairs or even a car structure in a production cell [7, 12, 15, 18, 20, 21, 23, 27, 31].

Such haptic feedback could also be generated using the passive mini mechanism, but at the expense of controller complexity and compromise on feedback authenticity. Indeed, feedback force would need to be generated with the combination of macro acceleration and mini mechanism physical limits in order for the mini mechanism to hit the mechanical stop at its workspace boundary and hence generate an force feedback. This is a significant limitation of the passive architecture.

Adding motors to the mini mechanism allows the generation of more elaborate feedback force without adding much complexity to the existing control. In fact, the macro mechanism controller remains unchanged, attempting to reposition the mini mechanism to its equilibrium position. The mini mechanism controller is solely used to generate the force feedback, using the macro and mini mechanism's measured location and motion and the virtual world constraint to generate the force.

As simple as it seems, there is still a limitation caused by the macro-mini architecture used. Since the macro-mini mechanism has a decoupled Cartesian architecture, only pure feedback forces can be generated. The following hypothesis is therefore stated: the mini mechanism's tip, with which the virtual world interacts, is a frictionless spherical tip. This hypothesis eliminates the need to compute torque feedback.

In this section, three different objects interaction are simulated and implemented. The simplest interaction consists of constraints caused by virtual walls since there is not virtual object motion dynamic to compute (Section 3.2.1). Section 3.2.2 presents the interaction with moveable objects. In this case, the virtual object dynamics must be computed in addition to the interaction force. Elastic and inelastic collisions are considered and investigated experimentally. The third interaction consists of adding a virtual mass to the mini mechanism end-effector (Section 3.2.3). Such virtual interaction can be used to simulate a variable payload or to adjust the impedance felt by the operator during the macro mechanism manipulation.

One of the early works on haptic feedback and interface led to the PHANToM mechanism [18]. The authors stated three criteria for effective haptic interfaces. First, the free space where no virtual interaction occurs must truly feel free. Second, the solid virtual objects must feel stiff. And finally, the virtual constraints must not be easily saturated. While the first two criteria are quite simple to understand the last criterion means that the haptic interface (i.e. the mini mechanism) must be able to generate high enough forces to render the various virtual objects. Since there is a limit on the possible force to be generated by the mini joint, there is therefore a limit on the virtual object mass or stiffness that can be rendered intuitively. Such constraints will be explored in the following subsections.

Reference [18] also proposed to simulate virtual walls using one-sided Hooke’s laws. The idea is that since the control is always working in discrete-time, the collision detection method can simply verify and measure the penetration depth of the end-effector through the virtual wall and apply a force — opposite to the penetration direction — using a very high virtual stiffness value K_v [23].

Furthermore, in order to simplify the control and simulation, the end-effector tip is considered to be spherical and frictionless [23]. Hence, no torque is generated at the tip of the mini, only Cartesian force.

It is stated in [19] that any physical system could be simulated using only a combination of ideal textbook objects such as springs, mass and damper. Modeling moveable objects is possible using a virtual mass and a viscous friction coefficient [23]. The virtual mass M_v is related to the tip acceleration while the viscous friction is related the the velocity component. This term can be see as a virtual damping C_v coefficient.

Specific stereotypical hand motions are associated with certain features of objects [15]. An example is the lateral motion of the hands (or finger) which is associated with the texture exploration. In our study, the virtual object will be modeled using a null surface roughness ($R_a = 0$). Note however that texture could be modeled using a more complex profile of the object surface, such as adding white noise to each surface. Surface roughness can only be felt with a multiple DOF manipulator since the roughness is rendered using a force normal to the mini mechanism motion direction.

An important relation between the parameters of the haptic device and what it can render as virtual object is described in [23]. The following equations show the relation between the device's mechanical damping b , the level of digital damping commanded to the device B , the virtual stiffness K to render and the servo period T controlling the device.

$$b > \frac{KT}{2} + B \quad (3.1)$$

This relation means three things. First, with the damping $\{b, B\}$ fixed, the maximum achievable stiffness is inversely proportional to the sampling period T . Second, with a zero virtual stiffness $\{K = 0\}$, the maximum virtual damping B is independent from the sampling rate ($b > B$). And finally, with the sampling period T and the mechanical damping B fixed, higher virtual stiffness K can only be achieved at the expense of reducing the virtual damping B .

3.2.1 Interaction with Virtual Wall

The term virtual wall will be used here for any object that should be rendered as static, such as wall or very heavy object. In this case, the kinematic constraints associated with the virtual object are quite simple, namely

$$\begin{aligned} x_v(t) &= x_v \\ \dot{x}_v(t) &= 0 \\ \ddot{x}_v(t) &= 0 \end{aligned} \quad (3.2)$$

Such interactions are widely described in the literature as they are the simplest ones. Indeed, there is no virtual dynamics to compute, only a reaction force to be generated by the haptic interface. In the current case, the reaction force f_R is generated by the mini mechanism. Note that the force f_R must be converted into a torque τ_c using the mini end-effector link length l . The force f_R depends on the virtual object stiffness K_v and the penetration depth herein referred to as $\Delta x = (x_v - x_m)$.

$$f_R = K_v \Delta x = K_v (x_v - x_m) \quad (3.3)$$

While the force computed depends strictly on the penetration depth and hence the mini position x_m , it is still indirectly dependent on the mini end-effector velocity and the computation sample period T . Indeed, the larger the mini velocity, the greater the penetration depth Δx will be.

While a standard stiffness K usually works in both compression and extension, the virtual stiffness used here is only in compression. Hence when the mini end-effector is not within the

virtual wall, the reaction force is null. Figure 3.1 illustrates the reaction force and the system dynamics.

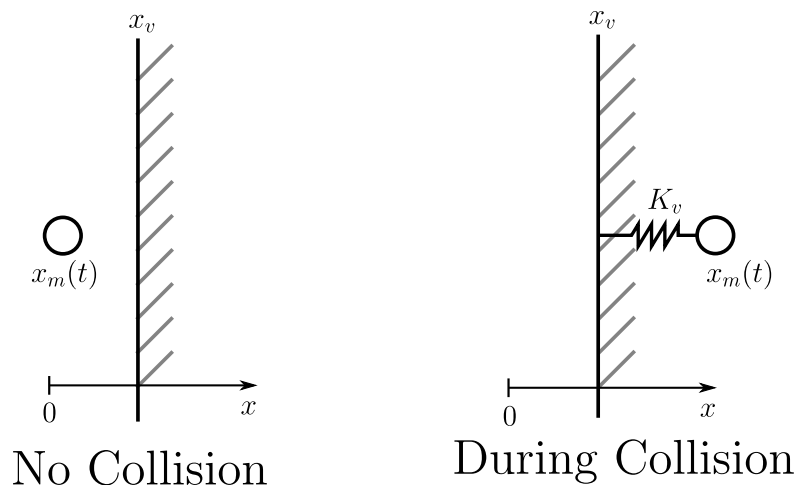


Figure 3.1 – Illustration of the dynamics involved in the interactions between the mini end-effector and the virtual wall.

In order to render wall — or any static object for that matter — the virtual stiffness K_v must be very high [23] and the mini mechanism must be able to render high forces, which are directly proportional to K_v , otherwise the control will saturate [18]. The present mechanism design can only generate a torque τ_c of approximately 1Nm. This means that with the mini effector length ($l = 0.19\text{m}$) the maximum force at the end-effector would be approximately 5N. This is clearly not enough to render stiff wall at standard human arm velocity.

Using the controller described in Section 2.5 a virtual wall was simulated at a specific position. However, as stated previously the present mechanism does not allow for intuitive and realistic wall rendering. Hence the wall feels soft instead of stiff and in some cases, whence the macro-mini motion is fast enough, the whole system could pass through the wall since the torque τ_c saturates quite easily.

3.2.2 Interaction with Moveable Virtual Object

Virtually moveable objects such as balls, chairs and tables are more complex to render compare with unmovable objects defined previously. In the case of a moveable object, the reaction force f_R acting on the mini end-effector must be computed, together with the dynamics of the virtual object $\{x_v(t), \dot{x}_v(t), \ddot{x}_v(t)\}$.

In order to model such an object, a virtual damping C_v and a virtual mass M_v are used instead of the virtual stiffness K_v . This means that the reaction force f_R now depends on the mini and virtual object velocities $\{\dot{x}(t), \dot{x}_v(t)\}$ and accelerations $\{\ddot{x}(t), \ddot{x}_v(t)\}$. Figure 3.2 illustrates the interaction between the mini end-effector and a virtual object described with a virtual mass and damper. Note that a virtual stiffness could have been added to render object deformation such as squishing a ball. However such interactions are not addressed here.

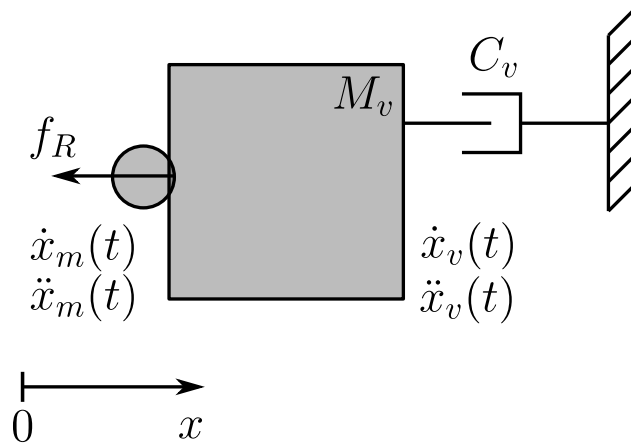


Figure 3.2 – Illustration of the dynamics involved in the interactions between the mini end-effector and a moveable virtual object described by a virtual mass M_v and damping C_v .

In the following subsections, the collision between the mini mechanism and the virtual object is explored. The coefficient of restitution γ is used to render and compare different nature and material of virtual object. First, the elastic collision mechanics is described and used to compute the reaction force f_R . Then, the command computed for the mini mechanism is presented. The virtual object's dynamics after the collision are also explored and the discrete-time algorithm — both for the mini command and the virtual object motion — is presented. Experimental results with various virtual masses M_v , damping C_v and restitution coefficients γ are shown and analyzed. Note that for simplicity, no external force f_h is considered in the dynamic model in the following subsections.

Reaction Force f_R during Collision

The collision between the mini mechanism and a virtual object is illustrated in figure 3.2, where the mini end-effector dynamics is represented with $\dot{x}(t)$ and $\ddot{x}(t)$. The reaction force f_R

is directly related to the change of momentum Δp caused by the collision.

The change in momentum is defined by

$$\Delta p = M\Delta V = F\Delta t \quad (3.4)$$

where ΔV corresponds to the change in velocity of the mass M and F corresponds to a force applied during a time Δt in order to produce such a change momentum. This simple equation links the change in velocity during the collision and the reaction force generated.

Knowing the initial mini m and virtual mass M_v velocities — respectively $\dot{x}_{m,1}$ and $\dot{x}_{v,1}$ — we can compute the velocities after the collision — respectively $\dot{x}_{m,2}$ and $\dot{x}_{v,2}$ — using the following equations.

$$\begin{aligned} \dot{x}_{m,2} &= \left(\frac{1}{m + M_v} \right) \left[m\dot{x}_{m,1} + M_v\dot{x}_{v,1} + \gamma M_v(\dot{x}_{v,1} - \dot{x}_{m,1}) \right] \\ \dot{x}_{v,2} &= \left(\frac{1}{m + M_v} \right) \left[m\dot{x}_{m,1} + M_v\dot{x}_{v,1} + \gamma M_v(\dot{x}_{m,1} - \dot{x}_{v,1}) \right] \end{aligned} \quad (3.5)$$

The coefficient of restitution γ is comprised in the domain $[0, 1]$. A coefficient of restitution $\gamma = 1$ corresponds to a perfect elastic collision, where no energy is lost during collision. A coefficient of restitution $\gamma = 0$ corresponds to a perfectly inelastic collision where both objects (m, M_v) have the same velocity after collision ($\dot{x}_{m,2} = \dot{x}_{v,2}$).

Therefore the reaction (or collision) force f_R is computed using the following relation where δt represents collision duration. Note that an equivalent — but of opposite direction — force is applied to the virtual object.

$$f_R = \frac{m(\dot{x}_{m,2} - \dot{x}_{m,1})}{\delta t} \quad (3.6)$$

Mini-Mechanism Command $\tau_c(t)$

In discrete time control, the force computed using eq. 3.6 can be significantly higher than the maximum force F_{max} (or maximum torque τ_{max}) that the mini mechanism can generate due to the very small control time step δt and very high change in velocity ($\dot{x}_{m,2} - \dot{x}_{m,1}$). In this case, the mini mechanism is simply used at its full capacity during a number of time steps N until the change in momentum Δp is completed. The time step δt corresponds to the discrete time step of the controller, or in other words the period between two measurements of the mini position x_m . One has then

$$\begin{aligned}
f_R &= \frac{m(\dot{x}_{m,2} - \dot{x}_{m,1})}{\delta t} \\
\tau_R &= \frac{f_R}{l} \\
N &= \tau_R \setminus \tau_{max}
\end{aligned} \tag{3.7}$$

where the operator \setminus represents the integer division.

Therefore the command sent to the mini corresponds to (τ_{max}) during $N\delta t$ and then to $(\tau - N\tau_{max})$ during a single time-step δt in order to complete the change in momentum Δp , namely

$$\tau_m = \begin{cases} \tau_{max} & \text{for } N\delta t \\ \tau - N\tau_{max} & \text{for } \delta t \end{cases} \tag{3.8}$$

This method allows us to simulate larger forces without significantly affecting the haptic feedback realism. Of course, there is still a limit on the number of time steps N that can be used before affecting the realism of the collision. This limit is not described mathematically as it is a matter of user perception.

Virtual Object Dynamics $\{x_v(t), \dot{x}_v(t), \ddot{x}_v(t)\}$

For the virtual object, the total change in momentum can be applied during a single time-step δt since there is no equivalent physical limitation in the virtual worlds. Since the virtual object is constructed with a virtual mass M_v and damper C_v , its dynamics is quite simple.

The following algorithm shows how the virtual object dynamics $(x_v, \dot{x}_v, \ddot{x}_v)$ is updated, how the collision is detected and how the reaction/collision force f_R is computed. The algorithm also shows the update order in discrete time where $t = k$ represents the current time-step while $t = (k - 1)$ represents the previous time step.

1. Get mini-mechanism measurement $\{x_m(k), \dot{x}_m(k), \ddot{x}_m(k)\}$. Note that the velocity and acceleration are numerically differentiated from the measured position $x_m(k)$, a low-pass filter is therefore applied prior to each differentiation.
2. Compute the current virtual object dynamics $\{x_v(k), \dot{x}_v(k), \ddot{x}_v(k)\}$ using the following expressions, where $F(k - 1)$ is the force applied on the virtual object at the previous time-step.

$$\begin{aligned}
\ddot{x}_v(k) &= \frac{F(k - 1) - \dot{x}_v(k - 1)C_v}{M_v} \\
\dot{x}_v(k) &= \dot{x}_v(k - 1) + \ddot{x}_v(k - 1)\delta t \\
x_v(k) &= x_v(k - 1) + \dot{x}_v(k - 1)\delta t + \ddot{x}_v(k - 1)\frac{\delta t^2}{2}
\end{aligned} \tag{3.9}$$

3. Detect collision using the mini position $x_m(k)$ and the virtual object limits position $(x_v(k-1) \pm L/2)$, where L represents the virtual object length (object boundaries).
4. If a collision occurs, compute the velocity change using the following equation (taken from eq. 3.5).

$$\dot{x}_v(k+1) = \left(\frac{1}{m + M_v} \right) \left[m\dot{x}_m(k) + M_v\dot{x}_v(k) + \gamma M_v(\dot{x}_m(k) - \dot{x}_v(k)) \right] \quad (3.10)$$

5. Compute the collision force $F(k)$ that will be applied at the next time-step to the virtual object.

$$F(k) = \frac{M_v(\dot{x}_v(k+1) - \dot{x}_v(k))}{\Delta t} \quad (3.11)$$

6. Compute the reaction force that needs to be applied to the mini-mechanism.

$$f_R(k) = -F(k) \quad (3.12)$$

It is interesting to note the virtual object behaviour in the absence of external force $F(k-1) = 0$ (see eq. 3.9). In this case the new acceleration $\ddot{x}_v(k)$ becomes

$$\ddot{x}_v(k) = -\frac{C_v}{M_v}\dot{x}_v(k-1) \quad (3.13)$$

meaning that the virtual object will decelerate until it reaches the state of rest. The deceleration rate is given by the ratio $\frac{C_v}{M_v}$. While the virtual damper was originally added to mimic friction, it is also used in order to stabilize the virtual object. Without the damper, the virtual object would remain in motion at velocity \dot{x}_v until another collision acts upon it.

Experimental Results

Experimental data were gathered using the same setup used in Chapter 2, except that the macro mechanism is passive ($\tau_M(t) = 0$). The mini mechanism is initially held in place at a specific angle ($\theta(t=0) = -\pi/4$, $x_m(t=0) = -0.13$ m) using a simple PI controller and then released in order to hit a virtual object at an initial position ($x_v(t=0) = 0.075$ m). The dashed red line in the mini position $x_m(t)$ graph of Figs. 3.3, 3.4 and 3.5 represents the initial position of the mini mechanism prior to the collision time. The algorithm previously described is then used to compute the collision force and update the virtual object dynamics and the torque sent to the mini-mechanism.

Three experiments were conducted in order to demonstrate the effect of the coefficient of restitution γ , the virtual mass M_v and the virtual damping C_v on the collision dynamics. For the first experiment, the virtual damping and mass are fixed and the coefficient of restitution is varied.

$$\begin{aligned} M_v &= 15 \text{ kg} \\ C_v &= 3 \text{ kg/s} \end{aligned} \rightarrow \gamma = \{0 \ 0.2 \ 0.4 \ 0.6 \ 0.8 \ 1.0\} \quad (3.14)$$

Figure 3.3 shows the mini mechanism and virtual object motion reaction to the collisions for the aforementioned combinations of the parameters. For the virtual object position $x_v(t)$, only the first second is shown to better highlight the difference between the different values of the coefficient of restitution γ .

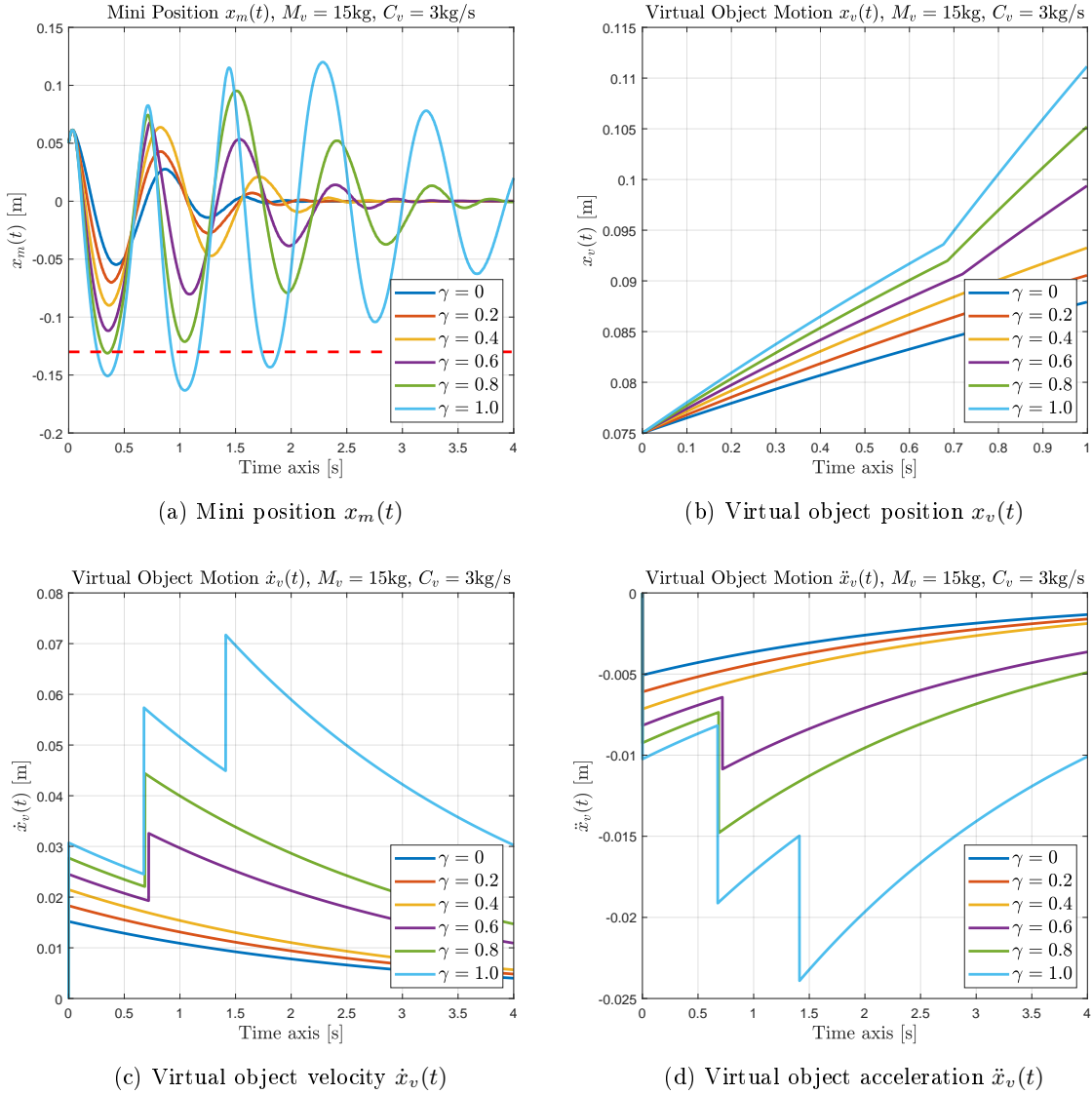


Figure 3.3 – Collision's response for different values of the coefficient of restitution γ . ($C_v = 3$ kg/s, $M_v = 15$ kg)

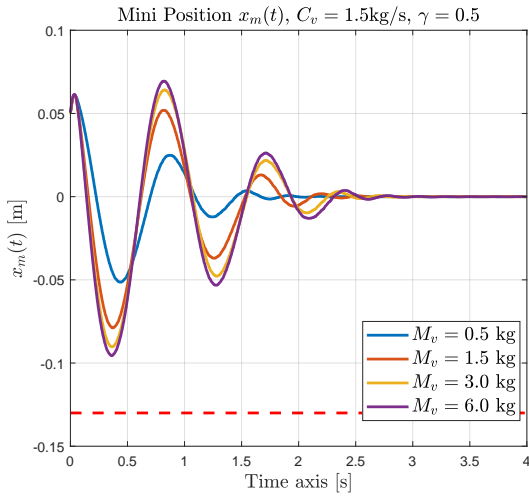
Higher values of the coefficient of restitution γ provide higher responses from both the mini mechanism and the virtual object. This is normal since a unit coefficient of restitution ($\gamma = 1$)

corresponds to a collision where no energy is lost (e.g. in heat, sound, etc...). With a coefficient of restitution equal or higher than $\gamma = 0.6$, the mini mechanism hits at least twice the virtual object. This is simply because the virtual object has a large mass ($M_v = 15$ kg) compared to the mini mechanism ($m = 0.3$ kg) and hence is not moving fast enough to escape a second collision. These repeated collisions are more easily seen in the virtual object velocity $\dot{x}_v(t)$ and acceleration $\ddot{x}_v(t)$ graphs. When the coefficient of restitution is too high (approximately $\gamma \geq 0.8$), the system seems to become unstable. This can be seen in the mini mechanism motion for $\gamma = 1.0$ where the return amplitude of the mini after the first collision (at $t \simeq 0.4$ s) is greater than the initial amplitude of the mini-mechanism which is indicated by the dashed red line. This means that the mini mechanism computed torque actually added energy to the system comprising the mini mechanism and the virtual object. One possible cause of this energy addition in the system is the sampling frequency of the collision detection algorithm [10].

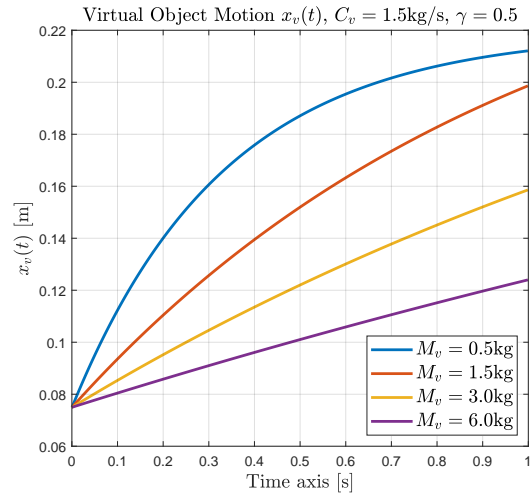
In the second experiment, the mass of the virtual object M_v is varied and the virtual damping and coefficient of restitution are fixed.

$$\begin{aligned} C_v &= 1.5 \text{ kg/s} \\ \gamma &= 0.5 \end{aligned} \rightarrow M_v = \{0.5 \ 1.5 \ 3.0 \ 6.0\} \text{ kg} \quad (3.15)$$

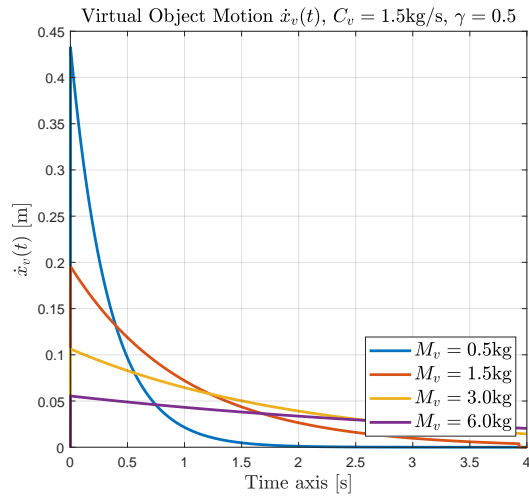
Figure 3.4 shows the results obtained. It can be noted that a higher virtual M_v causes the reaction force f_R to be larger, hence the mini mechanism amplitude response is higher. Another effect that can be observed is the deceleration rate for different values of the mass M_v . As seen in eq. 3.9, the deceleration rate is inversely proportional to the virtual mass M_v .



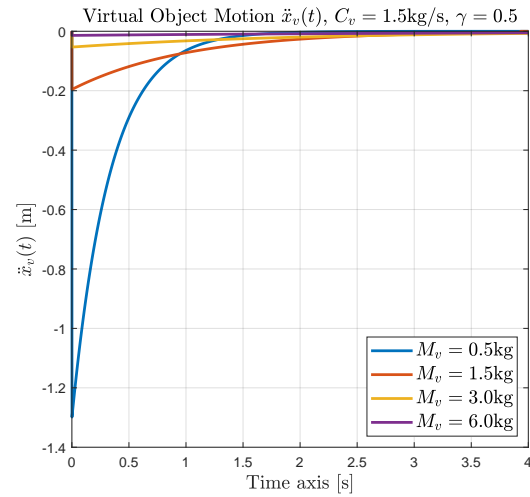
(a) Mini Position $x_m(t)$



(b) Virtual object position $x_v(t)$



(c) Virtual object velocity $\dot{x}_v(t)$



(d) Virtual object acceleration $\ddot{x}_v(t)$

Figure 3.4 – Collision’s response for different values of the virtual mass M_v . ($C_v = 1.5 \text{ kg/s}$, $\gamma = 0.5$)

In the last experiment, only the virtual damping C_v is varied, while the mass and coefficient of restitution are fixed.

$$\begin{aligned} M_v &= 3 \text{ kg} \\ \gamma &= 0.5 \end{aligned} \rightarrow C_v = \{0.5 \ 1.5 \ 3.0 \ 6.0\} \text{ kg/s} \quad (3.16)$$

Figure 3.5 shows the results obtained. Since the reaction force f_R is not dependent on the virtual damping C_v , the mini motion response is identical for all values of C_v . Contrary to the virtual mass M_v , the virtual object deceleration rate is proportional to the virtual damping.

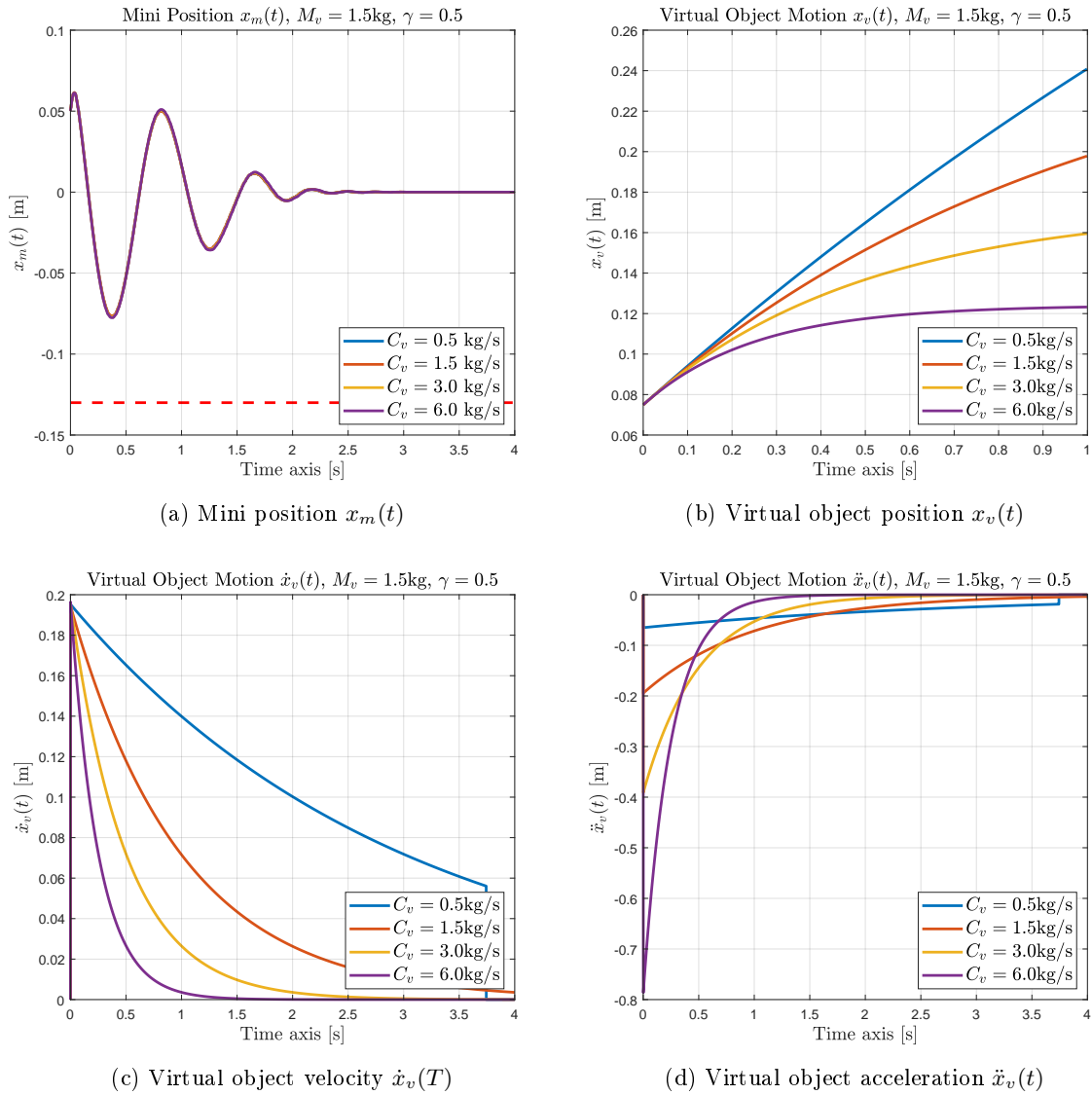


Figure 3.5 – Collision's response for different values of the virtual mass C_v . ($M_v = 1.5 \text{ kg}$, $\gamma = 0.5$)

3.2.3 Simulation of a Virtual Mass M_v at the Mini Mechanism End-Effector

The third interaction implemented is the simulation of a virtual mass attached to the end-effector of the mini mechanism. The virtual mass M_v is emulated using the active mini-mechanism. This subsection presents the mini mechanism control $\tau_c(t)$, the new dynamic equations of the system and a theoretical stability analysis similar to the previously presented for with the passive macro-mini system. Experimental results showing the effect of the virtual mass on the user's perception are also presented.

Mini Mechanism Command $\tau_c(t)$

The mini mechanism degree-of-freedom can be used to simulate a mass attached to the mini end-effector. If a real mass would be attached to the mini end-effector, the user would feel it from the gravity acceleration (g) and the mini angular acceleration ($\ddot{\theta}(t)$). The mini control torque $\tau_c(t)$ must therefore emulate the forces associated with these two accelerations. Figure 3.6 shows the schematic illustrating the virtual mass M_v added to the mini mass m .

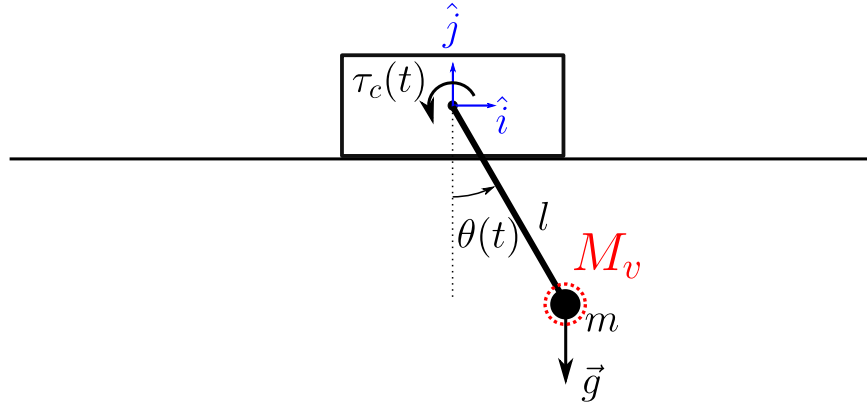


Figure 3.6 – Illustration of a virtual mass M_v attached to the mini end-effector. The virtual mass is simulated via the mini mechanism control torque $\tau_c(t)$.

The mini control torque corresponds to

$$\tau_c(t) = -M_v l g \sin(\theta(t)) - M_v l^2 \ddot{\theta}(t) \quad (3.17)$$

With the small angle approximation, this yields

$$\tau_c(t) \approx -M_v g \theta(t) - M_v l \ddot{\theta}(t) \quad (3.18)$$

Revision of the System Dynamics with a Virtual Mass M_v

The dynamic equations from Section 2.3 remain the same except for the new mini mechanism torque which is now non-zero. For clarity, the dynamic equation in translation (eq. 2.7) is repeated here.

$$F(t) = (M + m)\ddot{x}_M(t) + ml\ddot{\theta}(t) \quad (3.19)$$

The mini mechanism torque $\tau_c(t)$ is now added to eq. 2.13 which now yields the following equation:

$$ml\ddot{\theta}(t) = f_h(t) - (m + M_v)g\theta(t) - m\ddot{x}_M(t) - M_v g\ddot{\theta}(t) \quad (3.20)$$

Solving eq. 3.20 for the macro acceleration term $\ddot{x}(t)$ and substituting the results in eq. 3.19 finally gives

$$\ddot{x}(t) = \frac{f_h(t)}{m} - \left(\frac{m + M_v}{m}\right)g\theta(t) - \left(\frac{M_v}{m}\right)g\ddot{\theta}(t) - l\ddot{\theta}(t) \quad (3.21)$$

$$F(t) = \left(\frac{M + m}{m}\right)f_h(t) - \left(\frac{m + M_v}{m}\right)(M + m)g\theta(t) - \left(\frac{M_v}{m}\right)(M + m)g\ddot{\theta}(t) - Ml\ddot{\theta}(t) \quad (3.22)$$

Theoretical Stability Analysis

This subsection presents the theoretical stability analysis when using the variable stiffness controller (presented in section 2.5). For clarity, the controller eq. 2.42 is shown below.

$$F(t) = lC_d\dot{\theta}(t) + lK_d\theta(t) + lK_f\theta_f(t) \quad (3.23)$$

Using both eq. 3.22 and eq. 3.23 and solving for the external force $f_h(t)$ yields

$$\begin{aligned} B &= M + m \\ C &= \left(\frac{m + M_v}{m}\right) \end{aligned} \quad (3.24)$$

$$f_h(t) = \frac{1}{B}mlK_d\dot{\theta}(t) + Cmg\theta(t) + \frac{1}{B}lmK_f\theta_f(t) + \frac{1}{B}lmC_d\dot{\theta}(t) + M_v g\ddot{\theta}(t) + \frac{mMl}{B}\ddot{\theta}(t) \quad (3.25)$$

Taking the Laplace transform of eq. 3.25 yields the following expression:

$$F_H(s) = \Theta(s) \left[\frac{1}{B} mlK_d + Cmg + \frac{1}{B} lmK_f \left(\frac{\omega_c}{\omega_c + s} \right) + \frac{1}{B} lmC_d s + M_v g s^2 + \frac{mMl}{B} s^2 \right] \quad (3.26)$$

Equation 3.26 can be rearranged to have the same form as for the passive system stability analysis (2.48). The final form is presented below.

$$\frac{\Theta(s)}{F_H(s)} = \frac{B}{BM_v g + mMl} \left[\frac{b_1 s + b_0}{a_3 s^3 + a_2 s^2 + a_1 s + a_0} \right] \quad (3.27)$$

with

$$\begin{aligned} b_0 &= \omega_c \\ b_1 &= 1 \\ a_0 &= \omega_c \left[\frac{mlK_f + mlK_d + BCmg}{BM_v g + mMl} \right] \\ a_1 &= \frac{mlC_d \omega_c + mlK_d + BCmg}{BM_v g + mMl} \\ a_2 &= \frac{mlC_d}{BM_v g + mMl} + \omega_c \\ a_3 &= 1 \end{aligned} \quad (3.28)$$

With this form, the active system can be analyzed with the exact same method used for the passive system. While only the critically damped system will be explored here, the methodology described in section 2.5 can still be used to obtain a stable system. The expression for Δ and Δ_0 are repeated here for readability.

$$\begin{aligned} \Delta &= 18a_3 a_2 a_1 a_0 - 4a_2^3 a_0 + a_2^2 a_1^2 - 4a_3 a_1^3 - 27a_3^2 a_0^2 \\ \Delta_0 &= a_2^2 - 3a_3 a_1 \end{aligned} \quad (3.29)$$

To get a critically damped system, the condition $a_2 > 0$ must be satisfied. This means that

$$\frac{mlC_d}{BM_v g + mMl} + \omega_c > 0 \quad (3.30)$$

$$\frac{mlC_d}{BM_v g + mMl} > -\omega_c \quad (3.31)$$

$$C_d > -\frac{\omega_c (BM_v g + mMl)}{ml} \quad (3.32)$$

Since all the variables in eq. 3.32 are positive, this means that the virtual damping must be higher than a negative number, but not necessarily positive. Note the similitude with the condition stated for the passive mini mechanism (see eq. 2.57). In fact, if the virtual mass M_v is zero, the eq. 3.32 becomes identical to eq. 2.57. Again, we will use a more restricted condition on C_d , stating that the virtual damping of the controller must be a non-zero positive value.

$$C_d > 0 \quad (3.33)$$

Using the second condition ($\Delta_0 = 0$), we can define an expression for the virtual stiffness K_d as a function of the virtual damping C_d .

$$\begin{aligned} \Delta_0 &= 0 \\ a_2^2 - 3a_1 &= 0 \\ a_2^2 &= 3a_1 \end{aligned} \quad (3.34)$$

$$\left[\frac{mlC_d}{BM_vg + mMl} + \omega_c \right]^2 = 3 \left(\frac{mlC_d\omega_c + mlK_d + BCmg}{BM_vg + mMl} \right) \quad (3.35)$$

Solving eq. 3.35 for K_d yields the following expression.

$$K_d = \left(\frac{1}{ml} \right) \left[\frac{(mlC_d + \omega_c(BM_vg + mMl))^2}{3(BM_vg + mMl)} - (mlC_d\omega_c + BCmg) \right] \quad (3.36)$$

Note that if the virtual mass M_v is zero, then eq. 3.36 becomes identical to eq. 2.60.

Now using the last condition ($\Delta = 0$), an expression for K_f in terms of K_d and C_d can be obtained.

$$K_f = \frac{1}{27} \frac{(m(-2M\omega_c + C_d)l - 2\omega_c BM_vg)^3}{\omega_c ml (BM_vg + mMl)^2} \quad (3.37)$$

Theoretical Results

The influence of the virtual mass on the system is explored here with theoretical responses comparison. To compare with the passive system already analyzed (see section 2.5), the controller parameters experimentally found in the previous analysis are used again here.

$$\begin{aligned} K_d &= 1000 \text{ kg/s}^2 \\ C_d &= 400 \text{ kg/s} \\ K_f &= 500 \text{ kg/s}^2 \end{aligned} \tag{3.38}$$

The mini-mechanism responses $\theta(t)$ to a unit-impulse response $F_H(s) = 1$ for different values of the virtual mass M_v are illustrated in the figure below.

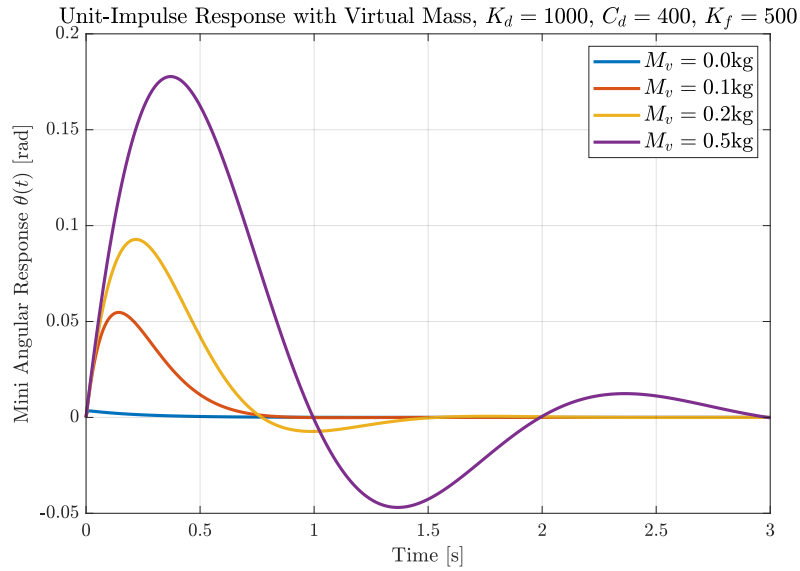


Figure 3.7 – Theoretical response to a unit-impulse force ($F_H(s) = 1$) for different values of the virtual mass M_v .

The theoretical results show that increasing the virtual mass M_v reduces the damping of the system. Indeed, the mini angular motion goes from an over-damped response (with $M_v \leq 0.1$ kg) to an under-damped response when $M_v > 0.1$ kg. Hence, simulating a mass at then end-effector of the mini mechanism is possible but must be implemented quite carefully to avoid an unstable behaviour of the system.

Experimental Validation

A simple experiment was designed to verify if the operator truly feels the effect of the virtual mass. First, the macro mechanism command is set to zero $\tau_m = 0$ Nm to ensure that it remains at rest. Then a force sensor is attached at the end-effector of the mini mechanism. This sensor is used to measure the force f_h used to move the mini mechanism as a function of the mini angular position $\theta(t)$. The sensor was calibrated in order to have its x -axis normal to the mini end-effector link. Note that due to the change in the mini mechanism end-effector (i.e. addition of force sensor), the mass of the mini, m , is now 0.28 kg.

The virtual mass is set to a specific value and the operator holds the end-effector at various angles between $\theta = -\pi/2$ and $\theta = \pi/2$. The force is measured at each angular position. For comparison, the theoretical force f_h is computed using eq. 3.40, taken from the rotational dynamic model. One has

$$\sum \tau_{\hat{k}}(t) = (m + M_v)l^2\ddot{\theta}(t) = lf_h(t) - (m + M_v)lg \sin \theta(t) \quad (3.39)$$

$$f_h(t) = (m + M_v)l\ddot{\theta}(t) + (m + M_v)g \sin \theta(t) \quad (3.40)$$

Since the measurements are taken in static conditions, the angular acceleration is zero and hence eq. 3.40 simplifies as

$$f_h(t) = (m + M_v)g \sin \theta(t) \quad (3.41)$$

Due to the very large number of data samples acquired by the controller, an automated process was designed to select force and angular measurements only when the mini mechanism is not accelerating. At rest, the typical angular acceleration measured was of the order of $\ddot{\theta}(t) = \pm 3$ rad/s². A threshold of $\delta_{\ddot{\theta}(t)} = 1$ rad/s² was used to select the relevant force and acceleration. In other words, the force and angular position were measured at each time step when $|\ddot{\theta}(t)| \leq \delta_{\ddot{\theta}(t)}$. Typical angular position and acceleration as well as force measurements are illustrated in figure 3.8.

Figure 3.9 shows the experimental results for four different virtual masses. The dashed curves represent the theoretical forces while the solid line curves represent the experimental measurements. It can be noted that the relative error between the theoretical force and the measured force is inversely proportional to the virtual mass M_v . This trend can be explained by inaccuracies in the dynamic model such as a lack of dry friction model or the oversimplification of the mini mechanism's mass distribution (m is considered a point mass at the end of link l). Such inaccuracies become less relevant for larger forces generated to emulate higher virtual mass M_v .

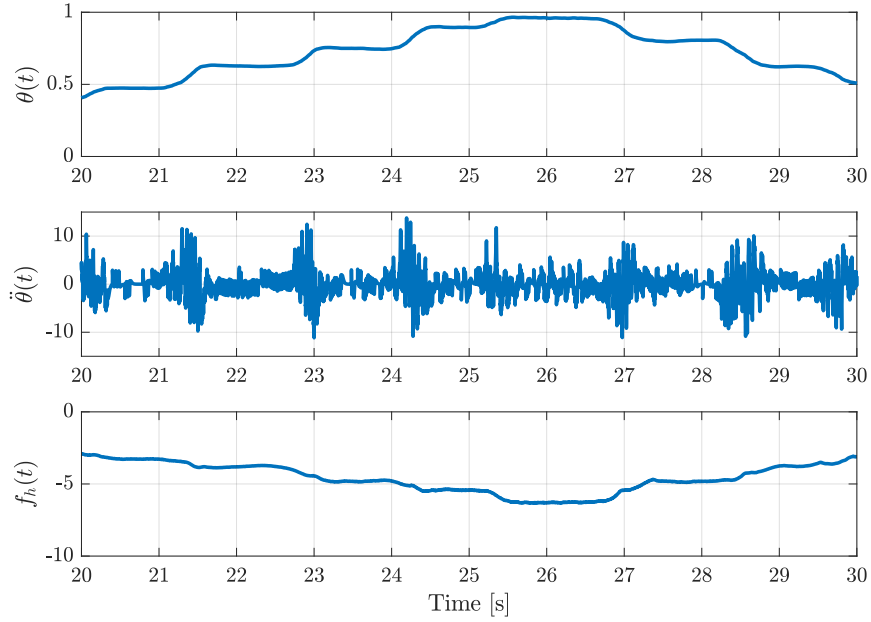
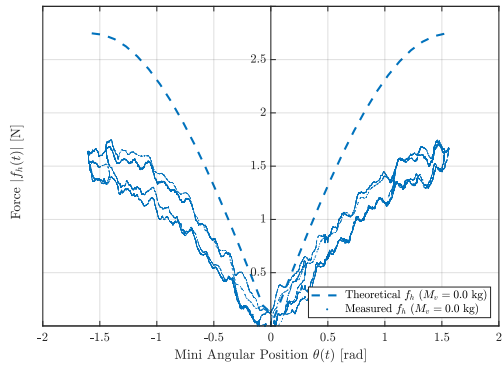
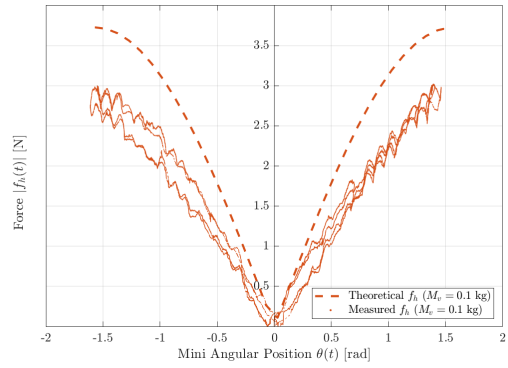


Figure 3.8 – Typical signal measured during the virtual mass experiment.

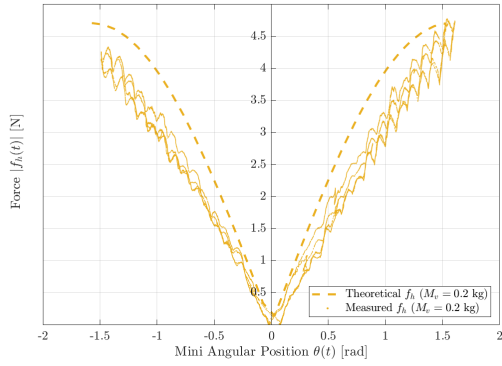
Another observation can be made regarding the measured force with a virtual mass of $M_v = 0.5$ kg. At the mini angular position limits — around $(\theta(t) = \pm\pi/2)$ — the measured force reaches a plateau at around $f_h = 6$ N. This is due to the mini mechanism motor limits. Indeed, the maximum torque that can be generated by the mini mechanism is about $(\tau_{c,max} = 0.9$ Nm). This represents a maximum generated force of approximately $(f_{h,max} = \tau_{c,max}/l = 4.7$ N). Adding the gravitational force acting on the mini mechanism mass ($f_g = mg = 2.7$ N), this yields a maximum theoretical force of $(f_{max} = 7.4$ N) to maintain the mini end-effector at $(\theta = \pm\pi/2)$.



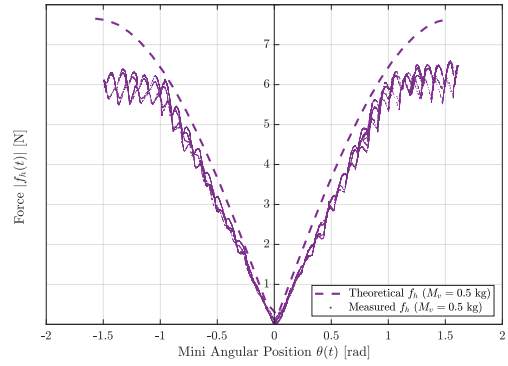
(a) $M_v = 0$ kg



(b) $M_v = 0.1$ kg



(c) $M_v = 0.2$ kg



(d) $M_v = 0.5$ kg

Figure 3.9 – Theoretical and experimental force f_h as a function of the mini angular position $\theta(t)$ and virtual mass M_v .

3.2.4 Conclusion

Two different limitations were observed during the experimental validations of the haptic feedback rendering. The first limitation comes from the mini mechanism's motor. Indeed, the motor can only generate a limited torque ($\tau_{c,max} = 0.94$ Nm). This directly affects the type and specification of object that can be rendered by the current macro mini architecture.

The second limitation comes from the method used to measure the mini velocity $\dot{x}_m(t)$ and acceleration $\ddot{x}_m(t)$. Numerical differentiation is sensitive to the noise in the signal and tends to amplify them it. Since the velocity is used to compute the collision reaction force f_R , there might be some inaccuracy causing unstable behaviour, as observed in figure 3.3.

A virtual mass M_v at the end-effector can effectively be emulated. Such an additional mass can be used to adapt the impedance felt by the user for different tasks. However the controller coefficients $\{K_d, C_d, K_f\}$ must be carefully adjusted as a function of the additional mass M_v to remain stable.

3.3 Planned Trajectory Motion

This section presents how a trajectory from point A to point B must be planned when using the macro-mini system, both with an active or passive mini mechanism. The first subsection explores the basics of trajectory motion for the macro system, without consideration of the passive mini mechanism. Experimental data are also shown to illustrate the consequence of having a passive joint. The second subsection presents how the active mini mechanism can be used to improve the motion.

3.3.1 Trajectory Planning of the Passive Mini Mechanism

The planned trajectory presented here are based on polynomial interpolation. This method is widely known and described in the literature [1, 5]. Other methods such as spline interpolation or even sum of sine functions could have been used [3]. However since the initial and final position are known, the polynomial interpolation is a good choice in terms of efficiency and simplicity.

The initial and final conditions of the motion are

$$\begin{aligned}x_M(t = 0) &= x_{M,A} \\ \dot{x}_M(t = 0) &= 0 \\ \ddot{x}_M(t = 0) &= 0 \\ x_M(t = t_f) &= x_{M,B} \\ \dot{x}_M(t = t_f) &= 0 \\ \ddot{x}_M(t = t_f) &= 0\end{aligned}\tag{3.42}$$

where t_f represents the time at which the macro is at rest at position $x_{M,B}$, and $x_M(t)$ represents the macro position at time t . Since there are a total of six (6) boundary conditions, the macro trajectory can be represented using a fifth-order polynomial, as shown below.

$$\begin{aligned}x_M(t) &= a_0 + a_1t + a_2t^2 + a_3t^3 + a_4t^4 + a_5t^5 \\ \dot{x}_M(t) &= a_1 + 2a_2t + 3a_3t^2 + 4a_4t^3 + 5a_5t^4 \\ \ddot{x}_M(t) &= 2a_2 + 6a_3t + 12a_4t^2 + 20a_5t^3\end{aligned}\tag{3.43}$$

Using the boundary conditions of (3.42) and the polynomials equations of (3.43), we can determine all six coefficients [11].

$$\begin{aligned}
a_0 &= x_{M,A} \\
a_1 &= a_2 = 0 \\
a_3 &= \frac{10(x_{M,B} - x_{M,A})}{t_f^3} \\
a_4 &= -\frac{15(x_{M,B} - x_{M,A})}{t_f^4} \\
a_5 &= \frac{6(x_{M,B} - x_{M,A})}{t_f^5}
\end{aligned} \tag{3.44}$$

Hence the polynomials of eq. 3.43 become

$$\begin{aligned}
x(t) &= x_{M,A} + \frac{10(x_{M,B} - x_{M,A})t^3}{t_f^3} - \frac{15(x_{M,B} - x_{M,A})t^4}{t_f^4} + \frac{6(x_{M,B} - x_{M,A})t^5}{t_f^5} \\
\dot{x}(t) &= \frac{30(x_{M,B} - x_{M,A})t^2}{t_f^3} - \frac{60(x_{M,B} - x_{M,A})t^3}{t_f^4} + \frac{30(x_{M,B} - x_{M,A})t^4}{t_f^5} \\
\ddot{x}(t) &= \frac{60(x_{M,B} - x_{M,A})t}{t_f^3} - \frac{180(x_{M,B} - x_{M,A})t^2}{t_f^4} + \frac{120(x_{M,B} - x_{M,A})t^3}{t_f^5}
\end{aligned} \tag{3.45}$$

These polynomials are represented in the graphs below for a normalized period T .

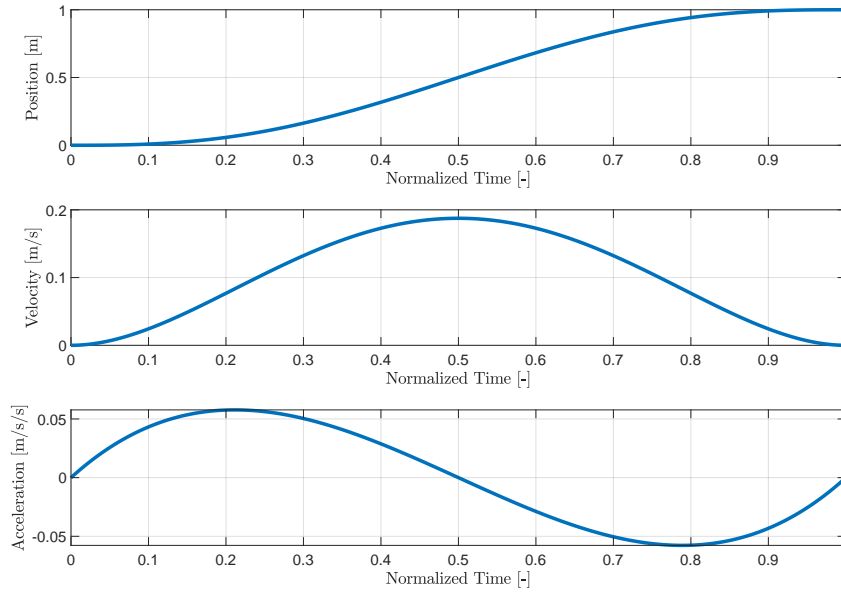


Figure 3.10 – Theoretical motion of the macro system. The time axis is normalized to the period $T = t_f - t_0$. The initial position is $x_A = 0 \text{ m}$ and the final position is $x_B = 1 \text{ m}$

Now the only remaining variable to determine is the total time to perform the trajectory, t_f . This can be done while ensuring that the maximum velocity \dot{x}_M^{max} and acceleration \ddot{x}_M^{max} of the macro mechanism is reached but never exceeded. The velocity $\dot{x}_M(t)$ reaches its maximum when its time derivative is zero and hence the following equation must be solved.

$$\ddot{x}_M(t) = \frac{60(x_{M,B} - x_{M,A})t}{t_f^3} - \frac{180(x_{M,B} - x_{M,A})t^2}{t_f^4} + \frac{120(x_{M,B} - x_{M,A})t^3}{t_f^5} = 0 \quad (3.46)$$

From the solution of eq. 3.46 for t , it appears clearly that the acceleration $\ddot{x}_M(t)$ is zero at three different times, namely

$$t = \{0, \frac{t_f}{2}, t_f\} \quad (3.47)$$

Using the central time $t = \frac{t_f}{2}$ yields

$$\dot{x}_M(t = t_f/2) = \frac{15(x_B - x_A)}{18 t_f} \leq \dot{x}_M^{max} \quad (3.48)$$

And hence

$$t_f \geq \frac{15(x_B - x_A)}{8 \dot{x}_M^{max}} \quad (3.49)$$

This is the minimal time that must be taken to perform the trajectory while ensuring that the macro's maximum reachable velocity is never exceeded. The second constraint to be satisfied is to ensure that the macro's maximum reachable acceleration \ddot{x}_M^{max} is never exceeded. The same process is used here for the acceleration.

$$\frac{d}{dt}\ddot{x}_M(t) = \frac{60(x_B - x_A)}{t_f^3} - \frac{360(x_B - x_A)t}{t_f^4} + \frac{360(x_B - x_A)t^2}{t_f^5} = 0 \quad (3.50)$$

The derivative of the acceleration is zero at two different times, namely

$$t = \left(0.5 \pm \frac{\sqrt{3}}{6}\right)t_f \quad (3.51)$$

Using these times in the acceleration polynomial gives the following minimum time period.

$$t_f \geq \sqrt{\frac{10\sqrt{3}}{3} \frac{|(x_B - x_A)|}{\ddot{x}_M^{max}}} \quad (3.52)$$

Equations (3.49) and (3.52) give the minimal time that must be taken to perform the trajectory while satisfying the system constraints. The highest of these two values must be used to ensure that all conditions are satisfied.

Experimental data were acquired using the same setup presented in Section 2.2. The macro was moved from $x_M = 0$ m to $x_M = 0.2$ m in the time period ($t_f = 1.1$ s). The distance travel represents the longest secure distance allowed by the experimental setup. With the selected trajectory duration, the maximum velocity and acceleration of the macro mechanism are never reached.

The following feedback loop was used to obtain the torque to be sent to the macro motor as a function of the reference velocity and position computed with the polynomials. An additional term is used to compensate for dry friction. This control is the same as the one used in Chapter 1, namely

$$\tau = K_p(x_M^{ref} - x_M) + K_v(\dot{x}_M^{ref} - \dot{x}_M) + \tau_f \quad (3.53)$$

where $(x_M^{ref}, \dot{x}_M^{ref})$ represent the computed trajectory and (x_M, \dot{x}_M) represent the measured macro motion. The gains for the controller were set to

$$\begin{aligned} K_p &= 2 \text{ N} \\ K_v &= 4 \text{ Ns} \\ \tau_f &= 2 \text{ Nm} \end{aligned} \quad (3.54)$$

Figure 3.11 shows comparisons between the theoretical and measured trajectory of the macro mechanism. It also shows the resulting mini motion. Using a feedback loop control for the macro motion allows the system to follow quite closely the reference motion. Note that the oscillation in the measured acceleration is a consequence of the numerical differentiation (twice).

As expected, there are small oscillations induced in the passive mini degree of freedom. This makes the mini end-effector to cross the commanded final position (0.2 m) slightly at the end. Due to the small macro velocity and the high friction at the passive joint, the oscillation is not too significant. But for a higher speed system, or a longer mini mechanism, the overshoot could quickly become a problem.

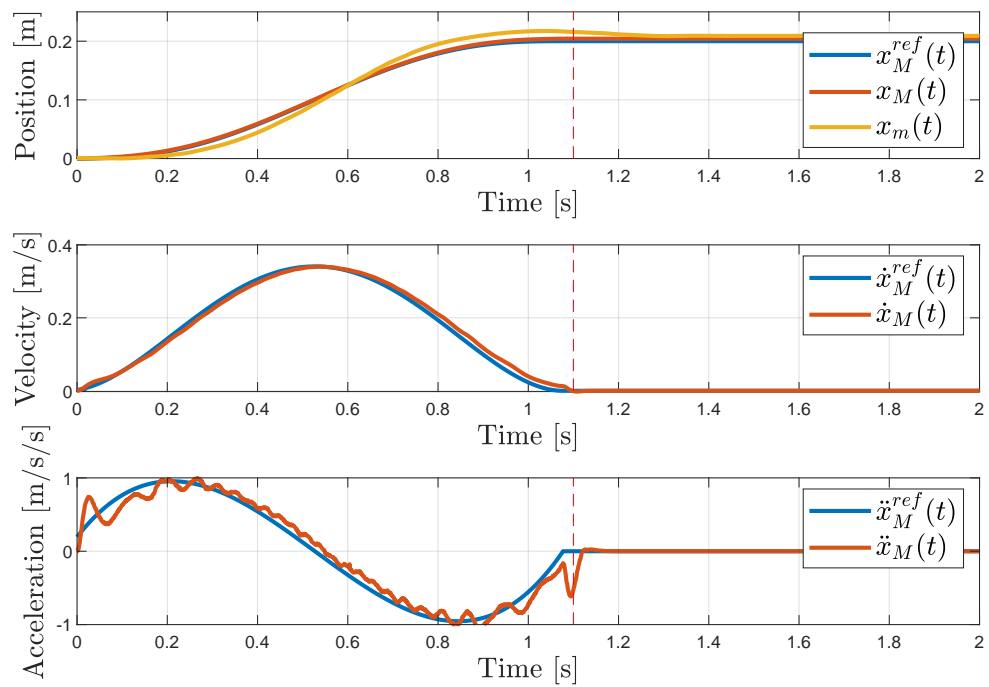


Figure 3.11 – Empirical results obtained for a motion from $x_A = 0$ m to $x_B = 0.2$ m.

This problem is commonly called in the literature the overhead crane problem. For such a system, the payload overshoot and oscillation removal is of critical importance for safety reasons. Many solutions for this problem can be found in the literature [2, 6, 8, 16, 17, 22, 24, 25, 26, 29, 28, 30] .

While the method described in [25] is simple, it is yet not perfect. Indeed, the macro planned motion relies on an open-loop control where the actual crane oscillation ($\theta(t)$) is never considered. To remove the crane oscillation, the planned motion relies on steep increases of velocity at specific times. These specific times are linked with the oscillation period of the crane, which is a function of its length. There are two major problems with such approaches. First, the anti-swing motion is dependent on the accuracy with which the crane length can be obtained. Second, the steep increase in velocity is practically not feasible by the system since the acceleration would be very large (jerky motion).

In [22] the crane input command is obtained via the inversion of the system's dynamics. In other words, the desired crane end-effector motion is used with the system's dynamic equations to determine the desired macro (crane) motion. It also uses a closed-loop controller, measuring the actual crane position and the cable's angular motion. Uncertainties on the cable length and payload mass are also taken into consideration in the motion planning.

A more recent paper [30] proposed a minimum-time trajectory planning approach that aims at computing the fastest trajectory from point x_A to x_B . The approach takes into consideration the system's limitations in velocity and acceleration, as well as the maximum acceptable end-effector swing angle θ . These limitations are used as constraints in the optimization process.

Other papers [6, 26] from the same authors provide other means of reducing crane oscillations. Paper [26] uses the same principle described in [25] but improves the method by reducing the jerk of the prescribed motion. In [6], a closed-loop controller is added to ensure that the planned trajectory is followed as closely as possible.

Most of the control methods found in the literature are dependent on the crane swing motion measurement. In [9] a method is proposed to estimate the swing motion directly from the voltage and current supplied to the crane motor. The system's dynamic model is used to estimate the swing motion and its effect on the power consumption of the motor.

3.3.2 Active Mini Mechanism Trajectory Planning

This section presents how the active mini mechanism can be used to reduce and eliminate the oscillation during planned trajectory motion. The new constraint — namely the maximum mini mechanism torque — is then added to the trajectory planning presented in Section 3.3.1.

The objective of activating the mini is to eliminate the oscillation (swing) motion of the mini end-effector. This objective can be written as

$$\begin{aligned}\theta(t) &= \theta_0 \\ \dot{\theta}(t) &= 0 \\ \ddot{\theta}(t) &= 0\end{aligned}\tag{3.55}$$

where θ_0 represents the initial angular position of the end-effector at the beginning of the planned motion. In practice, the initial angular position would be zero for most of the cases.

The mini angular motion was previously described in section 2.3. The dynamic equation in rotation — around axis \hat{k} — is rewritten below.

$$\sum \tau_{\hat{k}} = ml^2\ddot{\theta}(t) = \tau_c(t) + \tau_g(t) + \tau_x(t) + \tau_h(t)\tag{3.56}$$

$$\begin{aligned}\tau_g(t) &= -mgl \sin \theta(t) \\ \tau_x(t) &= -ml\ddot{x}_M(t) \cos \theta(t) \\ \tau_h(t) &= lf_h(t)\end{aligned}\tag{3.57}$$

In the case of planned trajectory motion, the external force $f_h(t)$ is considered to be zero at all times. With the small angle approximation and the constraints set from eq. 3.55, eq. 3.56 becomes

$$\sum \tau_{\hat{k}} = 0 = \tau_c(t) - mlg\theta(t) - ml\ddot{x}_M(t)\tag{3.58}$$

Solving for active mini torque $\tau_c(t)$ results in the following expression.

$$\tau_c(t) = ml[g\theta(t) + \ddot{x}_M(t)]\tag{3.59}$$

The mini torque command is therefore dependent on the mini angular position $\theta(t)$ and the macro mechanism acceleration $\ddot{x}_M(t)$. This command corresponds to a closed-loop control since the torque computed is expressed as a function of the mini angular position $\theta(t)$ which is updated at each time step. This creates a real-time compensation of possible motion of the

mini mechanism that could come from a variation from the dynamic model or inaccuracies in the macro mechanism acceleration.

Since the mini torque is dependent on the macro acceleration command, it adds a new constraint on the macro's planned motion. Indeed, to be able to eliminate the swing motion, the mini maximum torque τ_c^{max} must never be reached. The following equation shows the new constraint on the macro acceleration $\ddot{x}_M(t)$.

$$\tau_c(t) \leq \tau_c^{max} \quad (3.60)$$

$$\tau_c^{max} \geq ml[g\theta(t) + \ddot{x}_M(t)] \quad (3.61)$$

Hence, the following constraint on the macro acceleration must be satisfied.

$$\ddot{x}_M(t) \leq \frac{\tau_c^{max}}{ml} - g\theta(t) \quad (3.62)$$

The original planned trajectory described at the beginning of this section (see figure 3.10) is reused here with the active mini mechanism control of eq. 3.59. Again, the macro must move by a distance of $\Delta x = 0.2$ m in a time period of $t_f = 1.1$ s.

Figure 3.12 compares the mini mechanism motion with the passive and active mechanism. For the passive mini-mechanism, the maximum oscillation amplitude is about $\theta = 0.035$ rad (2°). The active mechanism reduces this maximum oscillation amplitude to $\theta = 0.0058$ rad (0.33°), which is about 6 times smaller than with the passive mechanism.

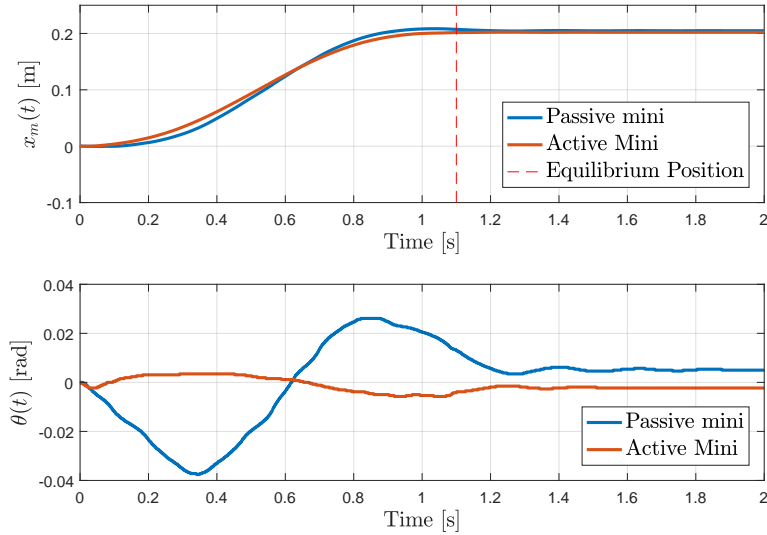


Figure 3.12 – Comparison of the mini position between the passive and active mechanism.

3.3.3 New Macro Acceleration Limits \ddot{x}_M^{max}

There are two limitations for the macro mechanism acceleration $\ddot{x}_M(t)$, the first is due to the macro mechanism itself (i.e. τ_M^{max}). The second limitation comes from the maximum torque τ_c^{max} that can be generated by the mini. At the end, the smallest of these limitation needs to be used to generate the planned trajectory motion (see eq. 3.52)

As stated, the first limitation comes from the maximum torque τ_M^{max} that can be generated by the macro. Using the torque constant and the maximum current I_M^{max} we obtain

$$\tau_M^{max} = \tau_{kM} I_M^{max} \quad (3.63)$$

Equation 2.21 is then used to link the maximum torque to the maximum force that the macro mechanism can generate.

$$F_M^{max} = \frac{2\pi\eta\tau_M^{max}}{\rho} \quad (3.64)$$

and using Newton's second law

$$F_M^{max} = (m + M)\ddot{x}_M^{max1} \quad (3.65)$$

Solving eq. 3.65 for \ddot{x}_M^{max} gives the first acceleration limit, namely

$$\ddot{x}_M^{max1} = \frac{2\pi\eta\tau_{kM}I_M^{max}}{\rho(m + M)} \quad (3.66)$$

The second limitation is dependent on the maximum torque that the mini can generate. Using the maximum mini current I_m^{max} and eq. 3.62, the following relation can be found:

$$\ddot{x}_M^{max2} = \frac{\tau_{km}I_m^{max}}{ml} - g\theta(t) \quad (3.67)$$

The new acceleration limits for the macro mechanism correspond to the smallest of the following two.

$$\ddot{x}_M^{max} = \min \left[\frac{2\pi\eta\tau_{kM}I_M^{max}}{\rho(m + M)}, \frac{\tau_{km}I_m^{max}}{ml} - g\theta(t) \right] \quad (3.68)$$

3.3.4 Conclusion

The use of the active mini mechanism greatly simplifies the trajectory planning of the macro-mini architecture compared with other methods from the literature. The oscillation at the mini's joint are greatly reduced, as demonstrated with the experimental results. The only disadvantage is that the macro mechanism acceleration is now limited by the maximum torque that the mini mechanism can generate.

3.4 Trajectories Involving Interactions with the Environment

One of the advantages of admittance control over impedance control is the ability to easily measure the interaction force with the environment. Indeed, the force and torque sensor used to monitor the interaction force between the collaborative robot and the operator can also be used to detect unwanted environment interaction such as collisions with an object or even a person.

With the current system, environment interactions are detected via motion of the mini mechanism. For manual operation, the macro mechanism is directly controlled using the mini motion. Since the mini mechanism has a very low-impedance, the control can be deemed safe. However, in the case of a planned trajectory motion where the mini mechanism is actively controlled to reduce oscillation and relative motion of the payload, a collision will only cause the mini mechanism to resist even more against the collided object. Hence in its current form, the trajectory planning algorithm of the active macro mini mechanism is not safe for human-robot collaboration.

This section aims at presenting how to measure force interaction during planned-trajectory motion using only the mini encoder measurement and the previously described dynamic model. Subsection 3.4.1 presents the theoretical foundation and Subsection 3.4.2 presents experimental results. .

3.4.1 Theoretical Foundation

During planned trajectory motion, the macro mechanism's motion is described by eq. 3.45 and the mini mechanism command corresponds to eq. 3.59. It is of interest here to measure the interaction force f_h at the end-effector of the mini mechanism (see figure 2.3).

Recall the original dynamic equation in rotation around the mini mechanism's axis of rotation previously presented in Section 2.3 (repeated below). The major difference with the passive system is the non-zero mini torque $\tau_c(t)$ command. Note that the small angle approximation is already applied to the different torque relations below.

$$\sum \tau_{\tilde{k}}(t) = ml^2\ddot{\theta}(t) = \tau_c(t) + \tau_g(t) + \tau_x(t) + \tau_h(t) \quad (3.69)$$

$$\begin{aligned} \tau_c(t) &= ml[g\theta(t) + \ddot{x}_M(t)] \\ \tau_g(t) &= -mlg\theta(t) \\ \tau_x(t) &= -ml\ddot{x}(t) \\ \tau_h(t) &= lf_h(t) \end{aligned} \quad (3.70)$$

Hence eq. 3.69 can be written as

$$ml^2\ddot{\theta}(t) = mlg\theta(t) + ml\ddot{x}_M(t) - mlg\theta(t) - ml\ddot{x}_M(t) + lf_h(t) \quad (3.71)$$

which can now be simplified as

$$f_h(t) = ml\ddot{\theta}(t) \quad (3.72)$$

Therefore the force $f_h(t)$ is directly related to the mini angular acceleration. This is possible because the mini torque command $\tau_c(t)$ is already compensating for the gravitational acceleration g and the macro acceleration \ddot{x}_M . Hence the only remaining force affecting the system should be an external force $f_h(t)$.

While eq. 3.72 is quite simple, some potential problems can arise from using such a method to measure external forces. A first possible problem comes from unmodelled forces in the system, such as friction at the mini mechanism's rotational joint.

Another issue is the method used to measure the angular acceleration $\ddot{\theta}(t)$. In practice, the encoder measurement needs to be numerically differentiated twice to obtain the angular acceleration. Such a numerical method tends to amplify the signal noise. A solution to this problem would be to low-pass the encoder signal. However, such a filtering necessarily generates delays in the angular acceleration signal, which can render its use inefficient. It is recalled that the objective of the force sensing is operator safety.

The next subsection presents experimental results obtained using the presented method. The forces measured with eq. 3.72 are compared with actual force measurement using a force sensor attached to the mini end-effector. The problems discussed earlier are also explored in more details.

3.4.2 Experimental Results

For this experiment, the force sensor used is the same as the one used in Section 3.2.3. The trajectory described and implemented in Section 3.3.2 was also re-used. The macro goes from position $x_M(t = 0) = 0$ m to $x_M(t = 1.1) = 0.2$ m and the mini mechanism is actively compensating to reduce the angular oscillation.

In order to illustrate how the computed force can be noisy, the first run was done without any collision. Hence the measured and computed force should be zero at all times. Figure 3.13 shows the experimental results for this run. The measured force — using the force sensor — is limited within $f_h = \pm 0.1$ N. The computed force however is a lot more noisy. There is a peak at the beginning of the motion caused by the macro’s initial acceleration. This is a sign that there is a small delay in the mini mechanism command τ_c as it does not perfectly eliminate the mini oscillation.

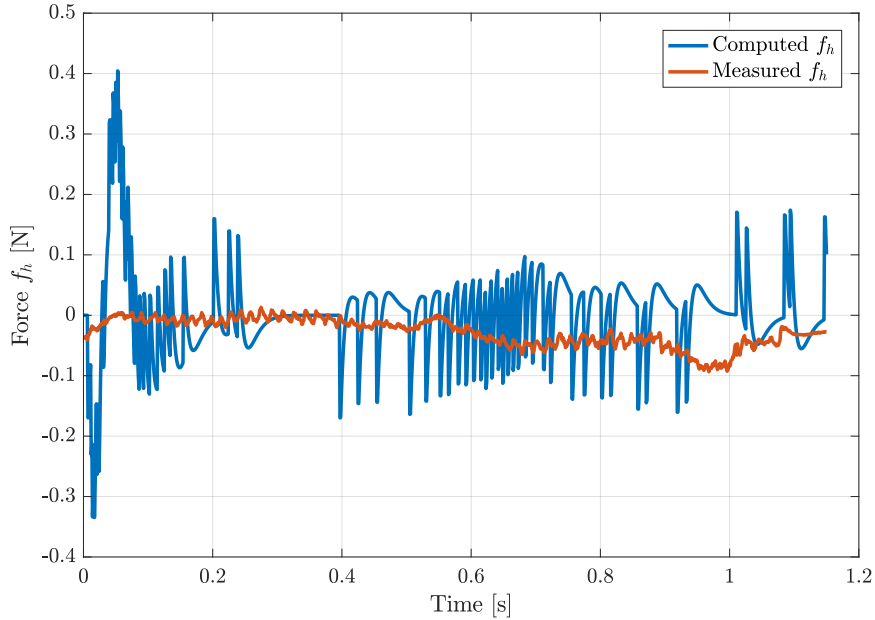


Figure 3.13 – Forces during trajectory motion, no collision.

Figure 3.14 shows a second run where the mini end-effector collided with a human hand. The collision occurred at around $t = 0.4$ s from the beginning of the trajectory. As seen before, there is a computed force peak at the beginning of the motion of about $f_h = \pm 0.5$ N.

While the system’s dynamic model does not allow for precise force measurement, collisions are easily detected due to the very sensitive angular acceleration measurement, which is directly linked with the measured force (see eq. 3.72).

A simple threshold in computed force f_h — or even in angular acceleration $\ddot{\theta}(t)$ — could be

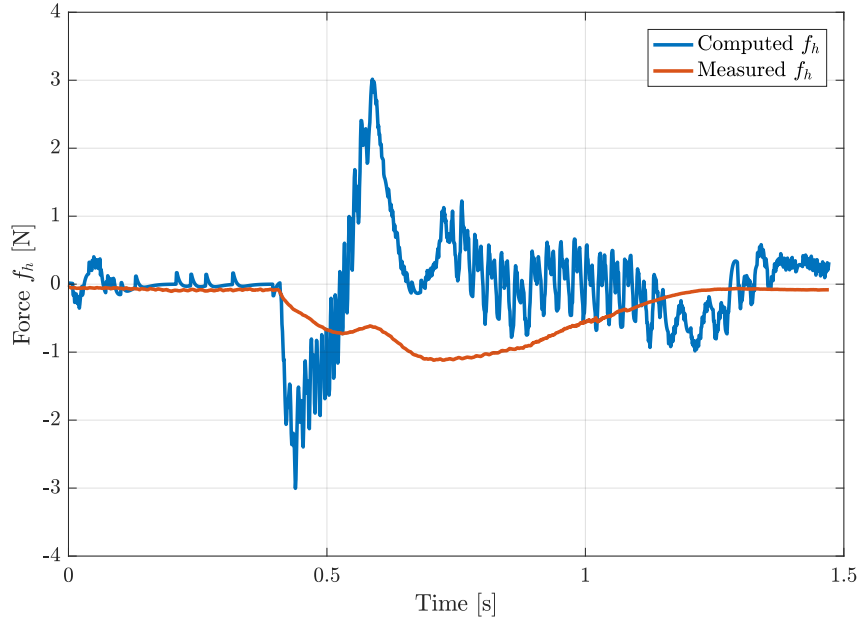


Figure 3.14 – Forces during trajectory motion, collision occurs at $c. t = 0.4s$ during the trajectory.

used for collision detection. To be effective, the threshold should be higher than the force peak computed at the beginning of the motion. In the current case, a threshold of $|f_{threshold}| = 1$ N could be used safely.

3.4.3 Conclusion

The last experimental results clearly show the advantage of using an active mini mechanism to compensate for the gravitational and macro mechanism acceleration perturbations during planned trajectory motion. Indeed, it simplifies greatly the collision detection since it does not require external force sensor or proximity detector. The mini mechanism’s encoding system — with the knowledge of the mini end-effector length l and the payload mass m — is sufficient to safely detect collision.

In the current work, a threshold as small as 1 N is adequate for collision detection. Of course, this threshold needs to be adjusted according to the end-effector length l and payload mass m as the force computed is directly proportional to these quantities (see eq. 3.72).

For comparison, the smallest maximum permissible force stated in Appendix A of the norm ISO/TS-15066 [13] is 65 N and smallest pressure limit is 110 N/cm². Note that the different body regions have different force and pressure thresholds. These limits can be used to set the collision detection threshold but also to limit the velocity and acceleration of the macro-mini architecture during planned trajectory motion.

3.5 Conclusion

While Chapter 2 described and analyzed the control of a passive macro mini mechanism, this chapter aimed at presenting the advantage of using an active macro mini architecture. It was shown that using backdrivable motors at the mini mechanism joints, the flexibility and intuitiveness of the passive manual control could be combined with haptic feedback. The active mini joint could also be used to reduce the payload oscillation during planned trajectory motion without over-complexifying the macro mechanism controller. Even a collision detection algorithm was implemented and compared with traditional force sensor measurement.

In terms of haptic feedback, several interactions with virtual objects were positively rendered with the active macro-mini mechanism. Unfortunately the mini joint's maximum producible torque (approximately 5 Nm) was a limiting factor for stiff wall rendering since the control saturated quite quickly. Virtual objects were also rendered using the active mini mechanism with still limitations on the virtual mass that could be rendered. Another issue with the virtual object rendering is the coefficient of restitution used that affects the system stability. Indeed, a coefficient of restitution greater than $\gamma \geq 0.8$ would cause instability by adding energy in the system composed of the macro-mini mechanism and the virtual world produced [4, 10]. At last, the simulation of a virtual mass at the mini end-effector adequately modifies the impedance felt by the user without compromising the system stability. Here also, the mini joint's maximum torque could only render a virtual mass of $M_v < 0.5$ kg in the presented experiment.

Another aspect explored was the use of the active mini joint to compensate and reduce the angular oscillation of the payload during planned trajectory motion of the macro mechanism. Also known as the overhead crane problem, the payload oscillation at the end of the mini mechanism could have been reduced using more complex trajectory for the macro using the system dynamic model. The active joint at the mini mechanism simplifies greatly this problem by compensating the gravitational and the macro mechanism acceleration. However, this method is quite dependent on the mini link length l and the payload mass m . Any inaccuracy in these two terms will reduce the oscillation compensation effects.

The last element considered is one of human safety. One advantage of admittance control over impedance control is that the use of a force sensor allows one to easily detect environment interaction and collision. Another approach was presented here to detect collision during planned trajectory motion using solely the encoder measurement of the mini joint. This method was compared with measurements from a force sensor attached to the mini end-effector. While the forces computed with this method are not quite as precise, a simple force threshold could yet be used for collision detection. In fact the collision is more easily distinguished with this method than with the force sensor signal.

3.6 Bibliography

- [1] Jorge Angeles. *Fundamentals of robotic mechanical systems*, volume 2. Springer, 2002.
- [2] Wojciech Blajer and K Kołodziejczyk. Motion planning and control of gantry cranes in cluttered work environment. *IET Control Theory & Applications*, 1(5):1370–1379, 2007.
- [3] Michael Brady, John M Hollerbach, Timothy L Johnson, Tomás Lozano-Pérez, Matthew T Mason, Daniel G Bobrow, Patrick Henry Winston, and Randall Davis. *Robot motion: Planning and control*. MIT press, 1982.
- [4] Daniela Constantinescu, Septimiu E Salcudean, and Elizabeth A Croft. Local model of interaction for haptic manipulation of rigid virtual worlds. *The International Journal of Robotics Research*, 24(10):789–804, 2005.
- [5] John J Craig. *Introduction to robotics: mechanics and control, 3/E*. Pearson Education India, 2009.
- [6] Yongchun Fang, Bojun Ma, Pengcheng Wang, and Xuebo Zhang. A motion planning-based adaptive control method for an underactuated crane system. *IEEE Transactions on Control Systems Technology*, 20(1):241–248, 2011.
- [7] J Randall Flanagan and Susan J Lederman. Neurobiology: Feeling bumps and holes. *Nature*, 412(6845):389, 2001.
- [8] Santiago Garrido, Mohamed Abderrahim, Antonio Giménez, Ramiro Diez, and Carlos Balaguer. Anti-swinging input shaping control of an automatic construction crane. *IEEE Transactions on Automation Science and Engineering*, 5(3):549–557, 2008.
- [9] Amin Gholabi, Mohammad Ebrahimi, Gholam Reza Yousefi, Mostafa Ghayour, Ali Ebrahimi, and Hamed Jali. Sensorless anti-swing control for overhead crane using voltage and current measurements. *Journal of Vibration and Control*, 21(9):1745–1756, 2015.
- [10] R Brent Gillespie and Mark R Cutkosky. Stable user-specific haptic rendering of the virtual wall. In *Proceedings of the ASME International Mechanical Engineering Congress and Exhibition*, volume 58, pages 397–406, 1996.
- [11] CM Gosselin and A Hadj-Messaoud. Automatic planning of smooth trajectories for pick-and-place operations. *Journal of Mechanical Design*, 115(3):450–456, 1993.
- [12] Vincent Hayward, Oliver R Astley, Manuel Cruz-Hernandez, Danny Grant, and Gabriel Robles-De-La-Torre. Haptic interfaces and devices. *Sensor review*, 2004.
- [13] ISO ISO. Ts 15066 (2016): robots and robotic devices—collaborative robots. *Geneva: International Organization for Standardization*, 2016.

- [14] Pascal D Labrecque, Thierry Laliberté, Simon Foucault, Muhammad E Abdallah, and Clément Gosselin. Uman: A low-impedance manipulator for human–robot cooperation based on underactuated redundancy. *IEEE/ASME Transactions on Mechatronics*, 22(3):1401–1411, 2017.
- [15] Susan J Lederman and Roberta L Klatzky. Hand movements: A window into haptic object recognition. *Cognitive psychology*, 19(3):342–368, 1987.
- [16] H-H Lee*. Motion planning for three-dimensional overhead cranes with high-speed load hoisting. *International Journal of Control*, 78(12):875–886, 2005.
- [17] Ziyad N Masoud and Ali H Nayfeh. Sway reduction on container cranes using delayed feedback controller. *Nonlinear dynamics*, 34(3-4):347–358, 2003.
- [18] Thomas H Massie, J Kenneth Salisbury, et al. The phantom haptic interface: A device for probing virtual objects. In *Proceedings of the ASME winter annual meeting, symposium on haptic interfaces for virtual environment and teleoperator systems*, volume 55, pages 295–300. Citeseer, 1994.
- [19] Margaret Minsky, Ouh-young Ming, Oliver Steele, Frederick P Brooks Jr, and Max Behensky. Feeling and seeing: issues in force display. In *ACM SIGGRAPH Computer Graphics*, volume 24, pages 235–241. ACM, 1990.
- [20] Allison M Okamura, Robert J Webster, Jason T Nolin, KW Johnson, and H Jafry. The haptic scissors: Cutting in virtual environments. In *2003 IEEE International Conference on Robotics and Automation (Cat. No. 03CH37422)*, volume 1, pages 828–833. IEEE, 2003.
- [21] Michael Ortega, Stephane Redon, and Sabine Coquillart. A six degree-of-freedom god-object method for haptic display of rigid bodies. In *IEEE Virtual Reality Conference (VR 2006)*, pages 191–198. IEEE, 2006.
- [22] Aurelio Piazzì and Antonio Visioli. Optimal dynamic-inversion-based control of an overhead crane. *IEE Proceedings-Control Theory and Applications*, 149(5):405–411, 2002.
- [23] Kenneth Salisbury, Francois Conti, and Federico Barbagli. Haptic rendering: introductory concepts. *IEEE computer graphics and applications*, 24(2):24–32, 2004.
- [24] Khalid L Sorensen, William Singhose, and Stephen Dickerson. A controller enabling precise positioning and sway reduction in bridge and gantry cranes. *Control Engineering Practice*, 15(7):825–837, 2007.
- [25] GP Starr. Swing-free transport of suspended objects with a path-controlled robot manipulator. 1985.

- [26] N Sun, Y Fang, X Zhang, and Y Yuan. Transportation task-oriented trajectory planning for underactuated overhead cranes using geometric analysis. *IET Control Theory & Applications*, 6(10):1410–1423, 2012.
- [27] Richard Q Van der Linde, Piet Lammertse, Erwin Frederiksen, and B Ruiter. The hapticmaster, a new high-performance haptic interface. In *Proc. Eurohaptics*, pages 1–5, 2002.
- [28] Xianqing Wu and Xiongxiang He. Enhanced damping-based anti-swing control method for underactuated overhead cranes. *IET Control Theory & Applications*, 9(12):1893–1900, 2015.
- [29] Zhou Wu and Xiaohua Xia. Optimal motion planning for overhead cranes. *IET Control Theory & Applications*, 8(17):1833–1842, 2014.
- [30] Xuebo Zhang, Yongchun Fang, and Ning Sun. Minimum-time trajectory planning for underactuated overhead crane systems with state and control constraints, 2014.
- [31] Craig B Zilles and J Kenneth Salisbury. A constraint-based god-object method for haptic display. In *Proceedings 1995 IEEE/RSJ International Conference on Intelligent Robots and Systems. Human Robot Interaction and Cooperative Robots*, volume 3, pages 146–151. IEEE, 1995.

Conclusion

The goal of this research was to demonstrate the advantages of using a low-impedance mini mechanism with an impedance controller to interface with a high-impedance macro mechanism for intuitive physical human-robot interactions. The main objectives were to design and evaluate a stable impedance controller, to compare the performance with a standard admittance control for similar tasks, to implement and test haptic feedback rendering with the addition of a backdrivable motor to the mini mechanism joint and to devise a stable and safe trajectory motion strategy for autonomous control.

Chapter 1 thoroughly described the design and dynamics of the passive parallel mechanism used to control a three-degree-of-freedom gantry robot. Among other things, it was demonstrated that the macro-mini mechanism provides a more intuitive and effortless means to control the gantry robot than standard admittance control, as proved by a simple peg-in-hole experiment. Indeed, the average time and force required to complete the task were ($T = 11.7$ s, $F = 0.66$ N) for the impedance controller, compared to ($T = 28.6$ s, $F = 20.6$ N) for the admittance controller.

Chapter 2 aimed at analyzing in more details the use of impedance control with similar macro-mini architecture. Since the mini mechanism is dynamically decoupled, a simplified single degree of freedom was used for a more thorough analysis of the impedance controller. The results obtained can be converted to a multi-dimensional macro-mini system without much modifications. The stability analysis demonstrated that the standard impedance controller — using a virtual mass M_d , a virtual damping C_d and a virtual stiffness K_d — leads to unstable behaviours. In fact, instabilities occur as soon as a non-zero virtual mass M_d is integrated into the controller. An alternative impedance controller — which uses a second virtual stiffness K_f linked to a low-pass filtered version of the angular position $\theta(t)$ — was therefore proposed and analyzed for stability performance. This controller proved to be more stable and intuitive than the initial standard controller.

Chapter 3 aimed at presenting other control strategies that could be used with the addition of a backdrivable motor at the mini mechanism joint. First of all, this additional actuated degree of freedom allows for haptic feedback rendering. It was demonstrated that virtual objects could be simulated and effectively felt by the user. The impedance felt by the user

when manipulating the mini mechanism control could even be modified by simulating a virtual mass M_v attached to the mini end-effector. One limit though of such haptic feedback comes from the maximum torque that the mini could generate, in the current study the limit was ($\tau_{c,max} \approx 5$ Nm). This considerably limits the virtual interactions that could be generated by the experimental setup. In fact, wall constraints could not be properly emulated as the interactions did not feel stiff enough.

Another aspect discussed is the autonomous motion of the macro mechanism. A disadvantage of the macro-mini architecture over the use of force sensor for the control is the additional passive degree of freedom. It was demonstrated that during planned motion of the macro mechanism, the payload — or for the current study the mini end-effector — was oscillating around the mini mechanism’s workspace centre. This behaviour poses safety risks if the payload mass is higher or if the macro moves at a considerable velocity. With the addition of a backdrivable motor to the mini mechanism joint, the oscillations can be compensated easily using the dynamic model of the system. For the experimental setup, the oscillations amplitude was reduced by a factor of 6 with the actuated mini mechanism.

Using the dynamic model, a simple collision detection method was designed and evaluated. The method consists in using the angular acceleration of the mini mechanism to compute interaction forces with the environment. Since the mini mechanism is actively compensating for oscillations caused by the macro motion, the mini angular position is considered to remain fixed except when a collision occurs. While the interaction forces cannot be precisely computed, collisions are easily detected. In fact, the collision seems to be more easily detected using this method than with a force sensor attached to the mini end-effector.

It was therefore demonstrated that impedance control with an actuated low-impedance mini mechanism interface can be safely and intuitively used for manual control of a gantry system and also for autonomous motion of the payload. The collision detection method ensures safe physical human-robot interactions.

The controller developed in the course of this research can now be implemented on the multi-dimensional macro-mini system presented in Chapter 1. Future work includes the design of a more robust parallel mechanism with the addition of backdrivable motors at the actuated joints. Also, some adaptations remain for the vertical axis motion as this particular degree of freedom must compensate for the gravitational acceleration. A calibration method could also be designed to automatically measure the payload mass using the backdrivable motor associated with the vertical axis of motion and henceforth adjusting the controller gains with regards to this measured mass.

Bibliography

- [Angeles, 2002] Angeles, J. (2002). *Fundamentals of robotic mechanical systems*, volume 2. Springer.
- [Blajer and Kołodziejczyk, 2007] Blajer, W. and Kołodziejczyk, K. (2007). Motion planning and control of gantry cranes in cluttered work environment. *IET Control Theory & Applications*, 1(5):1370–1379.
- [Brady et al., 1982] Brady, M., Hollerbach, J. M., Johnson, T. L., Lozano-Pérez, T., Mason, M. T., Bobrow, D. G., Winston, P. H., and Davis, R. (1982). *Robot motion: Planning and control*. MIT press.
- [Buerger and Hogan, 2007] Buerger, S. P. and Hogan, N. (2007). Complementary stability and loop shaping for improved human–robot interaction. *IEEE Transactions on Robotics*, 23(2):232–244.
- [Campeau-Lecours et al., 2016] Campeau-Lecours, A., Foucault, S., Laliberté, T., Mayer-St-Onge, B., and Gosselin, C. (2016). A cable-suspended intelligent crane assist device for the intuitive manipulation of large payloads. *IEEE/ASME Transactions on Mechatronics*, 21(4):2073–2084.
- [Cherubini et al., 2016] Cherubini, A., Passama, R., Crosnier, A., Lasnier, A., and Fraitse, P. (2016). Collaborative manufacturing with physical human–robot interaction. *Robotics and Computer-Integrated Manufacturing*, 40:1–13.
- [Colgate and Hogan, 1989] Colgate, E. and Hogan, N. (1989). An analysis of contact instability in terms of passive physical equivalents. In *Proceedings, 1989 international conference on robotics and automation*, pages 404–409. IEEE.
- [Colgate, 1994] Colgate, J. (1994). Coupled stability of multiport systems—theory and experiments.
- [Colgate and Hogan, 1988] Colgate, J. E. and Hogan, N. (1988). Robust control of dynamically interacting systems. *International journal of Control*, 48(1):65–88.

- [Constantinescu et al., 2005] Constantinescu, D., Salcudean, S. E., and Croft, E. A. (2005). Local model of interaction for haptic manipulation of rigid virtual worlds. *The International Journal of Robotics Research*, 24(10):789–804.
- [Craig, 2009] Craig, J. J. (2009). *Introduction to robotics: mechanics and control*, 3/E. Pearson Education India.
- [Fang et al., 2011] Fang, Y., Ma, B., Wang, P., and Zhang, X. (2011). A motion planning-based adaptive control method for an underactuated crane system. *IEEE Transactions on Control Systems Technology*, 20(1):241–248.
- [Flanagan and Lederman, 2001] Flanagan, J. R. and Lederman, S. J. (2001). Neurobiology: Feeling bumps and holes. *Nature*, 412(6845):389.
- [Garrido et al., 2008] Garrido, S., Abderrahim, M., Giménez, A., Diez, R., and Balaguer, C. (2008). Anti-swinging input shaping control of an automatic construction crane. *IEEE Transactions on Automation Science and Engineering*, 5(3):549–557.
- [Gholabi et al., 2015] Gholabi, A., Ebrahimi, M., Yousefi, G. R., Ghayour, M., Ebrahimi, A., and Jali, H. (2015). Sensorless anti-swing control for overhead crane using voltage and current measurements. *Journal of Vibration and Control*, 21(9):1745–1756.
- [Gillespie and Cutkosky, 1996] Gillespie, R. B. and Cutkosky, M. R. (1996). Stable user-specific haptic rendering of the virtual wall. In *Proceedings of the ASME International Mechanical Engineering Congress and Exhibition*, volume 58, pages 397–406.
- [Gosselin and Hadj-Messaoud, 1993] Gosselin, C. and Hadj-Messaoud, A. (1993). Automatic planning of smooth trajectories for pick-and-place operations. *Journal of Mechanical Design*, 115(3):450–456.
- [Gosselin et al., 2004] Gosselin, C., Kong, X., Foucault, S., and Bonev, I. (2004). A fully decoupled 3-dof translational parallel mechanism. *Parallel Kinematic Machines International Conference*, pages 595–610.
- [Gosselin et al., 2007] Gosselin, C. M., Masouleh, M. T., Duchaine, V., Richard, P.-L., Foucault, S., and Kong, X. (2007). Parallel mechanisms of the multipteron family: kinematic architectures and benchmarking. In *Proceedings 2007 IEEE International Conference on Robotics and Automation*, pages 555–560. IEEE.
- [Hayward et al., 2004] Hayward, V., Astley, O. R., Cruz-Hernandez, M., Grant, D., and Robles-De-La-Torre, G. (2004). Haptic interfaces and devices. *Sensor review*.
- [Hogan, 1984] Hogan, N. (1984). Impedance control: An approach to manipulation. In *1984 American control conference*, pages 304–313. IEEE.

- [Hogan, 1988] Hogan, N. (1988). On the stability of manipulators performing contact tasks. *IEEE Transactions on Robotics and Automation*, 4(6):677–686.
- [ISO, 2016] ISO, I. (2016). Ts 15066 (2016): robots and robotic devices—collaborative robots. *Geneva: International Organization for Standardization*.
- [Kong and Gosselin, 2002] Kong, X. and Gosselin, C. M. (2002). Kinematics and singularity analysis of a novel type of 3-crr 3-dof translational parallel manipulator. *The International Journal of Robotics Research*, 21(9):791–798.
- [Krüger et al., 2009] Krüger, J., Lien, T. K., and Verl, A. (2009). Cooperation of human and machines in assembly lines. *CIRP annals*, 58(2):628–646.
- [Kuling et al., 2015] Kuling, I. A., Smeets, J. B., Lammertse, P., Onneweer, B., and Mugge, W. (2015). Delays in admittance-controlled haptic devices make simulated masses feel heavier. *PloS one*, 10(9):e0138023.
- [Labrecque et al., 2016] Labrecque, P. D., Haché, J.-M., Abdallah, M., and Gosselin, C. (2016). Low-impedance physical human-robot interaction using an active–passive dynamics decoupling. *IEEE Robotics and Automation Letters*, 1(2):938–945.
- [Labrecque et al., 2017] Labrecque, P. D., Laliberté, T., Foucault, S., Abdallah, M. E., and Gosselin, C. (2017). Uman: A low-impedance manipulator for human–robot cooperation based on underactuated redundancy. *IEEE/ASME Transactions on Mechatronics*, 22(3):1401–1411.
- [Lamy et al., 2009] Lamy, X., Colledani, F., Geffard, F., Measson, Y., and Morel, G. (2009). Achieving efficient and stable comanipulation through adaptation to changes in human arm impedance. In *2009 IEEE International Conference on Robotics and Automation*, pages 265–271. IEEE.
- [Lauzier et al., 2009] Lauzier, N., Gosselin, C., Laliberté, T., and Tremblay, P. (2009). Adaptive gravity compensation of decoupled parallel and serial manipulators using a passive hydraulic transmission. *Proceedings of the Institution of Mechanical Engineers, Part C: Journal of Mechanical Engineering Science*, 223(12):2871–2879.
- [Lecours et al., 2012] Lecours, A., Mayer-St-Onge, B., and Gosselin, C. (2012). Variable admittance control of a four-degree-of-freedom intelligent assist device. In *2012 IEEE International Conference on Robotics and Automation*, pages 3903–3908. IEEE.
- [Lederman and Klatzky, 1987] Lederman, S. J. and Klatzky, R. L. (1987). Hand movements: A window into haptic object recognition. *Cognitive psychology*, 19(3):342–368.
- [Lee*, 2005] Lee*, H.-H. (2005). Motion planning for three-dimensional overhead cranes with high-speed load hoisting. *International Journal of Control*, 78(12):875–886.

- [Masoud and Nayfeh, 2003] Masoud, Z. N. and Nayfeh, A. H. (2003). Sway reduction on container cranes using delayed feedback controller. *Nonlinear dynamics*, 34(3-4):347–358.
- [Massie et al., 1994] Massie, T. H., Salisbury, J. K., et al. (1994). The phantom haptic interface: A device for probing virtual objects. In *Proceedings of the ASME winter annual meeting, symposium on haptic interfaces for virtual environment and teleoperator systems*, volume 55, pages 295–300. Citeseer.
- [Minsky et al., 1990] Minsky, M., Ming, O.-y., Steele, O., Brooks Jr, F. P., and Behensky, M. (1990). Feeling and seeing: issues in force display. In *ACM SIGGRAPH Computer Graphics*, volume 24, pages 235–241. ACM.
- [Newman and Zhang, 1994] Newman, W. S. and Zhang, Y. (1994). Stable interaction control and coulomb friction compensation using natural admittance control. *Journal of robotic systems*, 11(1):3–11.
- [Okamura et al., 2003] Okamura, A. M., Webster, R. J., Nolin, J. T., Johnson, K., and Jafry, H. (2003). The haptic scissors: Cutting in virtual environments. In *2003 IEEE International Conference on Robotics and Automation (Cat. No. 03CH37422)*, volume 1, pages 828–833. IEEE.
- [Ortega et al., 2006] Ortega, M., Redon, S., and Coquillart, S. (2006). A six degree-of-freedom god-object method for haptic display of rigid bodies. In *IEEE Virtual Reality Conference (VR 2006)*, pages 191–198. IEEE.
- [Piazzi and Visioli, 2002] Piazzi, A. and Visioli, A. (2002). Optimal dynamic-inversion-based control of an overhead crane. *IEE Proceedings-Control Theory and Applications*, 149(5):405–411.
- [Salisbury et al., 2004] Salisbury, K., Conti, F., and Barbagli, F. (2004). Haptic rendering: introductory concepts. *IEEE computer graphics and applications*, 24(2):24–32.
- [Sorensen et al., 2007] Sorensen, K. L., Singhose, W., and Dickerson, S. (2007). A controller enabling precise positioning and sway reduction in bridge and gantry cranes. *Control Engineering Practice*, 15(7):825–837.
- [Starr, 1985] Starr, G. (1985). Swing-free transport of suspended objects with a path-controlled robot manipulator.
- [Sun et al., 2012] Sun, N., Fang, Y., Zhang, X., and Yuan, Y. (2012). Transportation task-oriented trajectory planning for underactuated overhead cranes using geometric analysis. *IET Control Theory & Applications*, 6(10):1410–1423.

- [Tadele et al., 2014] Tadele, T. S., de Vries, T., and Stramigioli, S. (2014). The safety of domestic robotics: A survey of various safety-related publications. *IEEE robotics & automation magazine*, 21(3):134–142.
- [van der Linde and Lammertse, 2003] van der Linde, R. Q. and Lammertse, P. (2003). Hapticmaster—a generic force controlled robot for human interaction. *Industrial Robot: An International Journal*, 30(6):515–524.
- [Van der Linde et al., 2002] Van der Linde, R. Q., Lammertse, P., Frederiksen, E., and Ruiter, B. (2002). The hapticmaster, a new high-performance haptic interface. In *Proc. Eurohaptics*, pages 1–5.
- [Wen et al., 2001] Wen, J. T., Popa, D. O., Montemayor, G., and Liu, P. L. (2001). Human assisted impedance control of overhead cranes. In *Proceedings of the 2001 IEEE International Conference on Control Applications (CCA'01)(Cat. No. 01CH37204)*, pages 383–387. IEEE.
- [Wu and He, 2015] Wu, X. and He, X. (2015). Enhanced damping-based anti-swing control method for underactuated overhead cranes. *IET Control Theory & Applications*, 9(12):1893–1900.
- [Wu and Xia, 2014] Wu, Z. and Xia, X. (2014). Optimal motion planning for overhead cranes. *IET Control Theory & Applications*, 8(17):1833–1842.
- [Zhang et al., 2014] Zhang, X., Fang, Y., and Sun, N. (2014). Minimum-time trajectory planning for underactuated overhead crane systems with state and control constraints.
- [Zilles and Salisbury, 1995] Zilles, C. B. and Salisbury, J. K. (1995). A constraint-based god-object method for haptic display. In *Proceedings 1995 IEEE/RSJ International Conference on Intelligent Robots and Systems. Human Robot Interaction and Cooperative Robots*, volume 3, pages 146–151. IEEE.